Quantum Electromechanics with Two Tone Drive

Thesis by

Aaron Jacob Weinstein

In Partial Fulfillment of the Requirements

for the Degree of

Doctor of Philosophy

California Institute of Technology

Pasadena, California

2016

(Defended October 13, 2015)

To my parents and brother, for their unending support.

Acknowledgements

I would first like to express my sincere gratitude to my advisor Prof. Keith Schwab for the continuous support and guidance over the course of my study. His motivation, innovation, and knowledge made all of this work possible. My sincere thanks also go to the Schwab group postdocs: Dr. Junho Suh, Dr. KC Fong, and Dr. Matt Shaw. Thank you for serving as my daily mentors, for picking up my frantic calls at all hours, and for making these years stuck in windowless rooms a little bit brighter.

Thank you to the numerous staff and postdocs for sharing their valuable time, experience, and perspective. To the Eisenstein group, Prof. Erik Henriksen and Prof. Johannes Pollanen, thanks for all of their optimism, gusto, and low-temperature wizardry. To Mark Gonzalez, thanks for the wonderful training and guidance in the machine shop. To our theory collaborators Prof. Aashish Clerk, Prof. Florian Marquardt, Dr. Anja Metelmann and Dr. Andreas Kronwald, thank you for the clear and concise explanations, most of this analysis would not be possible without your support.

I would also like to thank my fellow labmates Laura DeLorenzo, Chan U Lei, and Dr. Emma Wollman for the stimulating exchanges, morning coffee chats, and shared sleepless days in the lab. Thank you for all the fun that we have had over the past years. To my Caltech friends – Vanessa, Brett, JD, Lincoln, Dvin, Simon, Jasper, Amir, Jeff, Richard, Alex, Tim, – thank you for making these years far more enjoyable than I had ever expected.

Last but not least, I would like to thank my parents and my brother for never losing faith in me and for letting me find my own way in life.

Abstract

In the field of mechanics, it is a long standing goal to measure quantum behavior in ever larger and more massive objects. It may seem like an obvious conclusion now, but up until recently it was not clear whether a macroscopic mechanical resonator – built up from nearly 10^{13} atoms – could be fully described as an ideal quantum harmonic oscillator. With recent advances in the fields of opto- and electro-mechanics, such systems offer a unique advantage in probing the quantum noise properties of macroscopic electrical and mechanical devices, properties that ultimately stem from Heisenberg's uncertainty relations. Given the rapid progress in device capabilities, landmark results of quantum optics are now being extended into the regime of macroscopic mechanics.

The purpose of this dissertation is to describe three experiments – motional sideband asymmetry, back-action evasion (BAE) detection, and mechanical squeezing – that are directly related to the topic of measuring quantum noise with mechanical detection. These measurements all share three pertinent features: they explore quantum noise properties in a macroscopic electromechanical device driven by a minimum of two microwave drive tones, hence the title of this work: "Quantum electromechanics with two tone drive".

In the following, we will first introduce a quantum input-output framework that we use to model the electromechanical interaction and capture subtleties related to interpreting different microwave noise detection techniques. Next, we will discuss the fabrication and measurement details that we use to cool and probe these devices with coherent and incoherent microwave drive signals. Having developed our tools for signal modeling and detection, we explore the three-wave mixing interaction between the microwave and mechanical modes, whereby mechanical motion generates motional sidebands corresponding to up-down fre-

quency conversions of microwave photons. Because of quantum vacuum noise, the rates of these processes are expected to be unequal. We will discuss the measurement and interpretation of this asymmetric motional noise in a electromechanical device cooled near the ground state of motion.

Next, we consider an overlapped two tone pump configuration that produces a time-modulated electromechanical interaction. By careful control of this drive field, we report a quantum non-demolition (QND) measurement of a single motional quadrature. Incorporating a second pair of drive tones, we directly measure the measurement back-action associated with both classical and quantum noise of the microwave cavity. Lastly, we slightly modify our drive scheme to generate quantum squeezing in a macroscopic mechanical resonator. Here, we will focus on data analysis techniques that we use to estimate the quadrature occupations. We incorporate Bayesian spectrum fitting and parameter estimation that serve as powerful tools for incorporating many known sources of measurement and fit error that are unavoidable in such work.

Contents

List of Figures

Chapter 1

Theory

In this chapter, we will first present a classical model for the microwave cavity which we then expand to include dispersive coupling to the motion of a mechanical oscillator. Later, we develop a quantum theory of the electromagnetic and mechanical modes via the input-output framework. We explore how this theory relates to the construction of the output microwave noise spectrum as well as the electromechanical interaction between the microwave and mechanical modes.

1.1 Classical microwave circuit analysis

1.1.1 Ideal circuit

Motivated by the geometry of our device, we model the microwave circuit as a lumped element parallel RLC circuit. Given the resistance R, capacitance C and inductance L, we consider a parallel array accessed via independent ports, which for the purpose of the experiment we separately label the right port "R" as the output and the left port "L" as the input port. Each port constitutes a coupling capacitor connected to a 50Ω transmission lines that serves to couple microwave signal into and out of the device.

Though the parallel RLC circuit is a prototypical example of an electromagnetic resonator and has been extensively analyzed [1], we will derive the circuit voltages and scattering parameters here for a few reasons. First, this analysis helps clarify the connection between the

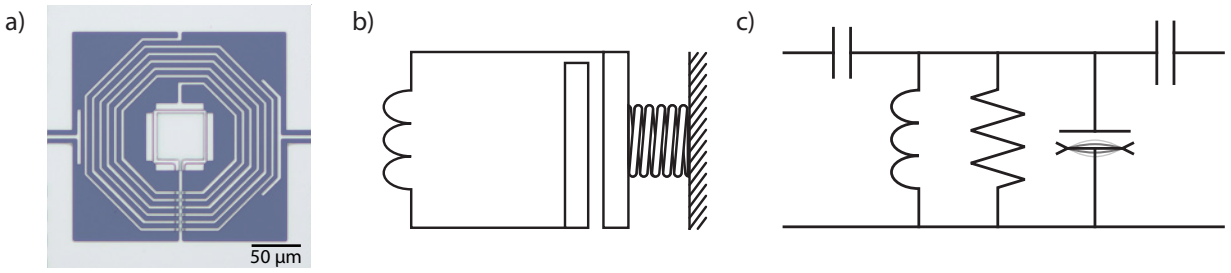

Figure 1.1: Electromechanical device and effective circuit schematics. **a.** Optical micrograph of a typical device from the top view. A parallel plate capacitor (center) is connected to a planar spiral inductor. Input and output coupling capacitors connect the cavity to external microwave waveguides. **b.** Simplified rendition of the microwave circuit emphasizing the electromechanical nature of the device. The microwave resonator is composed of lumped-element inductor and capacitor. The free-standing top gate of the capacitor is a mechanical oscillator, such that changes in position modify the capacitance and hence the microwave resonance frequency. **c.** Equivalent microwave circuit, including the most relevant experimental details: input and output capacitors serve to couple microwave signals into and out of the circuit while internal resistance degrades the quality of the resonator.

classical and quantum circuit models and will serve as useful consistency checks throughout the following calculations. Second, we ideally treat our circuit as an RLC circuit given in Fig. 1.1(a), but in reality our device has numerous features that are not captured in this circuit. We will first analyze the ideal circuit and then extend the model to incorporate technical issues specific to our system (Fig. 1.3(a)). Lastly, this circuit has been analyzed previously within the Schwab group with Norton equivalent circuit analysis [2], which leads to direct calculations for circuit parameters at the cost of potentially obscuring their physical origins. As an alternative method, we will derive the circuit voltages and effective scattering parameters via Kirchoff's circuit law.

To simplify the calculation, we can split the circuit as a T-network with three effective impedances: one for the unloaded resonator, Z_c (i.e., the RLC circuit ignoring the input/output couplers), one for the left port Z_L, denoted in this work as the left port "L", and one for the right port Z_R, denoted as the right port "R". For each grouping, the impedance is calculated directly from the constituent passive components. In this work, we use the engineering convention of $j = \sqrt{-1}$, which differs from the physics convention by a negative sign: $j \rightarrow -i$). Assuming the high-Q limit where we only consider frequencies confined

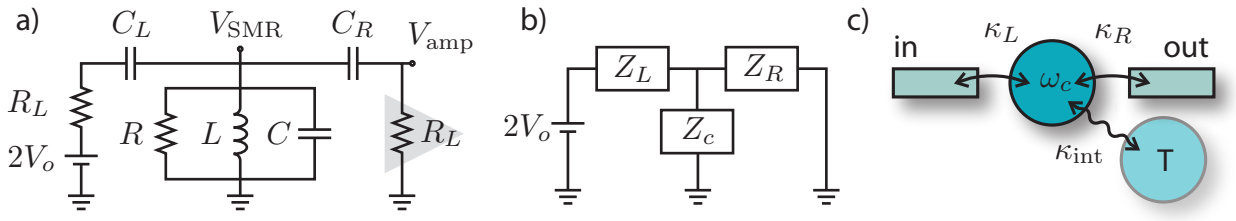

Figure 1.2: Equivalent microwave circuit. **a.** Full microwave circuit schematic including the supply V_o incident on the input capacitor, the load impedances R_L of the input and output transmission lines, the capacitances of the input C_L and output C_R couplers, the effective impedances of the RLC microwave resonator and the voltage drops across the resonator capacitor, $V_{\rm smr}$, and amplifier load $V_{\rm amp}$. **b.** Equivalent impedances. To simplify the calculation and aid intuition, the cavity is split into three effective impedances: Z_L is the input impedance, Z_R is the output impedance, and $Z_{\rm cav}$ is the impedance of the unloaded microwave resonator. **c.** Scattering picture. In the high-Q limit, the microwave resonator and environment is fully represented by a coupled-mode diagram. The microwave cavity (cyan) is characterized by a resonance frequency ω_c and dissipation rate $\kappa = \sum_\sigma \kappa_\sigma$. Each port represents a coupling channel that supports both relaxation and excitation of the cavity mode. The cavity radiates energy into each bath which in turn radiates incoherent noise, given by the equilibrium temperature T_σ, back into the cavity.

within a narrow bandwidth about ω_o (i.e., $\kappa \ll \omega_o$), so that $(\omega^2 - \omega_o^2) \simeq 2\omega_o(\omega - \omega_o)$, we find

$$Z_\sigma(\omega) = R_L + \frac{1}{j\omega C_\sigma}, \tag{1.1}$$

$$Z_{\rm cav}(\omega) = \left(\frac{1}{R} + j\omega C + \frac{1}{j\omega L}\right)^{-1}, \tag{1.2}$$

$$\simeq \frac{\omega_o Z_o}{2} \frac{1}{j(\omega - \omega_o) + \kappa_{\rm int}/2}, \tag{1.3}$$

where we define the characteristic impedance Z_o and bare resonance ω_o as $Z_o = \sqrt{\frac{L}{C}}$ and $\omega_o = \frac{1}{\sqrt{LC}}$. By formulating the impedance in this manner, we can now easily identify the cavity susceptibility as a Lorentzian factor with peak centered about ω_o and internal loss $\kappa_{\rm int}$. The internal loss rate, also defined as the full width at half max (FWHM) of the unloaded resonator, is defined via the circuit parameters as $\kappa_{\rm int} = 1/RC$.

The total impedance of the network, $Z_{\rm tot}$, is defined in terms of the sub-unit circuit

impedances as

$$Z_{\text{tot}} = Z_L + \left(Z_{\text{cav}}^{-1} + Z_R^{-1}\right)^{-1}, \tag{1.4}$$

$$= \frac{Z_{\text{cav}} Z_L Z_R}{Z_{\text{cav}} + Z_R} \left(Z_{\text{cav}}^{-1} + Z_L^{-1} + Z_R^{-1}\right). \tag{1.5}$$

1.1.2 Scattering parameters

We now derive the scattering parameters via the voltage drops over all relevant sections of the circuit. The voltage in the superconducting microwave resonator, V_{smr}, is given by the voltage across the capacitor,

$$V_{\text{smr}} = 2V_o \left(\frac{Z_L^{-1}}{Z_{\text{cav}}^{-1} + Z_L^{-1} + Z_R^{-1}}\right), \tag{1.6}$$

$$= V_o \sqrt{\frac{1}{R_L C}} \frac{j\sqrt{\kappa_L}}{j(\omega - \omega_c) + \kappa/2}, \tag{1.7}$$

where we have omitted the explicit frequency dependence of the effective impedances. The microwave resonance frequency ω_c and total linewidth κ now include the effects of the input and output coupling channels,

$$\omega_c = \omega_o + \sum_{\sigma=R,L} \delta\omega_\sigma, \tag{1.8}$$

$$\kappa = \sum_{\sigma=R,L,\text{int}} \kappa_\sigma. \tag{1.9}$$

Arranging the cavity voltage in a Lorentzian format allows us to identify the scattering parameters associated with each port in relation to the circuit elements. Assuming that the coupling capacitors are sufficiently small ($\omega^2 C_{\text{in}}^2 R_L^2 \ll 1$), the induced frequency shifts scale as

$$\delta\omega_\sigma = -\frac{\omega_o Z_o}{2} \times \text{Im}(Z_\sigma^{-1}), \tag{1.10}$$

$$= \frac{\omega_o}{2} \left(\frac{C_\sigma}{C}\right). \tag{1.11}$$

The loss rate associated with each port follows

$$\kappa_{\text{int}} = \frac{1}{RC}, \tag{1.12}$$

$$\kappa_{\sigma} = \omega_o Z_o \times \text{Re}(Z_{\sigma}^{-1}), \tag{1.13}$$

$$\simeq \omega_o^2 R_L \left(\frac{C_{\sigma}^2}{C}\right). \tag{1.14}$$

Regarding the voltage drop across the amplifier load, the output impedance behaves as a voltage divider,

$$V_{\text{amp}} = \frac{R_L}{Z_R} V_{\text{smr}}, \tag{1.15}$$

$$= j\sqrt{\kappa_R R_L C} V_{\text{smr}}(\omega). \tag{1.16}$$

Since the transmission lines are impedance matched to the signal generator, the power incident on the microwave circuit is given as the average voltage drop across the load resistance $P_{\text{in}} = \langle V_o^2 \rangle / R_L$. The energy stored in the resonator is calculated via the maximum voltage drop across the capacitor and is expressed as the number of coherent photons in the cavity, n_p,

$$U_c = \frac{|V_{\text{smr}}|^2}{2C} \tag{1.17}$$

$$= \frac{\kappa_L}{(\omega - \omega_c)^2 + (\kappa/2)^2} P_{\text{in}}, \tag{1.18}$$

$$= \hbar \omega_c n_p. \tag{1.19}$$

The internally dissipated power is calculated from the time-averaged voltage drop across the internal resistance,

$$P_{\text{int}} = \frac{\langle |V_{\text{smr}}|^2 \rangle}{R} \tag{1.20}$$

$$= \hbar \omega_c n_p \kappa_{\text{int}}. \tag{1.21}$$

Similarly, the output power follows from the time-averaged power dissipated across the amplifier load,

$$P_{\text{out}} = \frac{\langle |V_{\text{amp}}|^2 \rangle}{R_L} \tag{1.22}$$

$$= \frac{\kappa_L \kappa_R}{(\omega - \omega_c)^2 + (\kappa/2)^2} P_{\text{in}}, \tag{1.23}$$

$$= \hbar \omega_c n_p \kappa_R. \tag{1.24}$$

This relationship is useful for calibrating the internal loss, as the the peak height on resonance is given by the ratio $\left(\frac{\kappa_L \kappa_R}{\kappa^2}\right)$.

Based on the format of these equations, we see that the previous definitions of the loss rates κ_σ, initially motivated by identifying the circuit transmission as a Lorentzian lineshape, are properly associated with the dissipation rate of each respective port.

1.1.3 Bypass channel

From Eq. (1.7), the magnitude of the microwave circuit transmission exhibits a Lorentzian lineshape. However, a typical measurement of transmission through the microwave circuit noticeably deviates from a Lorentzian lineshape at frequencies far beyond the resonator linewidth. One distinct feature is the presence of an anti-resonance in the spectrum, indicating interference of multiple current channels at the output of the microwave circuit, in addition to a nearly flat transmission background that far exceeds the noise floor of our measurement apparatus (Fig. 1.3(b)). As a first step to understand this behavior, we assume the presence of a bypass channel that provides an alternate current path between the input and output ports of the sample (Fig. 1.3(a)).

Applying Kirchoff's Circuit Law over the equivalent circuit model, we recover the voltage grop across the resonator, the voltage drop across the amplifier load, and, assuming waveguide impedance matching, the complex transmission $S_{21}(\omega) = V_{\text{amp}}(\omega)/V_o$. For simplicity, we omit writing the explicit frequency dependence for the circuit impedances in the following equations. Under the assumptions that $1/(\omega C_L)$, $1/(\omega C_R)$, $|X_b| \gg R_L$, the voltages simplify

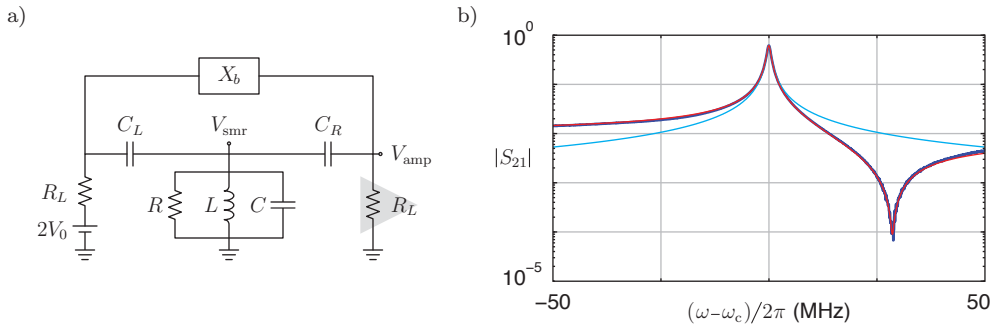

Figure 1.3: Microwave circuit with bypass channel. **a.** Equivalent microwave circuit model of a parallel RLC circuit probed with input and output capacitive couplers C_L, C_R, and including an additional bypass channel characterized by the reactance X_b. **b.** Driven response data (dark blue) fit with a bypass model (red) and ideal model ($|X_b| \to \infty$).

to

$$V_{\rm smr}(\omega) = V_o\sqrt{\frac{1}{R_L C}}\frac{j\sqrt{\kappa_L}}{j(\omega-\omega_c)+\kappa/2}, \tag{1.25}$$

$$V_{\rm amp}(\omega) = j\sqrt{\kappa_R R_L C}V_{\rm smr}(\omega)\left[1-\frac{j2R_L}{X_b}\frac{(\omega-\omega_c)}{\sqrt{\kappa_L\kappa_R}}\right], \tag{1.26}$$

$$S_{21}(\omega) = \frac{-\sqrt{\kappa_L\kappa_R}}{j(\omega-\omega_c)+\kappa/2}. \tag{1.27}$$

We further assume that the bypass channel is approximately flat over the explored frequency range. We can now pull out a frquency-dependent correction factor for the transmission through the resonator,

$$P_{\rm out}(\omega) = \Delta(\omega)\hbar\omega_c n_p \kappa_R, \tag{1.28}$$

where,

$$\Delta(\omega) = \left|1-\frac{j2R_L}{X_b}\frac{(\omega-\omega_c)}{\sqrt{\kappa_L\kappa_R}}\right|^2. \tag{1.29}$$

Though the source of this reactance is not entirely clear, we believe this bypass channel is associated with a sample package or chip mode of the device. Typically, we observe a low quality microwave resonance between 9-12 GHz depending on the dimensions of our fabricated chip. At the frequencies relevant to our measurements, the bypass transmission

through this low-Q mode is sufficiently flat and, due to the large frequency detuning, can be modeled as a positive, imaginary impedance that is consistent with this model.

We have also explored modeling this behavior from other known device features, such as the shunt capacitance of the external couplers or the impedance mismatches between sections of the on-chip waveguides; however, these attributes do not replicate the observed Fano lineshape for cavity transmission.

1.1.4 Optomechanical coupling and sideband transduction

Figure 1.4: Canonical examples of dispersive parametric coupling in opto- and electromechanical systems. **a.** Optomechanical system. One end mirror of a Fabry-Perot cavity is a mechanical resonator such that changes in position will alter the length of the optical cavity which in turns shifts the optical resonance frequency. **b.** Electromechanical system. A mechanical resonator forms one gate of a parallel plate capacitor in a lumped-element microwave resonator. Motion modifies the capacitance gap size which induces a shift in capacitance and resonance frequency. This system is closely replicated for the devices studied in this work.

Motivated by the design of our system, we now consider an electromechanical device that is composed of a LC microwave resonator with a flexible capacitor gate. The motion of the resonator modulates the gap size of the capacitor which in turn shifts the microwave resonance frequency

$$\omega_c = \frac{1}{LC}. \tag{1.30}$$

We express the strength of the electromechanical coupling, g, as

$$g = \frac{\partial \omega_c}{\partial x} = -\frac{\omega_c}{2C}\frac{\partial C}{\partial x}. \tag{1.31}$$

If we consider only a single resonant mode of the gate with resonance frequency ω_m and

amplitude x_o, the microwave resonance frequency now has explicit time modulation,

$$\omega_c(t) = \omega_c \left[1 - \frac{1}{2C}\frac{\partial C}{\partial x} x_o \cos(\omega_m t + \phi_m)\right]. \tag{1.32}$$

To help understand how this system behaves, we can calculate V_{smr} by first assuming that the cavity field instantaneously responds to the motion of the capacitor. The parametric coupling induces a combination of phase and amplitude modulation for the cavity field. For a small frequency shift $\delta\omega_c = \frac{\partial \omega_c}{\partial x} x(t) = g x(t) \ll \omega_c$, we capture the first order corrections by Taylor expanding the cavity transmission prefactor (Eq. (1.7)):

$$V_{\text{smr}} = V_o \left[S_{21}(\omega) + \frac{\partial S_{21}}{\partial \omega}\delta\omega_c(t)\right]_{\omega=\omega_p}, \tag{1.33}$$

$$= V_o S_{21}(\omega_p)\left[1 + \frac{jg}{j(\omega_p - \omega_c) + \kappa/2} x(t)\right], \tag{1.34}$$

$$= V_p e^{i(\omega_p t + \phi_p)} + \sum_{\pm} V_{\pm} e^{i[(\omega_p \pm \omega_m)t + \phi_{\pm}]}. \tag{1.35}$$

Parametrically modulating ω_c at ω_m generates sidebands detuned about the coherent pump at integer multiples of the mechanical resonance frequency with amplitude and phase determined by the pump detuning from cavity resonance.

This calculation hinges on the assumption that the cavity responds to the position of the mechanics much faster than the mechanical period. Since we are in the sideband resolved regime, $\omega_m \gg \kappa$, this assumption is explicitly violated – the cavity field responds to parametric modulation with a time constant on the order of the loaded dissipation rate κ^{-1}.

As a next step, we can extend the circuit model to account for the finite response time of the cavity. The following treatment follows closely along with Sec. 2.4 of [2]. Motivated by Fig. 1.2, the total current for a driven microwave resonator can be expressed as a parametric Mathieu equation,

$$I_o \cos(\omega_p t) = \frac{\partial}{\partial t}(CV) + \frac{1}{R}V + \frac{1}{L}\int dt V, \tag{1.36}$$

where the parametric modulation is implicitly included as the time-dependent capacitance C and the circuit parameters R, L, C include loading effects of the drive and measurement

circuits. Here, the microwave pump signal has been expressed as an incident source current oscillating at drive frequency ω_p and with amplitude I_o which can be expressed in terms of the cavity voltage $V_{\rm smr} = I_o Z_o \omega_p \frac{1}{\sqrt{(\omega_p-\omega_c)^2+(\kappa/2)^2}}$.

As it pertains to our experiments, we consider driving the system near cavity resonance at detunings spanning $\pm\omega_m$. As the cavity is sideband resolved, higher-order sideband terms will be highly suppressed by the cavity response and so we only consider voltage contributions from the first order sidebands. We consider a trial solution that includes the carrier drive and nearest-neighbor sidebands:

$$V(t) = V_p e^{-i(\omega t+\phi_p)} + V_- e^{-i(\omega_- t+\phi_-)} + V_+ e^{-i(\omega_+ t+\phi_+)}. \tag{1.37}$$

Differentiating Eq. (1.36) and substituting in the trial solution, the phase and amplitude for these three components can be solved under the following assumptions: the modulation is sufficiently weak so that the coherent pump is unaffected and follows $V_p e^{i\phi_p} = V_{\rm smr} = V_o\sqrt{\frac{1}{R_L C}}\frac{j\sqrt{\kappa_L}}{j(\omega-\omega_c)+\kappa/2}$, the pump frequency is sufficiently close to cavity resonance so $\omega_p \simeq \omega_c$ simplifies the cavity susceptibilities, and $\omega_m \gg \kappa$ ensures the coupling to higher order sidebands is negligible. In terms of the pump detunings, $\Delta_\pm = \omega_\pm - \omega_c$, the voltage components follow

$$V_- = -gx_o\frac{1}{\sqrt{(\kappa/2)^2+\Delta_-^2}}V_p, \tag{1.38}$$

$$\phi_- = \arctan\left(\frac{\kappa}{2\Delta_-}\right) - \phi_p + \phi_m, \tag{1.39}$$

$$V_+ = -gx_o\frac{1}{\sqrt{(\kappa/2)^2+\Delta_+^2}}V_p, \tag{1.40}$$

$$\phi_+ = \arctan\left(\frac{\kappa}{2\Delta_+}\right) - \phi_p - \phi_m. \tag{1.41}$$

With an entirely classical model, we already see that electromechanical systems exhibit the Raman-like processes of up and down-conversion of photons resulting from the parametric coupling between the mechanical motion and the electromagnetic modes of a resonant cavity. These up and down-converted sidebands form the subject of this work and will be discussed

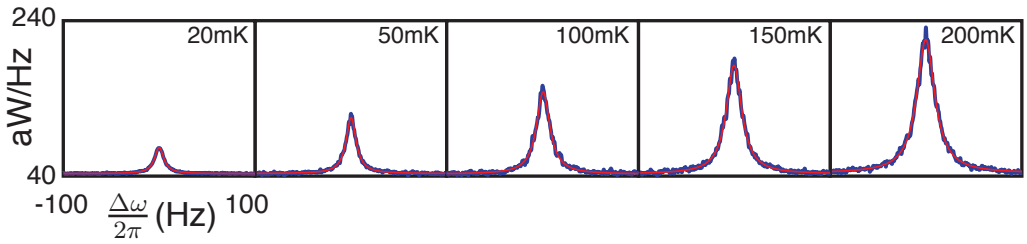

Figure 1.5: Thermomechanical noise spectra. Typical microwave noise spectrum (blue) with Lorentzian fits (red) of the up-converted motional sideband. As the cryostat temperature rises from 20mK to 200mK, we observe the sideband power increase accordingly, as well as a small linear increase in the intrinsic mechanical linewidth.

extensively in the following work. Foreshadowing for later discussion, note that there is a sign difference for the transduced mechanical phase ϕ_m between the up and down converted mechanical sidebands; this serves an important role in quantum noise correlations that arise between the imprecision and back-action noise forces.

From this result, we can derive a useful relation for the integrated microwave noise power under the transduced mechanical sidebands. Following Eqs. (1.38)-(1.41) and assuming that the mechanics is uncorrelated with the drive voltage, the integrated microwave noise power, normalized by the drive power, of the motional sidebands that are up- (+) and down-converted (−) into the cavity center are proportional to the rms motional noise $\langle x^2 \rangle$,

$$\frac{\langle V_\pm^2 \rangle}{\langle V_p^2 \rangle} = \left(\frac{2g}{\kappa} \right)^2 \langle x^2 \rangle. \tag{1.42}$$

Since the normalized ratio $\frac{\langle V_\pm^2 \rangle}{\langle V_p^2 \rangle}$ is insensitive to fluctuations in the output gain of the microwave circuit, this is a useful relationship to extract the electromechanical coupling g . In our experiments, we extract out the prefactor $(\frac{2g}{\kappa})$ by monitoring the ratio between the transduced motional sideband power (Fig. 1.5) and the coherent drive power (measured at the detector output) as we regulate the cryostat temperature from base temperature up to 200mK via calibrated resistance thermometry. As a consistency check, we find that the mechanical bath thermalizes all the way down to the base temperature of our fridge (Fig. 4.2).

1.1.5 Mechanical forces

We have now shown that a dispersive parametric coupling between the mechanical and electromagnetic resonator gives rise to microwave transduction of motion, but that is not the full picture. Through the electromechanical coupling, the electromagnetic resonator energy is now position dependent and gives rise to microwave-induced mechanical forces. As a simple illustration for a microwave resonator with a flexible capacitor gate, the resonator energy is now a function of position, leading to electromagnetic-driven forces on the mechanics,

$$F_{\text{mech}} = -\frac{dU_c}{dx}, \tag{1.43}$$

$$= \frac{1}{2}|V_{\text{smr}}(t)|^2 \left(\frac{dC}{dx}\right). \tag{1.44}$$

From this simple result, we find that the mechanical forces are driven by microwave signal mixing, reminiscent of the three-wave mixing that leads to phonon-photon transduction. Since these mechanical forces are driven by microwave mixing, we must also pay careful attention to microwave noise at $\omega_p \pm \omega_m$ for two reasons. First, the mechanical resonator is in the high-Q limit and only responds to forces that are close to ω_m in the Fourier domain. Second, we typically rely on intense coherent drives at ω_p to enhance the electromechanical coupling, meaning that the dominant force terms at ω_m are generated from mixing between the coherent microwave drive at ω_p and microwave noise in the narrow band about $\omega_p \pm \omega_m$.

This immediately sets up a feedback mechanism that will generally introduce correlations between the microwave and mechanical signals. Furthermore, this feedback system is dynamic in nature: the mechanical signals are transduced into microwave signals which in turn mix back down into mechanical forces.

This feedback mechanism is a source of much of the major results in opto- and electromechanics, such as optomechanical induced transparency [3–5], mechanical cooling [6, 7], mechanical amplification [8], microwave squeezing [9,10]. These results represent major milestones in the fields of mechanical sensing and mechanical state preparation at the quantum level; the purpose of this section is to illustrate an analogous, and perhaps more intuitive,

classical model for much of this behavior.

1.2 Quantum analysis

1.2.1 Transmission line quantization

As a first step to building up a quantum model for electromechanical measurements, we consider the quantization of a microwave transmission line. This is a good place to start since it will guide our treatment of microwave baths and will also shape our treatment for noise spectrum calculations in later sections. This section closely follows the arguments and calculations of [11].

For a transmission line with capacitance per length c and inductance per length l, it is convenient to define the flux variable $\hat{\varphi}$ and momentum conjugate $\hat{q}$ (local charge density). The Hamiltonian is given by

$$\hat{\mathcal{H}} = \int dx \left[\frac{1}{2c}\hat{q}^2 + \frac{1}{2l}(\partial_x \hat{\varphi})^2 \right]. \tag{1.45}$$

The Hamiltonian is simplified with a normal mode expansion for the standing waves on an infinite transmission line. With periodic boundaries, $q = n\pi/L$ for $n \in \mathbb{Z}$,

$$\hat{b}_q \equiv \frac{1}{\sqrt{\hbar\omega_q L}} \int dx e^{-iqx} \left[\frac{1}{\sqrt{2c}}\,\hat{q} - i\sqrt{\frac{q^2}{2l}}\,\hat{\varphi} \right]. \tag{1.46}$$

The Hamiltonian becomes

$$\hat{\mathcal{H}} = \sum_q \hbar\omega_q \hat{b}_q^\dagger \hat{b}_q, \tag{1.47}$$

where $\omega_q = v_p|q|$ is the mode frequency and $v_p = 1/(lc)$ is the wave velocity of the transmission line.

The voltage at one end of an infinite transmission line is defined as the amplitude quadra-

ture of the electromagnetic field.

$$\hat{V}(x,t) = \sum_q \sqrt{\frac{\hbar\omega_q}{2Lc}} \left[\hat{b}_q e^{i(qx-\omega_q t)} + \hat{b}_q^\dagger e^{i(qx+\omega_q t)}\right], \tag{1.48}$$

where the explicit time-dependence of the bath operators are given by the Heisenberg equation of motion. Ignoring any coupling between bath and system, $\hat{b}_q(t) = \hat{b}_q e^{-i\omega_q t}$.

Based on the form of Eq. (1.48), we can organize the voltage operator into right moving fields, proportional to $(t - \frac{x}{v_p})$, or left moving fields proportional to $(t + \frac{x}{v_p})$:

$$\hat{V}(x,t) = \hat{V}^{\rightarrow}(t - \frac{x}{v_p}) + \hat{V}^{\leftarrow}(t + \frac{x}{v_p}). \tag{1.49}$$

Expanding Eq. (1.49) and noting that $\omega_q \geq 0$ for all q,

$$V^{\rightarrow}(t) = \int_0^\infty \frac{d\omega}{2\pi} \sqrt{\frac{\hbar\omega Z_o}{2}} \left[\hat{b}^{\rightarrow}[\omega] e^{-i\omega t} + \hat{b}^{\dagger\rightarrow}[\omega] e^{i\omega t}\right], \tag{1.50}$$

where the right-moving annihilation operator is defined as

$$\hat{b}^{\rightarrow}[\omega] \equiv 2\pi \sqrt{\frac{v_p}{L}} \sum_{q>0} \hat{b}_q \delta(\omega - \omega_q). \tag{1.51}$$

Similarly, the left-moving field is

$$V^{\leftarrow}(t) = \int_0^\infty \frac{d\omega}{2\pi} \sqrt{\frac{\hbar\omega Z_o}{2}} \left[\hat{b}^{\leftarrow}[\omega] e^{-i\omega t} + \hat{b}^{\dagger\leftarrow}[\omega] e^{i\omega t}\right], \tag{1.52}$$

$$\hat{b}^{\rightarrow}[\omega] \equiv 2\pi \sqrt{\frac{v_p}{L}} \sum_{q<0} \hat{b}_q \, \delta(\omega - \omega_q). \tag{1.53}$$

Note that the right and left movers are separated in the Fourier domain into positive and negative frequencies. This frequency separation ensures that the field commutators are nonzero only for identically moving fields,

$$\left[\hat{b}^{\rightarrow}[\omega], \hat{b}^{\dagger\rightarrow}[\omega']\right] = \left[\hat{b}^{\leftarrow}[\omega], \hat{b}^{\dagger\leftarrow}[\omega']\right] = 2\pi \, \delta(\omega - \omega'), \tag{1.54}$$

and also introduces Heaviside step functions into the correlators for the right-moving field,

$$\langle \hat{b}^{\dagger\rightarrow}[\omega]\hat{b}^{\rightarrow}[\omega']\rangle = 2\pi\,\delta(\omega-\omega')n_\sigma\Theta(\omega), \tag{1.55}$$

$$\langle \hat{b}^{\rightarrow}[\omega]\hat{b}^{\dagger\rightarrow}[\omega']\rangle = 2\pi\,\delta(\omega-\omega')(n_\sigma+1)\Theta(\omega), \tag{1.56}$$

and correlators for the left-moving field,

$$\langle \hat{b}^{\dagger\leftarrow}[\omega]\hat{b}^{\leftarrow}[\omega']\rangle = 2\pi\,\delta(\omega-\omega')n_\sigma\Theta(-\omega), \tag{1.57}$$

$$\langle \hat{b}^{\leftarrow}[\omega]\hat{b}^{\dagger\leftarrow}[\omega']\rangle = 2\pi\,\delta(\omega-\omega')(n_\sigma+1)\Theta(-\omega), \tag{1.58}$$

where the fields are taken to be in equilibrium with a bath at occupation n_σ.

This transmission line quantization applies to standing electromagnetic waves on an isolated transmission line. This is a rather simplified example of what we typically encounter in experiments. For a finite length transmission line loaded on either side by measurement equipment, the boundary conditions at each termination introduce explicit relationships between the right- and left-moving waves. These conditions potentially alter the manner in which we treat the microwave fields. For example, a semi-infinite transmission line terminated at $x = 0$ by an impedance-matched spectrum analyzer will absorb all incident signals. For the left-moving signals, the microwave field propagates in the other direction and, at least in theory, never reflects back to the analyzer. In this situation, the analyzer is only sensitive to the right moving signal $\hat{V}^{\rightarrow}$. In Sec. 1.3, we explore how this behavior manifests for the types of noise measurements considered in this work.

1.2.2 Input-output relations

We will now consider the dynamics between a quantum system coupled to a bosonic bath continuum and will arrive at Langevin-Heisenberg equations for the system operator that includes the effects of bath-induced dissipation and noise fluctuations. The arguments and calculations presented here closely follow along with [11, 12].

The Hamiltonian for a system coupled to a bath is

$$\hat{\mathcal{H}} = \hat{\mathcal{H}}_{\text{sys}} + \hat{\mathcal{H}}_{\text{bath}} + \hat{\mathcal{H}}_{\text{int}}. \tag{1.59}$$

The bath is a continuum of independent harmonic oscillators labeled by the quantum number q,

$$\hat{\mathcal{H}}_{\text{bath}} = \sum_q \hbar\omega_q \hat{b}_q^\dagger \hat{b}_q, \tag{1.60}$$

with commutation relations,

$$\left[\hat{b}_q, \hat{b}_{q'}^\dagger\right] = \delta_{q,q'}. \tag{1.61}$$

We make the rotating wave approximation and only consider the resonant contributions to the system-bath interaction Hamiltonian,

$$\hat{\mathcal{H}}_{\text{int}} = -i\hbar \sum_q \left[f_q \hat{a}^\dagger \hat{b}_q - f_q^* \hat{a}^\dagger \hat{b}_q\right], \tag{1.62}$$

where f_q represents the coupling strength between system and bath operators. Terms like $\hat{b}^\dagger \hat{a}^\dagger$ and $\hat{b}\hat{a}$ have been neglected since they are unphysical and are fast oscillating in the interaction picture.

Next, we take the Markov approximation and assume the coupling is frequency independent,

$$\sum_q |f_q|^2 e^{-i(\omega_q - \omega_c)(t-t')} = \kappa\delta(t-t'). \tag{1.63}$$

Substituting between the Heisenberg equations for the system and bath operators, we arrive at the Langevin-Heisenberg equations for the cavity mode that includes both dissipation and coupling to bath fluctuations,

$$\dot{\hat{a}} = \frac{i}{\hbar}\left[\hat{\mathcal{H}}_{\text{sys}}, \hat{a}\right] - \frac{\kappa}{2}\hat{a} - \sqrt{\kappa}\hat{b}_{\text{in}}(t), \tag{1.64}$$

where the input and output field operators are defined in terms of the bath modes,

$$\hat{b}_{\text{in}}(t) \equiv \tfrac{1}{\sqrt{\kappa}} \sum_q f_q e^{i\omega_q(t-t_0)} \hat{b}_q(t_0), \tag{1.65}$$

$$\hat{b}_{\text{out}}(t) \equiv \tfrac{1}{\sqrt{\kappa}} \sum_q f_q e^{i\omega_q(t-t_1)} \hat{b}_q(t_1). \tag{1.66}$$

Solving for the system operator dynamics, we arrive at the Langevin-Heisenberg equation for the system operator,

$$\dot{\hat{a}} = \frac{i}{\hbar}\left[\hat{\mathcal{H}}_{\text{sys}}, \hat{a}\right] - \frac{\kappa}{2}\hat{a} - \sqrt{\kappa}\hat{b}_{\text{out}}, \tag{1.67}$$

with the input-output boundary condition,

$$\hat{b}_{\text{out}}(t) = \hat{b}_{\text{in}}(t) + \sqrt{\kappa}\hat{a}(t). \tag{1.68}$$

This final condition implies that the output microwave field consists of the system signal coupling out of the external port in addition to the reflected input bath noise. This relationship captures the behavior of a system coupled to the environment through a single port. In our work, we deal with cavities that are coupled to the environment through multiple ports that arise from both external and internal dissipation. We can generalize the input-output relations for multiple ports σ, each associated with separate scattering rates κ_σ, and input bath operators $\hat{b}_{\sigma,\text{in}}$. The only modification to the relations above is that we must now specify an input-output boundary condition for each port,

$$\hat{b}_{\sigma,\text{out}}(t) = \hat{b}_{\sigma,\text{in}}(t) + \sqrt{\kappa_\sigma}\hat{a}(t). \tag{1.69}$$

Since the input-output conditions are linear, the system responds identically to the Heisenberg-Langevin equation Eq. (1.68), except now the bath operator and scattering rate is given by

the weighted average of the port contributions,

$$\kappa = \sum_{\sigma} \kappa_{\sigma} \tag{1.70}$$

$$\hat{b}_{\text{in}} = \sum_{\sigma} \sqrt{\frac{\kappa_{\sigma}}{\kappa}} \hat{b}_{\sigma\text{in}}. \tag{1.71}$$

As a final note, the input-output relations are a useful tool to model the linear propagation of noise through our system. As it pertains to calculating experiment measurables like the noise spectral density radiating out of the cavity or the complex transmission through the microwave circuit, we only consider the "right-moving" fields of Eq. (1.48) which restricts the summation in Eqs. (1.71) to only positive quantum numbers, $q > 0$. This restriction implies that the input bath annihilation operator only has spectral weight at positive frequencies.

This frequency separation introduces Heaviside step functions that depend on the time-ordering of the bath operators. For example, Fourier terms like

$$\int dt e^{i\omega t} \langle \hat{d}^{\dagger}_{\sigma,\text{in}}(0) \hat{d}_{\sigma,\text{in}}(t) \rangle = n_{\sigma} \Theta(\omega) \tag{1.72}$$

have spectral weight only at positive frequencies. Alternatively, terms like

$$\int dt e^{i\omega t} \langle \hat{d}^{\dagger}_{\sigma,\text{in}}(t) \hat{d}_{\sigma,\text{in}}(0) \rangle = n_{\sigma} \Theta(-\omega) \tag{1.73}$$

only have spectral weight at negative frequencies. Since the output microwave field $\hat{b}_{\text{out}}$ will be linearly proportional to the input field $\hat{b}_{\text{in}}$, we omit output-field correlation terms that, following the input field correlators, have no spectral weight at positive frequencies.

1.3 Noise detection

In this work, we apply continuous wave signals and measure in the frequency domain. Therefore, the bulk of the analysis is performed in the frequency domains and utilizes two main techniques, microwave noise measurement and scanning homodyne detection. Here we con-

sider the microwave noise spectrum, also referred to as the power spectral density of the output voltage noise.

Consider output voltage noise normalized to units of quanta,

$$\hat{V}_{\text{out}} = \hat{d}_{\text{out}} + \hat{d}^{\dagger}_{\text{out}}. \tag{1.74}$$

The power spectral density of the outgoing voltage noise is given by

$$S_{VV}[\omega] = \langle |\hat{V}_{\text{out}}[\omega]|^2 \rangle. \tag{1.75}$$

Assuming the voltage fluctuations are stationary and ergodic [11, 13], the Wiener-Kintchin theorem connects the spectral density to the Fourier transform of the autocorrelator $G_{VV}(t) = \langle \hat{V}_{\text{out}}(t)\hat{V}_{\text{out}}(0) \rangle$,

$$S_{VV}[\omega] = \int dt e^{i\omega t} \langle \hat{V}_{\text{out}}(t)\hat{V}_{\text{out}}(0) \rangle, \tag{1.76}$$

$$= \int dt e^{i\omega t} \langle \hat{d}^{\dagger}_{\text{out}}(t)\hat{d}_{\text{out}}(0) + \hat{d}_{\text{out}}(t)\hat{d}^{\dagger}_{\text{out}}(0) \rangle. \tag{1.77}$$

1.3.1 Linear detection

A general approach to measure the power spectrum of the microwave field is to first measure the time-dependent quadrature amplitudes of the output field and then use these elements to calculate a power spectrum. We do this in our experiment by using a linear amplifier to measure the voltage associated with the outgoing field.

This detection scheme is formally equivalent to a diode plus filter. The diode serves a large bandwidth square-law power detector that is sensitive to the integrated voltage noise over the full frequency domain. To isolate only a sharp peak of the noise spectrum, we introduce a well-behave, normalized bandpass filter function $f[\omega]$ sharply peaked at the designated ω. The voltage at the filter output is

$$\hat{V}_f[\omega] = f[\omega]\hat{V}_{\text{out}}[\omega]. \tag{1.78}$$

With filter in place, the diode output is

$$I \propto |\hat{V}_f|^2 = \int_{-\infty}^{\infty} d\omega |f[\omega]|^2 S_{VV}(\omega), \tag{1.79}$$

$$= \frac{1}{2}\left(S_{VV}[\omega] + S_{VV}[-\omega]\right), \tag{1.80}$$

$$= \bar{S}_{VV}[\omega]. \tag{1.81}$$

The second line follows from the fact that the filter function is real in the time domain, $f[\omega] = f[-\omega]^*$ so that $|f[\omega]|^2 = |f[-\omega]|^2$. Moving to notation for the noise spectrum emanating from the right port "R" port of the our device, we find that linear detection is sensitive to the symmetrized output noise spectrum,

$$\bar{S}_R[\omega] = \frac{1}{2}\int dt e^{i\omega t}\langle\{\hat{V}_{\text{out}}(t), \hat{V}_{\text{out}}(0)\}\rangle, \tag{1.82}$$

$$= \frac{1}{2}\int dt e^{i\omega t}\langle \hat{d}^\dagger_{R,\text{out}}(0)\hat{d}_{R,\text{out}}(t) + \hat{d}_{R,\text{out}}(t)\hat{d}^\dagger_{R,\text{out}}(0)\rangle. \tag{1.83}$$

This last line arises from the frequency separation of the transmission line modes to right- and left-moving fields so that the output voltage is defined only for the single branch of positive frequencies and terms with no spectral weight at the specified frequency are omitted.

Note that symmetric detection is sensitive to the shot noise of the electromagnetic field since it contains terms like $\langle \hat{d}_{\text{out}}\hat{d}^\dagger_{\text{out}}\rangle$. Associating the field correlator $\langle \hat{d}^\dagger_{\text{out}}\hat{d}_{\text{out}}\rangle$ with photon destruction and $\langle \hat{d}_{\text{out}}\hat{d}^\dagger_{\text{out}}\rangle$ with photon emission, the symmetric spectrum can be reinterpreted as the average rate at which the detector absorbs and radiates energy with the environment.

For the case of voltage digitization and fourier transformation, an ADC will sample a time series of voltages across an impedance-matched load. Once the voltage stream is stored as classical real data, the classical voltage commutes with itself at all times, giving rise to a symmetrized noise spectrum. Alternatively, the voltage time series is complex conjugate symmetric in the Fourier domain ($V[\omega] = V[-\omega]^*$), and so again the spectral density from digitization must be symmetric in frequency.

1.3.2 Nonlinear detection

What if one performs direct photon counting instead of linear noise detection? Since photodetection is sensitive only to the absorption of photons, the corresponding noise spectrum contains only to normal-ordered terms consistent with the Glauber formalism [11, 14]. In terms of the microwave noise radiating out of the output port "R", the photon-counting spectrum is

$$S_R[\omega] = \int dt e^{i\omega t} \langle : \hat{V}_{\text{out}}(t)\hat{V}_{\text{out}}(0) : \rangle, \tag{1.84}$$

$$= \int dt e^{i\omega t} \langle \hat{d}^\dagger_{R,\text{out}}(0)\hat{d}_{R,\text{out}}(t) \rangle. \tag{1.85}$$

Since the normal-ordered detection only absorbs energy from the system, this measurement scheme is not sensitive to the vacuum fluctuations of the electromagnetic field.

Note that the symmetrized and normal-ordered spectra are related through the commutation relations of the output microwave field ($[\hat{d}_{\sigma,\text{out}}, \hat{d}^\dagger_{\sigma,\text{out}}] = 1$) and are thus necessarily the same minus a white shot noise floor,

$$\bar{S}_R[\omega] = S_R[\omega] + \tfrac{1}{2}. \tag{1.86}$$

Since there is little question whether a microwave field behaves quantum mechanically, it seems straightforward to relate the rates of emission to that of absorption. By formally applying the output field commutation relation, measurements can be framed as measuring only photon absorption or both photon emission and absorption. Is this an important distinction? If the question is whether or not the outgoing light field behaves quantum mechanically, then perhaps not. But, as we show later, if the question extends to broader statements about proving the quantum mechanical essence of macroscopic mechanical objects, then yes this is an important distinction and raises ambiguity in measurement interpretation.

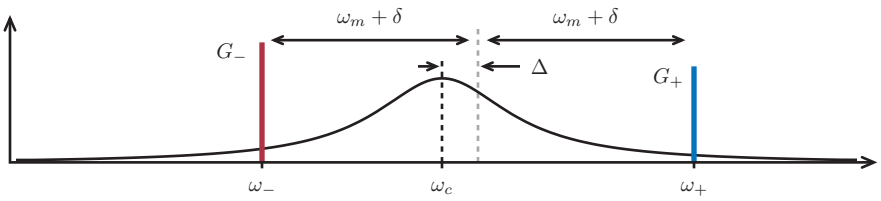

Figure 1.6: General two-tone pump configuration. The drive field consists of two microwave tones (red and blue peaks) detuned above and below the cavity resonance ω_c (cavity DOS in black) at frequencies ω_+ and ω_- and with amplitudes $\alpha_\pm$ leading to enhanced optomechanical coupling strengths $G_\pm$. To simplify calculations, we move into the interaction pictures with the cavity field rotating about $\omega_c + \Delta$ and mechanical field rotating about $\omega_m + \delta$. The detunings are defined via the microwave drive frequencies: $\Delta = [\frac{1}{2}(\omega_+ + \omega_-) - \omega_c]$ and $\delta = [\frac{1}{2}(\omega_+ - \omega_-) - \omega_m]$.

1.4 Optomechanical interaction

We are now ready to tackle modeling our electromechanical system within the input-output framework defined above.

1.4.1 Linearized optomechanical Hamiltonian and quantum Langevin equations

We consider the canonical optomechanical Hamiltonian,

$$\hat{H} = \hbar\omega_c \hat{a}^\dagger \hat{a} + \hbar\omega_m \hat{b}^\dagger \hat{b} - \hbar g_0 \hat{a}^\dagger \hat{a} \left(\hat{b} + \hat{b}^\dagger\right) + \hat{\mathcal{H}}_{\text{diss}} + \hat{\mathcal{H}}_{\text{drive}}, \tag{1.87}$$

where $\hat{a}$ $\left(\hat{a}^\dagger\right)$ is the annihilation (creation) operator of the intra-cavity microwave field, $\hat{b}$ $\left(\hat{b}^\dagger\right)$ is the mechanical phonon annihilation (creation) operator, and $g_0 = \frac{\partial \omega_c}{\partial x} x_{\text{zp}}$ is the bare optomechanical coupling. The term $\hat{\mathcal{H}}_{\text{diss}}$ models the cavity and mechanical dissipation channels to their respective baths, consistent with input-output relations of Eq. (1.67), and the final term $\hat{\mathcal{H}}_{\text{drive}}$ captures the coherent cavity driving.

We will now begin to tailor this calculation to our experimental system. In our experiment, the otpomechanical system is a two-port electromechanical system driven from the left input port, which we designate (L), and measured via the right output port, which we designate (R). We initially consider driving the system with two microwave tones detuned

above and below the cavity resonance. The drive Hamiltonian reads

$$\hat{H}_{\text{drive}} = \hbar \sum_{\nu=\pm} \alpha_\nu \left(\hat{a} e^{i\omega_\nu t} + \hat{a}^\dagger e^{-i\omega_\nu t} \right), \tag{1.88}$$

where $\omega_\pm = \omega_c + \Delta \pm (\omega_m + \delta)$ and $\alpha_\pm$ are the red and blue pump amplitudes defined at the input port. The detunings δ and Δ are shown in Fig.1.6. In the following, we apply standard linearization, i.e., we separate the cavity and the mechanical operators, $\hat{a}$ and $\hat{b}$, into a classical part, $\bar{a}$ or $\bar{b}$, plus quantum fluctuations, $\hat{d}$ or $\hat{c}$. E.g., $\hat{a} \to \bar{a} + \hat{d}$. In the interaction picture with respect to $\hat{H}_0 = \hbar (\omega_c + \Delta) \hat{a}^\dagger \hat{a} + \hbar (\omega_m + \delta) \hat{b}^\dagger \hat{b}$, we find the *linearized* optomechanical Hamiltonian

$$\hat{H}_{\text{lin}} = \hat{H}_{\text{RWA}} + \hat{H}_{\text{CR}} \,. \tag{1.89}$$

Here,

$$\hat{H}_{\text{RWA}} = -\hbar \Delta \hat{d}^\dagger \hat{d} - \hbar \delta \hat{c}^\dagger \hat{c} - \hbar \left[\left(G_+ \hat{c}^\dagger + G_- \hat{c} \right) \hat{d}^\dagger + \left(G_+ \hat{c} + G_- \hat{c}^\dagger \right) \hat{d} \right] \tag{1.90}$$

describes the resonant part of the linearized optomechanical interaction, whereas

$$\hat{H}_{\text{CR}} = -\hbar \left[G_+ e^{-2i(\omega_m+\delta)t} \hat{c} + G_- e^{2i(\omega_m+\delta)t} \hat{c}^\dagger \right] \hat{d}^\dagger - \hbar \left[G_+ e^{2i(\omega_m+\delta)t} \hat{c}^\dagger + G_- e^{-2i(\omega_m+\delta)t} \hat{c} \right] \hat{d} \tag{1.91}$$

describes off-resonant optomechanical interactions. Note that $G_\pm = g_0 \bar{a}_\pm$ describes the driven-enhanced optomechanical coupling. Here, $\bar{a}_\pm$ is the intracavity microwave amplitude due to the red and blue pumps, and we have assumed $\bar{a}_\pm \in \mathbb{R}$ for simplicity and without loss of generality.

Let us first consider the good cavity limit ($\omega_m \gg \kappa$) which allows us to work within the rotating wave approximation, $\hat{H}_{\text{lin}} \approx \hat{H}_{\text{RWA}}$. In this case, the linearized quantum Langevin equations (Eq.(1.67)) read

$$\dot{\hat{d}} = -\left(\frac{\kappa}{2} - i\Delta \right) \hat{d} + i \left(G_- \hat{c} + G_+ \hat{c}^\dagger \right) + \sqrt{\kappa} \hat{d}_{\text{in}}, \tag{1.92}$$

$$\dot{\hat{c}} = -\left(\frac{\gamma_m}{2} - i\delta \right) \hat{c} + i \left(G_- \hat{d} + G_+ \hat{d}^\dagger \right) + \sqrt{\gamma_m} \hat{c}_{\text{in}} \,. \tag{1.93}$$

Here, $\hat{d}_{\rm in} = \sum_{\sigma=L,R,I} \sqrt{\frac{\kappa_\sigma}{\kappa}} \hat{d}_{\sigma,\rm in}$ is the total input noise of the cavity, where $\hat{d}_{\sigma,\rm in}$ describes the input fluctuations to the cavity from channel σ with damping rate κ_σ. $\sigma = L$ and R correspond to the left and right microwave cavity ports, while $\sigma = I$ corresponds to internal losses. The noise operator $\hat{c}_{\rm in}$ describes quantum and thermal noise of the mechanical oscillator with intrinsic damping rate γ_m. The input field operators satisfy the following commutation relations:

$$\left[\hat{d}_{\sigma,\rm in}(t), \hat{d}^\dagger_{\sigma',\rm in}(t')\right] = \delta_{\sigma,\sigma'}\delta(t-t'), \tag{1.94}$$

$$\left[\hat{c}_{\rm in}(t), \hat{c}^\dagger_{\rm in}(t')\right] = \delta(t-t'), \tag{1.95}$$

$$\langle \hat{d}^\dagger_{\sigma',\rm in}(t)\hat{d}_{\sigma,\rm in}(t')\rangle = n^{\rm th}_\sigma \delta_{\sigma,\sigma'}\delta(t-t'), \tag{1.96}$$

$$\langle \hat{c}^\dagger_{\rm in}(t)\hat{c}_{\rm in}(t')\rangle = n^{th}_m \delta(t-t'), \tag{1.97}$$

where $n^{\rm th}_\sigma$ is the photon occupation in port σ, and $n^{th}_m = \left[\exp\left(\hbar\omega_m/k_BT\right)-1\right]^{-1}$ is the thermal occupation of the mechanical oscillator. The total occupation of the cavity is the weighted sum of the contributions from different channels: $n^{th}_c = \sum_\sigma \frac{\kappa_\sigma}{\kappa} n^{\rm th}_\sigma$.

We include multiple bath temperatures (n^{th}_σ) to describe the various sources of heating in microwave circuits. Compared to optical cavities which are passively cooled well into the ground state ($< 10^4$ K), microwave cavities can have significant thermal occupation even at temperatures reached in the dilution refrigerator. Filtering on the input and output transmission lines suprresses incident room tepmrerature noise; however, other issues may remain, like internal dissipation in the cavity [15], or thermal noise from refrigerator components [16]. Additionally, there are other issues common to both microwave and optical systems, such as source-phase noise [9] and cavity-frequency jitter [17]. Whatever the source, noise in the system can be generalized into two categories based on how the noise contributes to the measured signal, either by radiating directly into the cavity (n^{th}_l and n^{th}_i) or by radiating into both the cavity and detector (n^{th}_r).

For microwave noise spectrum calculations, we will also encounter correlations between the cavity operator and the output port bath. The input-output relations and cavity field

correlations yield

$$\langle \hat{d}^{\dagger}_{R,\mathrm{in}}(t)\, \hat{d}_{\mathrm{in}}(t')\rangle = \langle \hat{d}^{\dagger}_{\mathrm{in}}(t)\, \hat{d}_{R,\mathrm{in}}(t')\rangle = \sqrt{\frac{\kappa_R}{\kappa}}\, n_r^{th}\, \delta(t-t') \tag{1.98}$$

$$\langle \hat{d}_{R,\mathrm{in}}(t)\, \hat{d}^{\dagger}_{\mathrm{in}}(t')\rangle = \langle \hat{d}_{\mathrm{in}}(t)\, \hat{d}^{\dagger}_{R,\mathrm{in}}(t')\rangle = \sqrt{\frac{\kappa_R}{\kappa}}\, (n_r^{th}+1)\, \delta(t-t') \tag{1.99}$$

$$\langle \hat{d}^{\dagger}_{R,\mathrm{in}}(t)\hat{d}^{\dagger}_{\mathrm{in}}(t')\rangle = \langle \hat{d}_{R,\mathrm{in}}(t)\hat{d}_{\mathrm{in}}(t')\rangle = 0. \tag{1.100}$$

1.4.2 Optomechanical output spectrum and mechanical spectrum

In this section, we derive the optomechanical output spectrum and the mechanical quadrature spectrum, first within the RWA and later in Sec. 1.3 including bad cavity effects. For this, we solve the quantum Langevin equations (Eqs. 1.92, 1.93) in Fourier space. It is convenient to define the vectors $\boldsymbol{D} = \left(\hat{d}, \hat{d}^{\dagger}, \hat{c}, \hat{c}^{\dagger}\right)^T$, $\boldsymbol{D}_{\mathrm{in}} = \left(\hat{d}_{\mathrm{in}}, \hat{d}^{\dagger}_{\mathrm{in}}, \hat{c}_{\mathrm{in}}, \hat{c}^{\dagger}_{\mathrm{in}}\right)^T$ and $\boldsymbol{L} = \mathrm{diag}\left(\sqrt{\kappa}, \sqrt{\kappa}, \sqrt{\gamma_m}, \sqrt{\gamma_m}\right)$. We then find the following solution to the quantum Langevin equations in frequency space:

$$\hat{\boldsymbol{D}}\left[\omega\right] = \boldsymbol{\chi}\left[\omega\right] \cdot \boldsymbol{L} \cdot \hat{\boldsymbol{D}}_{\mathrm{in}}\left[\omega\right], \tag{1.101}$$

where

$$\boldsymbol{\chi}\left[\omega\right] \equiv \begin{pmatrix} \frac{\kappa}{2} - i\left(\omega+\Delta\right) & 0 & -iG_- & -iG_+ \\ 0 & \frac{\kappa}{2} - i\left(\omega-\Delta\right) & iG_+ & iG_- \\ -iG_- & -iG_+ & \frac{\gamma_m}{2} - i\left(\omega+\delta\right) & 0 \\ iG_+ & iG_- & 0 & \frac{\gamma_m}{2} - i\left(\omega-\delta\right) \end{pmatrix}^{-1}. \tag{1.102}$$

We measure the output microwave spectrum through the undriven (right) cavity port. One finds the input-output relation $\hat{d}_{\sigma,\mathrm{out}}[\omega] = \hat{d}_{\sigma,\mathrm{in}}[\omega] + \sqrt{\kappa_\sigma}\hat{d}[\omega]$,

$$\hat{d} = \boldsymbol{\chi}_{11}\sqrt{\kappa}\hat{d}_{\mathrm{in}} + \boldsymbol{\chi}_{12}\sqrt{\kappa}\hat{d}^{\dagger}_{\mathrm{in}} + \boldsymbol{\chi}_{13}\sqrt{\gamma_m}\hat{b}_{\mathrm{in}} + \boldsymbol{\chi}_{14}\sqrt{\gamma_m}\hat{b}^{\dagger}_{\mathrm{in}}, \tag{1.103}$$

where all explicit frequency dependence has been omitted. The complex transmission spectrum (driven response) is given by

$$S_{21}[\omega] = -\sqrt{\kappa_L \kappa_R}\, \boldsymbol{\chi}_{11}(\omega). \tag{1.104}$$

The symmetric noise spectral density (Eq. (1.83)) is given by

$$\bar{S}_R[\omega] = \int dt e^{i\omega t} \langle \hat{d}^\dagger_{R,\mathrm{out}}(0)\hat{d}_{R,\mathrm{out}}(t) + \hat{d}_{R,\mathrm{out}}(t)\hat{d}^\dagger_{R,\mathrm{out}}(0)\rangle, \tag{1.105}$$

$$= \kappa_R \kappa \left(|\boldsymbol{\chi}_{11}|^2 + |\boldsymbol{\chi}_{12}|^2\right)\, (n_c^{th} + 1/2) \tag{1.106}$$

$$+ \kappa_R \gamma_m \left(|\boldsymbol{\chi}_{13}|^2 + |\boldsymbol{\chi}_{14}|^2\right)\, (n_m^{th} + 1/2) \tag{1.107}$$

$$+ \left[1 - \kappa_R \left(\boldsymbol{\chi}_{11} + \boldsymbol{\chi}^*_{11}\right)\right]\, (n_r^{th} + 1/2). \tag{1.108}$$

It is also useful to consider the normal-ordered spectrum, $\bar{S}_R[\omega] = S_R[\omega] + \frac{1}{2}$:

$$\begin{aligned} S_R[\omega] &= \int dt e^{i\omega t} \langle \hat{d}^\dagger_{R,\mathrm{out}}(0)\hat{d}_{R,\mathrm{out}}(t)\rangle \\ &= \kappa_R \kappa |\boldsymbol{\chi}_{11}|^2\, n_c^{th} \\ &\quad + \kappa_R \kappa |\boldsymbol{\chi}_{12}|^2\, (n_c^{th} + 1) \\ &\quad + \kappa_R \gamma_m |\boldsymbol{\chi}_{13}|^2\, n_m^{th} \\ &\quad + \kappa_R \gamma_m |\boldsymbol{\chi}_{14}|^2\, (n_m^{th} + 1) \\ &\quad + \left[1 - \kappa_R \left(\boldsymbol{\chi}_{11} + \boldsymbol{\chi}^*_{11}\right)\right]\, n_r^{th}. \end{aligned}$$

1.4.3 Motional noise spectrum

The mechanical spectrum is obtained in a similar fashion. The mechanical annihilation operator is defined via the scattering terms,

$$\hat{b} = \boldsymbol{\chi}_{31}\sqrt{\kappa}\hat{d}_{\mathrm{in}} + \boldsymbol{\chi}_{32}\sqrt{\kappa}\hat{d}^\dagger_{\mathrm{in}} + \boldsymbol{\chi}_{33}\sqrt{\gamma_m}\hat{b}_{\mathrm{in}} + \boldsymbol{\chi}_{34}\sqrt{\gamma_m}\hat{b}^\dagger_{\mathrm{in}}. \tag{1.109}$$

The position noise spectrum is calculated in the lab frame as

$$S_{xx}[\omega] = \int dt e^{i\omega t}\langle \hat{x}(t)\hat{x}(0)\rangle, \tag{1.110}$$

$$= x_{\rm zp}^2 \left\{ |\boldsymbol{\chi}_{31}(\omega)|^2 + |\boldsymbol{\chi}_{32}(-\omega)|^2 \right\} \kappa(n_c^{th}+1) \tag{1.111}$$

$$+ x_{\rm zp}^2 \left\{ |\boldsymbol{\chi}_{32}(\omega)|^2 + |\boldsymbol{\chi}_{31}(-\omega)|^2 \right\} \kappa n_c^{th} \tag{1.112}$$

$$+ x_{\rm zp}^2 \left\{ |\boldsymbol{\chi}_{33}(\omega)|^2 + |\boldsymbol{\chi}_{34}(-\omega)|^2 \right\} \gamma_m(n_m^{th}+1) \tag{1.113}$$

$$+ x_{\rm zp}^2 \left\{ |\boldsymbol{\chi}_{34}(\omega)|^2 + |\boldsymbol{\chi}_{33}(-\omega)|^2 \right\} \gamma_m n_m^{th}. \tag{1.114}$$

The symmetrized motional noise spectrum is defined in terms of symmetrized bath contributions,

$$\bar{S}_{xx}[\omega] = \frac{1}{2}\int dt e^{i\omega t}\langle \{\hat{x}(t),\hat{x}(0)\}\rangle, \tag{1.115}$$

$$= x_{\rm zp}^2 \left(|\chi_{31}(\omega)|^2 + |\chi_{32}(\omega)|^2 \right) \kappa(n_c^{th}+\alpha/2) \tag{1.116}$$

$$+ x_{\rm zp}^2 \left(|\chi_{33}(\omega)|^2 + |\chi_{34}(\omega)|^2 \right) \gamma_m(n_m^{th}+\beta/2), \tag{1.117}$$

$$= \frac{x_{\rm zp}^2\gamma_{\rm tot}}{(|\omega|-\omega_m)^2+(\frac{\gamma_{\rm tot}}{2})^2} \left[\frac{\gamma_m}{\gamma_{\rm tot}} \left(n_m^{th}+\frac{\beta}{2} \right) + \frac{\gamma_{\rm op}^+ + \gamma_{\rm op}^-}{\gamma_{\rm tot}} \left(n_c^{th}+\frac{\alpha}{2} \right) \right], \tag{1.118}$$

$$= \frac{x_{\rm zp}^2\gamma_{\rm tot}}{(|\omega|-\omega_m)^2+(\frac{\gamma_{\rm tot}}{2})^2} \left(n_m + \frac{\tilde{\beta}}{2} \right). \tag{1.119}$$

If necessary, bad cavity effects can be incorporated using the same truncation techniques as outlined in the section below.

1.4.4 Calculation of bad cavity effects

In the frequency domain, the explicit time-dependence of $\hat{\mathcal{H}}_{\rm CR}$ couples sytem operators at different frequencies to each other,

$$\hat{\boldsymbol{D}}_{\boldsymbol{CR}}[\omega] = \boldsymbol{\chi}_{\boldsymbol{CR}}[\omega] \cdot \boldsymbol{L}_{\boldsymbol{CR}} \cdot \hat{\boldsymbol{D}}_{\boldsymbol{CR},\rm in}[\omega]. \tag{1.120}$$

Here, $\hat{\boldsymbol{D}}_{\boldsymbol{CR}}[\omega]$ contains infinitely many sidebands detuned by $\Omega = 2\,(\omega_m + \delta)$,

$$\hat{\boldsymbol{D}}_{\boldsymbol{CR}}[\omega] = \Big(... \; \hat{\boldsymbol{D}}[\omega - 2\Omega],\, \hat{\boldsymbol{D}}[\omega - \Omega],\, \hat{\boldsymbol{D}}[\omega],\, \hat{\boldsymbol{D}}[\omega + \Omega],\, \hat{\boldsymbol{D}}[\omega + 2\Omega] \; ...\Big)\,,$$

while $\hat{\boldsymbol{D}}\,[\omega]$ is defined in the same manner as in Sec. 1.4.2.

The updated scattering matrix $\boldsymbol{\chi}_{\boldsymbol{CR}}$ iteratively builds up the bad-cavity couplings,

$$\boldsymbol{\chi}_{\boldsymbol{CR}}(\omega) = \begin{bmatrix} \ddots & & & & & \\ \boldsymbol{\chi}_- & \boldsymbol{\chi}^{-1}(\omega - \Omega) & \boldsymbol{\chi}_+ & 0 & 0 & \\ 0 & \boldsymbol{\chi}_- & \boldsymbol{\chi}^{-1}(\omega) & \boldsymbol{\chi}_+ & 0 & \\ 0 & 0 & \boldsymbol{\chi}_- & \boldsymbol{\chi}^{-1}(\omega + \Omega) & \boldsymbol{\chi}_+ & \\ & & & & \ddots & \end{bmatrix}^{-1}, \tag{1.121}$$

with

$$\boldsymbol{\chi}_- = \begin{bmatrix} 0 & 0 & -iG_+ & 0 \\ 0 & 0 & iG_- & 0 \\ 0 & 0 & 0 & 0 \\ iG_- & iG_+ & 0 & 0 \end{bmatrix}, \tag{1.122}$$

and

$$\boldsymbol{\chi}_+ = \begin{bmatrix} 0 & 0 & -iG_- & 0 \\ 0 & 0 & iG_+ & 0 \\ -iG_+ & -iG_- & 0 & 0 \\ 0 & 0 & 0 & 0 \end{bmatrix}. \tag{1.123}$$

In order to solve the equations of motion, we truncate the number of sidebands that we take into account, i.e., we truncate the length of $\hat{\boldsymbol{D}}_{\boldsymbol{CR}}$ to the n^{th} sideband at frequency $(\omega_m \pm n\Omega)$. As the analytic solutions are unwieldy even for first order corrections, we instead numerically calculate the spectrum at frequencies specified by the data. In this fashion, the likelihood function can still be evaluated and, with proper choice of numerical methods, maximum likelihood estimation techniques can still be utilized for data fitting and parameter estimation.

Chapter 2

Fabrication and measurement

This chapter will discuss the measurement details that are common to the experiments discussed in this work. We first describe the design and fabrication of our electromechanical device, then describe relevant details following how we package, probe and analyze the system.

2.1 Device design

Previous electromechanical work in the Schwab group at Cornell and Maryland utilized metalized nitride nanowires coupled to superconducting half-wave resonators. Using these kinds of devices, mechanical cooling [18] and back-action evasion measurements [19] closely approached the quantum regime but were hindered by technical nonidealities induced by relatively weak electromechanical coupling and sufficiently large second order capacitance nonlinearities. Motivated by electromechanical devices fabricated at JILA [4,20], the work in the Schwab group at Caltech focused on a similar device design that incorporates a vacuum-gap planar capacitor and lumped element spiral inductor. Compared to the nanowires, the drastic increase in capacitance and mechanical stiffness of the planar capacitor mitigated the previous difficulties with cooling and BAE measurements. Furthermore, we hoped to develop alternative processing techniques that would ideally suppress known microwave issues such as two-level system noise. Our design of these devices is discussed below.

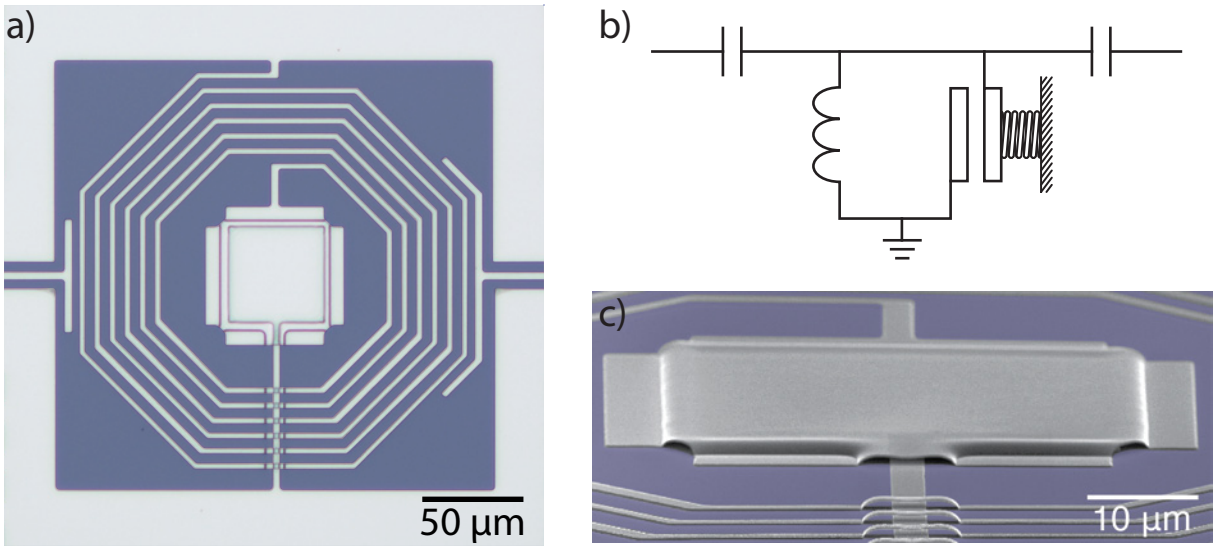

Figure 2.1: Device images. **a.** Top view optical micrograph of the device. The microwave circuit is fabricated from aluminum (grey) on a silicon substrate (blue). A parallel plate capacitor, center, is surrounded by a spiral planar inductor to form a microwave resonator. Input and output coupling capacitors transmit signals into and out of the device. **b.** Simplified circuit model. The top gate of the capacitor is a compliant membrane that supports drumhead acoustic modes. **c.** Electron micrograph side view of the capacitor. The gap between the capacitor gates is roughly 100nm at cryogenic temperatures.

2.1.1 Device modeling

We simulate the microwave resonators in *Sonnet*, a commercial 2.5D electromagnetic field solver that incorporates the Method of Moments applied to Maxwell's equations. Shooting for a microwave resonance between 5 and 7 GHz, we model a $40\mu\text{m}\times40\mu\text{m}$ capacitor placed at the center of 6-turn spiral inductor. The capacitor is placed in the center of the inductor for technical reasons; we have no way of producing clean interconnects between different metalization layers so the capacitor serves as the interconnect between the bottom spiral and top airbridge layers of the inductor. From simulation, we extract out the dissipation rates associated with intrinsic dissipation and radiation loss channels. For high-resistivity silicon with a loss tangent of 2×10^{-4} [21], we expect a loss rate on the order of $2\pi\times100$ kHz stemming from eddy currents induced in the substrate. Radiation loss is a much weaker effect, only contributing around $2\pi\times5$ kHz of loss.

Ignoring other dissipation sources such as those associated with fabrication imperfections,

like dirt in the capacitor gap or trapped between the inductor metalization and subtrate, the total internal loss is expected to be about $\kappa_{\text{int}} = 2\pi \times 165\text{kHz}$. To mitigate the effects of dielectric loss, we have attempted to switch from the device substrate from silicon to sapphire but have encountered difficulties with modifying the fabrication recipes as the subtrate alters the behavior of the sacrificial layer.

We can also extract the equivalent circuit parameters for the inductance and parasitic capacitance. We extract a total inductance of approximately 15 nH, consistent with analytic calculations for planar spiral inductors [22]. For the parasitic capacitance, the series capacitance of the air bridges and the capacitive coupling of the inductor to ground account for roughly $C_p = 30$ fF. Given that we can achieve capacitor gaps of approximately 100 nm, the parasitics roughly account for 20% of the total capacitance and hence the participation ratio of the position-dependent capacitance is on the order of one: $\eta = \frac{C}{C+C_p} \simeq 0.8$.

As an aside, we have fabricated suspended top gates in both squares and circle patterns. Though we do expect to see improved mechanical behavior of circular boundaries [23], in practice we observe worse performance probably due to fabrication issues associated with the altered design.

2.1.2 Suppressed parametric effects

We can perform a simple calculation to compare the onset of parametric amplification between nanowire [19] and planar capacitor devices. In both devices, the capacitance depends on the position as $\frac{1}{x}$ and hence contains terms to all orders in a Taylor expansion. Only considering the second order term, $\frac{\partial^2 C}{\partial x^2}$, the mechanics responds to the electromechanical coupling with a power dependent spring shift, $\Delta\omega_m = \frac{1}{2}\frac{k_{\text{EM}}}{k}$, where k is the bare mechanical spring constant and the induced electromagnetic spring constant is

$$k_{\text{EM}} = \frac{\hbar\omega_c n_p}{2C}\frac{\partial^2 C}{\partial x^2}. \tag{2.1}$$

With two tone drive detuned by $\pm\omega_m$, the spring shift modulates the mechanical resonance at twice the mechanical frequency. Such modulation supports mechanical parametric

amplification [12] such that the amplification factor scales with the ratio of the frequency shift compared to the linewidth, $\frac{\Delta\omega_m}{\gamma_m}$. Calculating this factor for a set optical scattering rate (ignoring differences in x_{zp} scales), we find that it scales inversely with spring constant and participation ratio:

$$\frac{\Delta\omega_m}{\gamma_m} = \frac{Q_m}{2}\frac{k_{\mathrm{EM}}}{k}, \tag{2.2}$$

$$= \frac{\hbar\gamma_{\mathrm{op}}}{2}\left(\frac{Q_m}{Q_c}\right)\left(\frac{1}{k}\right)\left(\frac{1}{\eta}\right). \tag{2.3}$$

Assuming the consistent resonator Q's between nanowire and planar devices, we find that the amplification factor at a given cooperativity is highly suppressed in the planar devices by nearly six orders of magnitude, mainly due to the enhanced participation ratio.

2.2 Fabrication

In this section, we will first describe the fabrication recipe for processing the current generation of electromechanical devices. Though this recipe may appear circuitous, it is the result of multiple years of work spread between four graduate students and postdocs and is informed by many iterations of alternative failed recipes. To elucidate these steps and hopefully save other graduate students untold hours in the cleanroom, the remainder of the section will discuss process development details of three older recipes that incorporated alternative choices for deposition techniques, film materials and sacrificial layers. The different recipes are denoted by their most relevant fabrication details: "NbTin and SiO_2", "Germanium and thermal", "PMGI and e-beam" and "Polymer and sputter".

2.2.1 Device recipe

We start with high-resistivity silicon wafer ($> 10\mathrm{k}\Omega/\mathrm{cm}^2$) prepared with a modified RCA clean and BOE oxide strip. A 100 nm thick aluminum layer is sputter deposited at 6 Å/s in a 5 mTorr Argon environment via a UHV-compatible DC magnetron sputter gun mounted

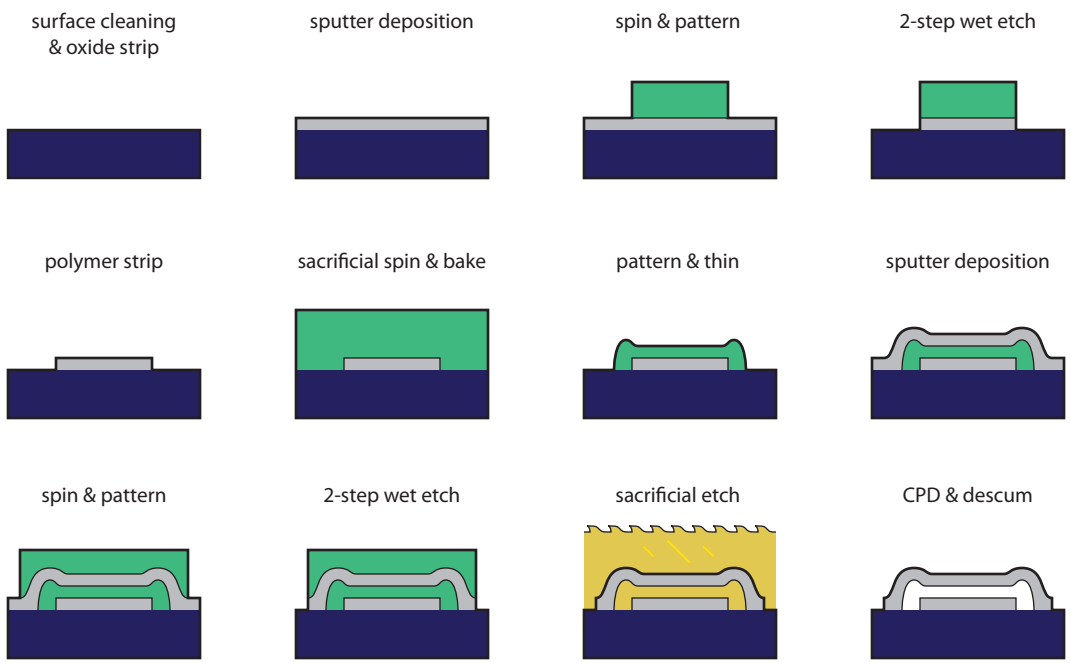

Figure 2.2: Fabrciation steps. The device is processed on a high-resistivity silicon wafer (blue). 100nm aluminum (grey) is sputter deposited and patterned via a wet etch. Photoresist (green) serves as both an etch-stop for the device and a sacrificial layer, defining the capacitor's gap size and protecting the bottom layer from later processing steps. The sacrificial layer is removed in a solvent soak in Remover PG (yellow) and device is dried via critical point drying to ensure the top gate does not collapse.

in a UHV chamber with a base pressure of $< 10^{-}9$ Torr. The bottom layer design is patterned with contact photolithography using an S1800 series photoresist. A two-step subtractive wet etch, consisting of Transene Aluminum etchant followed by CD-26, removes the exposed bottom layer. Following polymer removal via Remover PG, the sacrificial layer is patterned and thinned via double-exposure contact photolithography. After reflow and surface preparation of the sacrificial layer with O_2 plasma descum, the top layer is sputter deposited and patterned under the same conditions as the bottom aluminum layer. The sacrificial layer is removed via overnight soaking in PG Remover. To avoid collapse of the top gate, the device is dried in a critical point drier followed by a final O_2 plasma clean.

Next, we will discuss previous iterations of the recipes for older generations of devices.

2.2.2 NbTiN and SiO_2

In the Schwab group, the electromechanics work at Caltech began with the work of a postdoc, Matt Shaw, who fabricated a suspended, planar capacitor device entirely out of NbTiN. The aim for using such a material was to achieve exceedingly high microwave Q (Q $\sim 10^6$ seen in $\lambda/4$ resonators made of NbTiN [24]) and potentially overcome nonlinearities associated with two-level system defects that are typically encountered in aluminum-based microwave cavities [25]. Coincidentally, the group had access to a cleanroom at the Jet Propulsion Laboratory (JPL) with a high-quality NbTiN sputter chamber up and running.

The device was fabricated on high-resistivity silicon substrate and the NbTiN was reactive ion sputtered in argon environment [15]. The top gate of the capacitor was suspended via a silica sacrificial layer removed in a buffered-oxide etch (BOE) release soak. This recipe proved difficult to control as the BOE soak altered the film stress of the NbTiN. Despite attempts to diagnose and fix the issue, this device exhibited low microwave Q and significant Ohmic heating at the pump powers required for sufficient optomechanical coupling.

Interestingly, this device showed a thermal-induced parametric instability in BAE pump configuration (see Fig. 4.1). With pumps detuned by twice the mechanical resonance frequency, the power in the cavity modulates at twice the mechanical frequency. The mechanical mode had a small enough specific heat and fast enough thermal time constant for the phonon bath to track along with the modulating cavity power. Due to a thermal-induced mechanical resonance frequency, this pump configuration modulated ω_m at twice its frequency, eventually reaching a parametric instability at elevated pump powers [15].

We attempted to diagnose the different possible causes for the low microwave Q and associated heating issues by repeating fab processing steps on quarter wave resonators, but we failed to find a smoking gun. After months, we moved on to fabricating new devices out of aluminum and relying only on Caltech facilities.

2.2.3 Germanium and Thermal Evaporation

At the time, our group had a custom built thermal evaporator mounted in a UHV chamber that had only been exposed to aluminum. For the next device, we chose to work with thermal-evaporated aluminum because of the group's past experience and because the campus cleanroom had few options for producing clean superconducting films from Nb or NbTiN.

Since the group was also familiar with metallized nitride films for mechanical resonators [18, 19], the first device iteration was designed around a vacuum gap capacitor with a thick ($\sim \mu$m) top gate and mechanical mode in the bottom gate formed by a nitride membrane coated with 100nm of aluminum. We used LPCVD nitride deposited on high-resistivity silicon (> 10 kΩ/cm^2). For the sacrificial layer, we chose to work with e-beam evaporated germanium so that we could take advantage of a dry XeF_2 etch that aggressively attacks Si/Ge with undercut etch rates in excess of 40μm/min [26]. This etch step fit nicely into the processing steps: the nitride coating protected the silicon substrate, XeF_2 does not attack aluminum, and the aluminum is not exposed to any flourine-containing plasmas.

Using this technique, we achieved reasonable gaps and optomechanical coupling. However, the device had significant frequency jitter that worsened with aging and thermal cycling. The device also showed significant TLS nonlinearities [17]. Thout we were unable to diagnose the problem, we believe that these defects were likely associated with the choice of sacrificial layer (germanium alloys with aluminum and absorbs water) and the sacrificial etch (XeF_2 slowly attacks nitride).

2.2.4 PMGI and E-Beam Evaporation

In an effort to develop as gentle a sacrificial layer removal etch as possible, we next began working on devices based around polymer sacrificial layers. We kept the same device design as before – a doubly clamped beam at the center of a spiral inductor – and also kept the mechanics as a metalized membrane on the bottom plane.

To achieve sacrificial layers on the order of 200-500nm, we used an underlayer resist, PMGI. We also moved from thermal-evaporated aluminum to e-beam evaporation in hopes

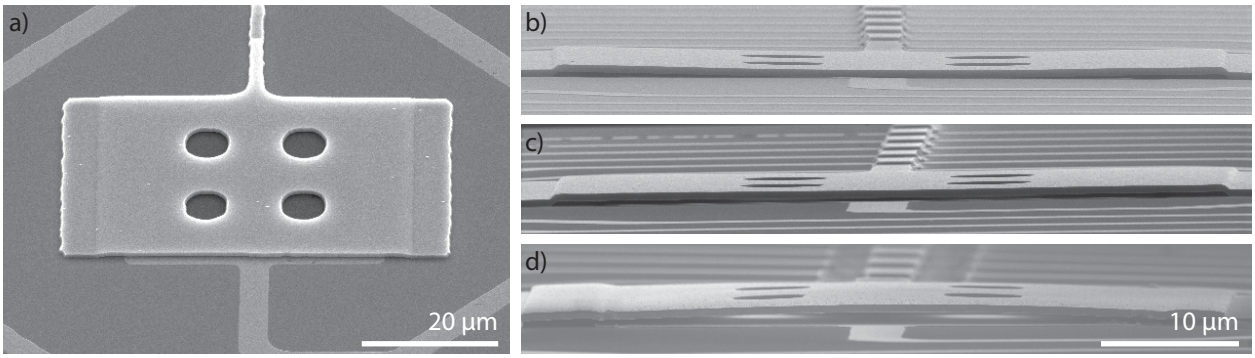

Figure 2.3: Aluminum stress control. **a.** E-beam deposited aluminum with PMGI sacrificial layer. The top gate stress was difficult to control. With nearly identical processing conditions, the top gate would **b.** collapse, **c.** appear nearly flat or **d.** pop up from compressive stress.

of getting better deposition control. The aluminum was patterned with a wet etch and the sacrificial layer was removed with an overnight soak in Remover-PG. The new devices showed consistent optomechanical coupling rates but with improved TLS behavior. Despite much effort to get better control of the capacitor gap size, the stress in the top gate was inconsistent between depositions – sometimes tensile stress, sometimes compressive stress – and hence it was very difficult to control the behavior of the top gate after release (Fig. 2.3).

We attempted to shape the top gate to control the deformation with compressive stress, but the stress varies enough between runs that there is no way to do this repeatedly despite attempts at thermal annealing [27]. As another last ditch effort, we split the e-beam deposition of the top layer into seven steps and mounted the device to a thermal heat-sink. Alas, there was no obvious improvement and we were unable to control the film stress.

2.2.5 Polymer and Sputtered Aluminum

After the last iteration of devices, we needed a method to control stress of the aluminum film. To accomplish this, we removed our thermal evaporator and replaced it with a UHV compatible magnetron sputter system. The move to a sputter deposition system allows for control of the aluminum film stress via control of the backing argon pressure.

Ideally, replacing the e-beam deposition with sputter deposition would work with minimal recipe modification; unsurprisingly, this was not the case. The sputtered films differed from

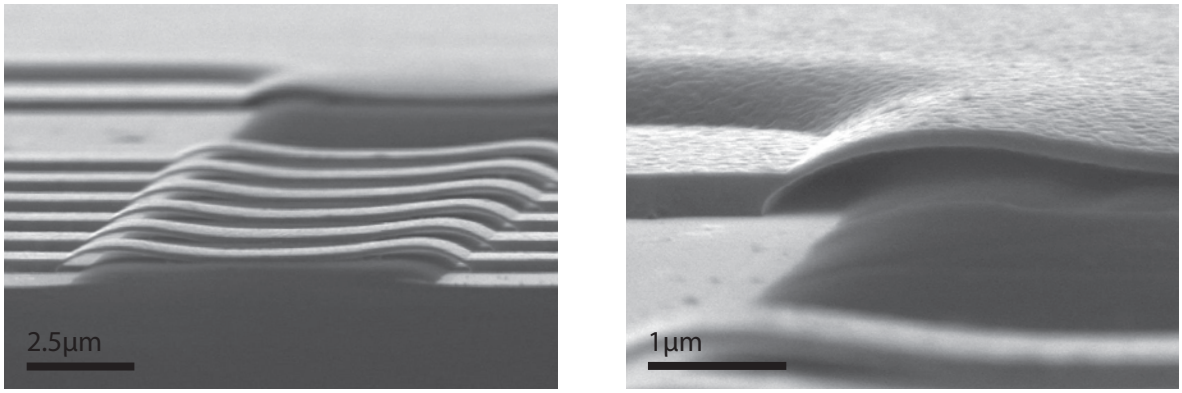

Figure 2.4: PMGI adhesion issues. **a.** The PMGI sacrificial layer (black) exhibits poor adhesion to the sputtered aluminum (light grey) and poor resistivity to the wet aluminum etchant. As evidenced by the thinning of the inductor air bridges, the device could not survive full aluminum patterning . **b.** Poor adhesion between the PMGI and aluminum causes the etchant to rapidly penetrate the edges of the top layer.

e-beam deposition in multiplecurcial ways. First, sputter deposition is nearly isotropic, so that there is no option of lift-off – all patterning must be done with a subtractive etch process.

Another important issue is that our sputtered films do not etch cleanly with transene etchant. After sufficient etch time, the substrate surface is left with a spackled residue. XDS analysis of the residue confirmed that it was aluminum oxide, which is not surprising since we have no in-situ surface prep and are unable to control our subtrate surface chemistry. Since we were unable to strip reside with designated aluminum etchant, we attempted a low dosage of TMAH common to photoresist developers (CD-26), which worked to remove the residue. Thus, we use a two-step wet etch: Transene aluminum etchant A followed by CD-26. The final dip in CD-26 cleans off surface residue over a short enough time that the remaining film is insignificantly attacked.

However, the recipe still did not work as is. Sputtered films that are annealed above 130° display hillock formation [28,29]. PMGI requires baking at temperatures in excess of 170° and so this problem is somewhat unavoidable. Hillocks on the scale of 50nm significantly perturb the behavior of the gap; however, the polymer can conformally coat such topolographical defects and this recipe could still work.

Finally, the adhesion between the PMGI and sputtered aluminum is so poor that we are unable to wet etch the top aluminum layer without destroying the air bridges of the spiral inductor. After attempts to reactive-ion etch (RIE) and descum to activate and roughen up the PMGI surface, there is still no improvement. Attempts to move to dry etch the top layer were futile as the etch would chlorinate the top polymer layer, rendering it difficult to remove. As an aside, we also considered a lift-off technique for sputtered films but, due to the isotropic nature of the deposition, the sidewall quality tapers off over microns, which is unsuitable for bridges or inductors.

Serendipitously, we explored aluminum adhesion with different polymers and a fellow graduate student, Chan U Lei, explored new recipes based around the Shipley S-series photoresists. Initial tests exhibited good adhesion between sputtered aluminum and S1800. To optimize the adhesion, we found that thinning the photoresist with a weak flood-exposure followed by surface activation with a short oxygen plasma descum created sufficient adhesion to survive the remaining fabrication steps. Since S1800 spins down to around 1.5μm, we moved to a thinner resist in the same series, S500, in hopes of directly spin-coating a 500 nm sacrificial layer with higher precision than the double-exposure techniques required for S1800, however the thinner resist had similar adhesion issues despite similar surface preparation steps.

Based on our experimentation so far, the only recipe compatible with sputtered aluminum and polymer sacrificial layers is based around S1800 series spun to around 1.5μm and thinned to around 500nm via flood exposure. To control the thickness of this layer, we must calibrate with spin speed and exposure time. However, the contact photolithography equipment we use only controls exposure time steps within 0.10s steps. Given the lamp power drifts and aging, this is not a very accurate method to control the polymer thickness. Since the polymer behavior also differs with age and humidity, the trick was to calibrate and then fab as many devices as possible.

Though we did not have a chance to attempt different sacrificial layer types, combining a dielectric sacrificial layer with a wet etch removal might be possible with alternative silicon etches [30, 31] that do not attack aluminum.

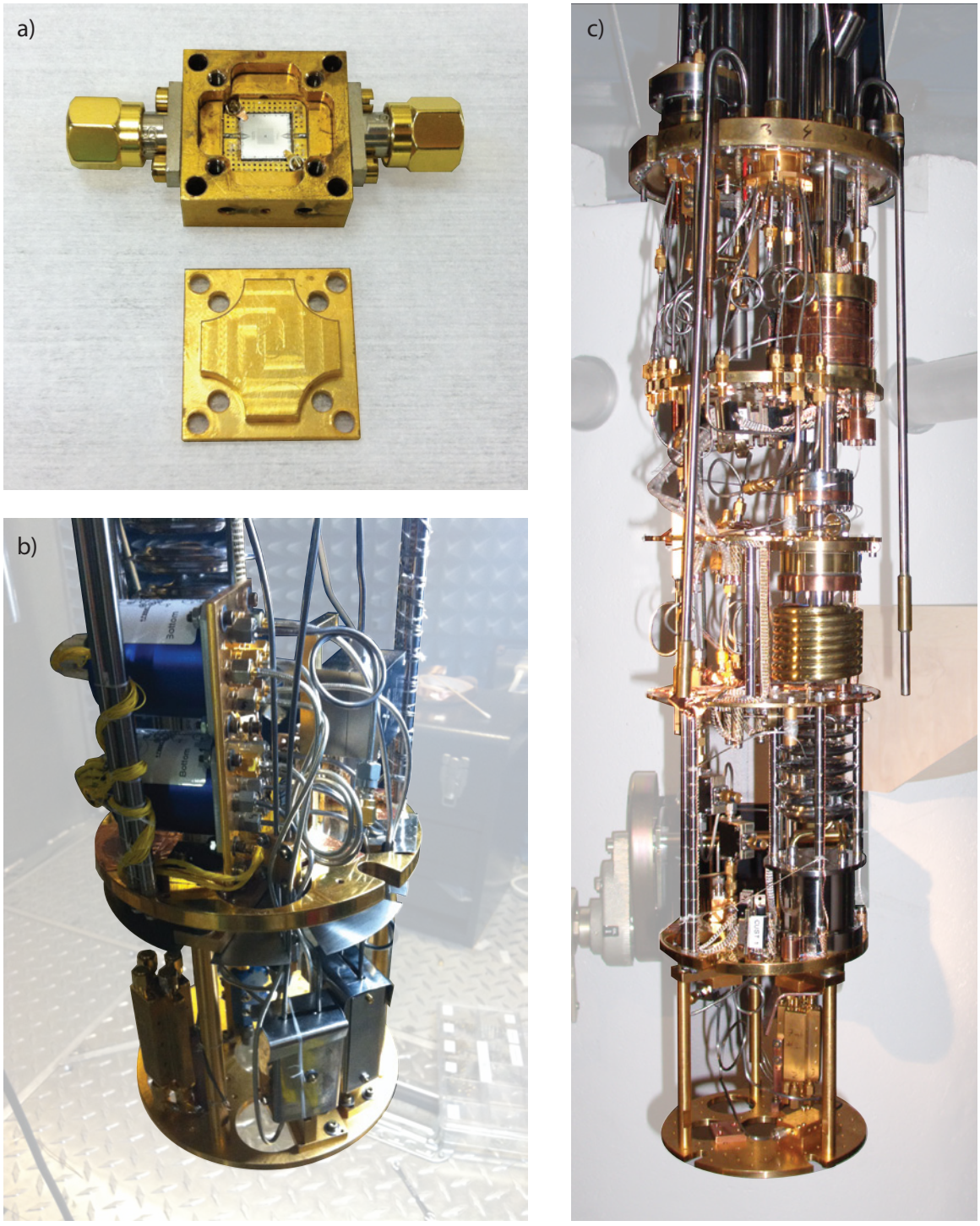

Figure 2.5: Device mounting. **a.** The device is mounted and wirebonded into a copper sample package. **b.** Each sample package is mounted to the mixing plate and shielded with superconducting and mu-metal shields. The microwave switches (blue cans) are visible. **c.** Our dilution refrigerator is an Oxford Kelvinox400.

2.3 Measurement techniques

2.3.1 Device packaging

We process our devices on 6mmx6mm and 6mmx3mm silicon chips. We found that moving to 3mm chips pushed out chip modes, doubled our fab output, and was directly compatible with existing 6x6mm packaging equipment. These chips are clip-mounted into copper sample packages though we have also explored PMMA gluing. The chip waveguides are wirebonded out to grounded CPW tranmission lines onto an arlon PCB that is impedance matched to the silicon wafer. The arlon circuit boards are indium soldered into the copper sample packages and the PCB transmission lines are soft soldered to coax ferrule adapters that launch the microwave signals through the sample package. These coax adapters mate to field replaceable SMA connectors which are commercially available from Southwest Microwave in both standard and non-magnetic options. We have tested both kinds of connectors and have observed no obvious differences in device behavior.

The sample package is mounted to a cold finger on the mixing plate of an Oxford Kelvinox 400 wet dilution refrigerator. The mixing plate has a cryoperm radiation shield, however we also shield each device within superconducting and mu-metal shields. Alternating between different shielding configurations, we see no obvious signs of flux noise [32] or quasiparticle induced dissipation [33] though our devices are less susceptible to these issues compared to superconducting qubit circuits.

2.3.2 Fridge circuit

Since it takes days to cycle our dilution refrigerator, we have added a set of passive microwave switches that allow us to probe up to 6 different devices with the same fridge circuit. Our switches are commercially available from Radiall. We learned about them from other research groups that modify these switches for optimal operation at cryogenic temperatures [34], though we initially installed our switches out of the box (unmodified). For a single switching operation composed of two pairs of reset and set pulses, we typically heat our mixing plate

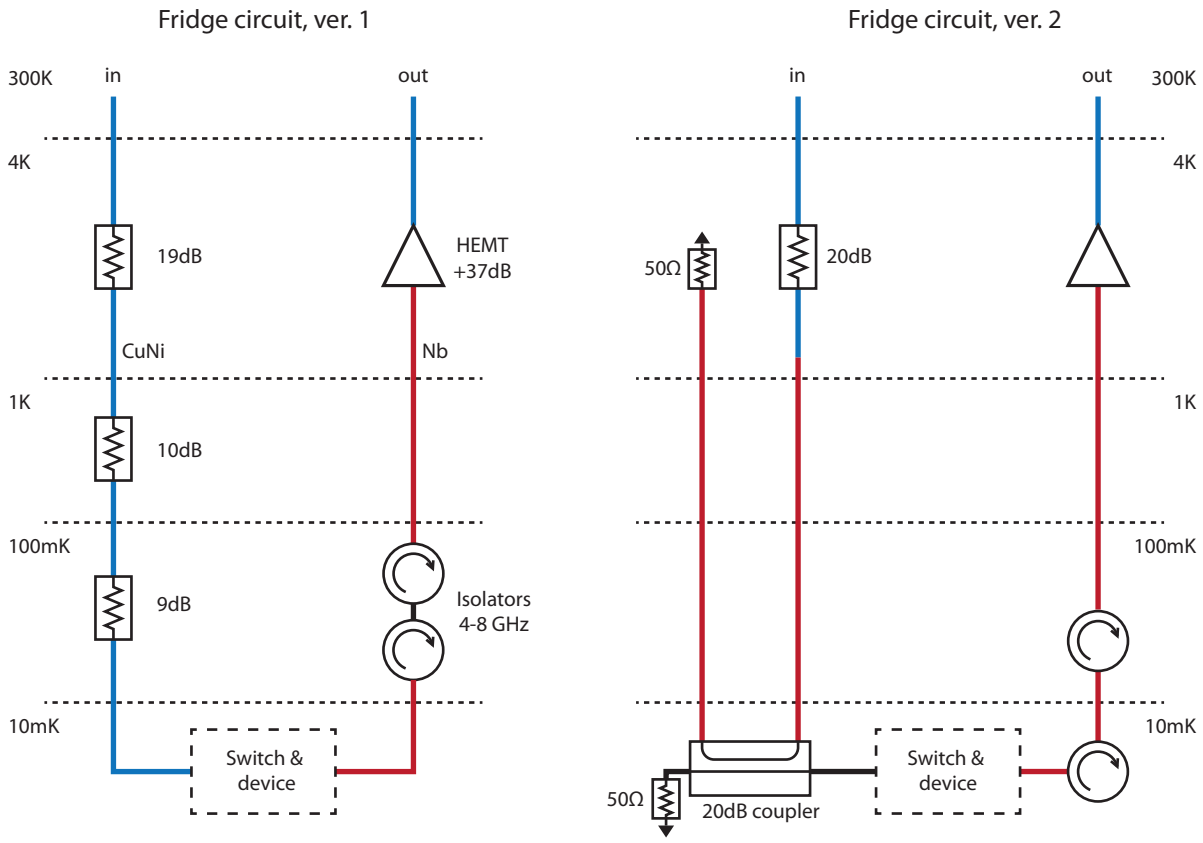

Figure 2.6: Fridge circuit. **a.** Version 1 as used in asymmetry and BAE measurements. An input waveguide composed of copper-nickel coax (blue) provides approximately 55dB of total attenuation to sufficiently suppress room temperature Johnson noise. The output of the device runs to a cryogenic amplifier (HEMT) at 4K through superconducting niobium coax (red). A pair of isolators cut out the 4K noise radiating back from the amplifier. **b.** Version 2 as used in squeezing measurements. To reduce heating of the mixing plate due to Ohmic heating of attenuators under intense microwave drive, the input line utilizes a directional coupler that does not dissipate the incident power. Furthermore, the first stage of the attenuator is shifted to the mixing plate to ensure the output port is in the ground state ($n_r^{th} = 0$).

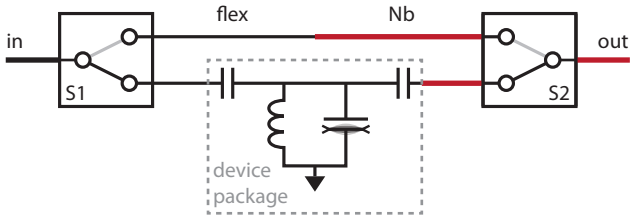

Figure 2.7: Switching circuit. Multiplexing with a latching microwave switch allows up to five sample packages and an impedance matched through connection to be accessed in a single cooldown.

to nearly 150mK, requiring between 30min - 90min to cool back down to base temperature depending on the fridge pump configuration. This is a minor nuisance for the kinds of experiments we do though modifying the switches is something that should be done in the future.

To probe the device, the fridge is wired with separate input and output microwave coax lines. The input lines is composed mainly of CuNi coax with an additional 40dB of isolation distributed over the dilution fridge stage temperatures. This isolation filters out room temperature Johnson noise while minimizing ohmic heating and re-emission of thermal noise from attenuators. On the output side, superconducting Niobium coax feeds the microwave signals first through a pair of circulators and then to a cyrogenic amplifier at 4K. The circulators provide over 25dB of isolation from 4K noise radiating out of the input port of the amplifier. The cryogenic amplifier is a cryogenic compatible low noise HEMT amplifier with gain of 37dB and a noise temperature of 3.6K (manufactured at Caltech by S. Weinreb). The signals are then fed out to room temperature analysis. Refer to Fig. 2.6 for details of the fridge circuit.

2.3.3 Drive circuit

For our measurements we rely on intense multi-tone pumping as well as weak noise injection. To achieve this, we construct the circuit outline in Fig. 2.8. Multiple drive tones are produced either via independent single tone sources, coupled into the same line with passive summers or direction couplers, or with a multi-tone vector source (Agilent E8267C). At the necessary

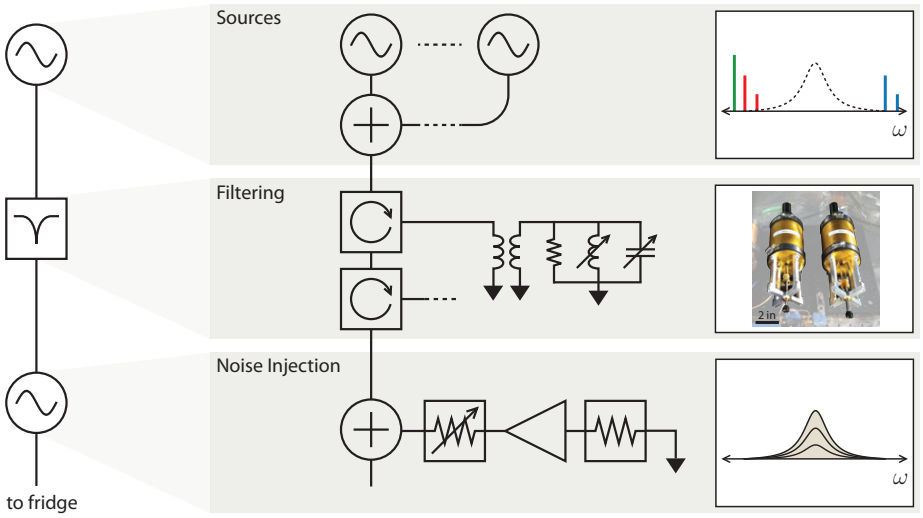

Figure 2.8: Drive circuit.**a.** Multiple microwave sources, both single tone and vector sources, are summed generate the desired pump configuration. **b.** A bank of room temperature filter cavities isolate source phase noise to ensure the cavity does not get excited by classical noise on the input line. **c.** Noise injection. A white noise source can selectively inject classical noise into the cavity on the order of one to ten microwave photons.

powers, the phase noise of the sources at detunings near ω_m is large enough to directly excited our microwave cavity with sufficiently large classical noise.

To remedy this, we implement a bank of tunable copper-can filter cavities that isolate injected phase noise by over 30dB (typically 50dB) over a narrow band $\approx$ 450 kHz. These cavities are mounted at room temperature and typically have loaded quality factors of Q$\sim 5 \times 10^3$. Depending on measurement requirements, the cavities can be set up in either transmission or rejection mode and hence can serve either as bandpass filters or notch filters.

Despite all of this filtering, we then add a pseudo-white microwave noise source to inject a weak amount of classical microwave noise into our circuit. The purpose of this noise is to allow us control over classical occupation of the microwave resonator with occupations on the order of one. This serves as an important measurement feature since our system almost always exhibits classical noise effects. By controlling the amount of classical noise in the cavity, we can calibrate out classical noise contributions and reveal the desired quantum behavior.

Chapter 3

Sideband asymmetry

3.1 Introduction

A fascinating aspect of quantum measurement is that the outcome of experiments and the apparent nature of the object under study depend critically on the properties of both the system and the measurement scheme [35]. An excellent illustration is found when considering measurements of the quantum harmonic oscillator. If measured with an ideal energy detector, the observed signals will demonstrate energy level quantization [36, 37]; measured instead with an ideal position detector, no evidence of quantized energy levels are found and the measured signals appear to be that of a very cold, classical oscillator [6, 18]. The details of the measurement are as essential to the apparent nature of the system under study as the properties of the system itself – succinctly expressed by Roy Glauber: "A photon is what a photodetector detects." [38]

To describe the measured noise of quantum systems, it is often useful to make use of so-called quantum noise spectral densities, which in general are not symmetric functions of frequency: $S_{xx}(-\omega) \neq S_{xx}(+\omega)$, where $S_{xx}(\omega)$ is the spectral density of the observable $x(t)$, defined as the Fourier transform of $\langle \hat{x}(t)\hat{x}(0)\rangle$ [11]. For a quantum harmonic oscillator, the negative and positive frequency sides of this spectral density describe the ability of the

system to emit or absorb energy,

$$S_{xx}[\omega] = \int d\omega e^{i\omega t} \langle \hat{x}(t)\hat{x}(0) \rangle \tag{3.1}$$

$$= x_{\mathrm{zp}}^2 |\chi_m(-\omega)|^2 \gamma_m n_m^{th} + x_{\mathrm{zp}}^2 |\chi_m(\omega)|^2 \gamma_m \left(n_m^{th} + 1\right), \tag{3.2}$$

with the mechanical susceptibility defined as $\chi_m(\omega)s = [-i(\omega - \omega_m) + \gamma_m/2]^{-1}$. In the ground state, $n_m^{th} = 0$, there is no ability for the harmonic oscillator to emit energy so that $S_{xx}(-\omega_m) = 0$. It can, however, absorb energy and as a result, $S_{xx}(+\omega_m) = \frac{4}{\gamma_m} x_{\mathrm{zp}}^2$, where $x_{\mathrm{zp}} = \sqrt{\hbar/2m\omega_m}$ is the amplitude of zero point fluctuations for a mechanical oscillator with mass m, resonance frequency ω_m, and damping rate γ_m. This asymmetric-in-frequency motional noise spectrum was first measured in atomic systems prepared in quantum ground states of motion [39–41], where the motional sideband absorption and fluorescence spectra were detected via photodetection.

Analogous quantum noise effects can also be studied in macroscopic mechanical systems, using electro-mechanical and opto-mechanical devices prepared and probed at quantum limits [6, 7, 10, 42]. These systems exhibit the Raman-like processes of up and down conversion of photons, resulting from the parametric coupling between mechanical motion and electromagnetic modes of a resonant cavity; the rates of these processes should naturally mirror the asymmetry in the mechanical quantum noise spectral density $S_{xx}(\pm\omega_m)$. Recent experiments in optomechanics have demonstrated this expected imbalance between up and down converted sidebands [43, 44]. Here, we demonstrate the analogous physics in a quantum circuit, where it is now microwave photons (not optical photons) which probe the mechanical motion.

3.1.1 Toy model

As a first step to understand how the motional sideband asymmetry manifests in an electromechanical system probed through the cavity mode, we consider the following simplified expressions for the microwave noise spectrum. For a single microwave drive at ideal red

($\Delta = -\omega_m$) and blue ($\Delta = \omega_m$) detunings, the Langevin equation for the cavity operator under RWA is

$$\chi_c^{-1}(\omega)\hat{d}[\omega] = -\sqrt{\kappa}\,\hat{d}_{\text{in}}[\omega] - iG_{\mp}\,\hat{b}^{(\dagger)}[\omega],$$

where $\hat{b}$ ($\hat{b}^\dagger$) and $G_{\mp}$ is associated with detuning $\Delta = \pm\omega_m$.

The microwave noise spectrum is specified by the output field correlators in the frequency domain. Relating the microwave correlators with the corresponding mechanical correlators yields different results depending on the drive detunings. For the up-converted signal,

$$\left.\begin{aligned}\langle \hat{d}^\dagger_{R,\text{out}}[\omega]\,\hat{d}_{R,\text{out}}[\omega']\rangle &\propto \langle \hat{b}^\dagger_{\text{in}}[\omega]\,\hat{b}_{\text{in}}[\omega']\rangle,\\ &\propto n_m^{th}\,\delta(\omega+\omega'),\end{aligned}\right\} \quad (\Delta = -\omega_m) \tag{3.3}$$

whereas the down-converted signal includes quantum fluctuations,

$$\left.\begin{aligned}\langle \hat{d}^\dagger_{R,\text{out}}[\omega]\,\hat{d}_{R,\text{out}}[\omega']\rangle &\propto \langle \hat{b}_{\text{in}}[\omega]\,\hat{b}^\dagger_{\text{in}}[\omega']\rangle,\\ &\propto (n_m^{th}+1)\,\delta(\omega+\omega'),\end{aligned}\right\} \quad (\Delta = \omega_m), \tag{3.4}$$

so it does appear that the detection of microwave sideband asymmetry serves as an accurate proxy for motional sideband asymmetry. Per the discussion in Sec. 1.3.1, however, linear microwave detection senses the symmetrized noise spectrum that is calculated as the average of both normal and antinormal ordered terms,

$$\left.\begin{aligned}\langle \{\hat{d}^\dagger_{R,\text{out}}[\omega]\,,\hat{d}_{R,\text{out}}[\omega']\}\rangle &\propto \langle \{\hat{b}_{\text{in}}[\omega]\,,\hat{b}^\dagger_{\text{in}}[\omega']\}\rangle,\\ &\propto (2n_m^{th}+1)\,\delta(\omega+\omega').\end{aligned}\right\} \quad (\Delta = \pm\omega_m). \tag{3.5}$$

Now it appears that the mechanical asymmetry is averaged out by the process of microwave measurement. What happened to the mechanical zero-point fluctuations? In the following, we will model this system within an input-output framework and resolve this contradiction.

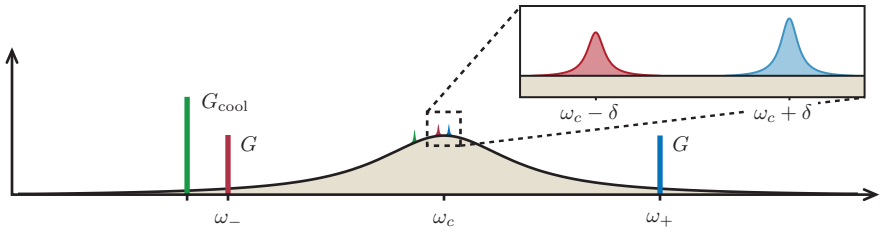

Figure 3.1: Sideband asymmetry pump configuration. Two probe tones (red and blue bar) monitor the up and down-converted motional sidebands while a third tone (green bar) cools the mechanics. The probe tones are balanced in power with associated optomechanical coupling strengthcs G and are detuned symmetrically about cavity resonance (black line) at frequencies $\omega_\pm = \omega_c \pm (\omega_m + \delta)$. The up-converted (red are) and down-converted (blue area) motional sidebands are sufficiently detuned to avoid sideband overlap. Generally, we assume the cavity is occupied with classical noise (beige area) that can mix down to produce real forces on the mechanics.

3.2 Optomechanical sideband asymmetry

For our analysis, we consider a sideband-resolved system simultaneously probed with two pumps at near ideal red- and blue-detunings. This model is useful because it closely resembles our measurement routine, models multitone effects that could arise between direct and indirect coupling between the probe tones, and simplifies to a single drive model in the limit of setting either probe amplitude to zero.

In contrast, the actual experiment consists of a two-port electro-mechanical system that we simultaneously pump with three microwave tones, all detuned from cavity resonance. Two balanced probe tones are detuned symmetrically about the cavity center and are used to simultaneously monitor the motional sidebands that are up- and down-converted near cavity resonance but with sufficient detuning to avoid sideband overlap. A third red-detuned cooling tone dampens the mechanical motion via dynamical back-action and is used to cool the mechanics to near the ground state. Refer to Fig. 3.1 for a schematic of the pump configuration. In a frame rotating at the cavity frequency ω_c, the drive Hamiltonian is

$$\hat{\mathcal{H}}_{\text{drive}} = \sum_{\nu=\pm} a_\nu (\hat{a} e^{i\nu(\omega_m+\delta)t} + \hat{a}^\dagger e^{-i\nu(\omega_m+\delta)t}) + a_{\text{cool}} (\hat{a} e^{i(\omega_m+\delta_c)t} + \hat{a}^\dagger e^{-i(\omega_m+\delta_c)t}), \tag{3.6}$$

where drive amplitudes are all assumed to be real. We will initially ignore the coupling to the cooling beam and instead model the electromechanical dynamics in response to the two

balanced drive tones. As we later show, separating the transduced sidebands (compared to the effective mechanical damping rate) allows one to treat the drives independently so that we will later incorporate the additional cooling tone without altering the following analysis.

3.2.1 Equations of motion

Following the steps in Sec. 1.4, we make unitary transformations to a rotating, displaced frame with $\hat{a} = e^{-i\omega_c t}[a(t) + \hat{d}]$ with $a(t) = \langle \hat{a} e^{i\omega_c t} \rangle$ and $\hat{b} = \hat{c} e^{-i(\omega_m + \delta)t})$. In this frame, the coherent drive amplitude follows

$$a(t) = a_- e^{i(\omega_m+\delta)t} + a_+ e^{i(\omega_m+\delta)t} + a_{\text{cool}} e^{i(\omega_m+\delta_c)t}, \tag{3.7}$$

where the phases of all drive tones can be arbitrarily defined and assumed zero so that $a_{\pm,\text{cool}}$ are real. This assumption holds for sufficiently large detunings $\delta, \delta_c \gg \gamma_{\text{tot}}$ that suppress any direct correlations between the separate drives. If this were not the case, the relative phases between the drive tones could play an important role. Along the lines that the probe tones act independently, the cooling tone will be temporarily ignored. Now, the interaction Hamiltonian becomes $\hat{\mathcal{H}}_{\text{int}} = \hat{\mathcal{H}}_{\text{lin}} + \hat{\mathcal{H}}_{CR}$, where

$$\hat{\mathcal{H}}_{\text{lin}} = -iG_-(\hat{d}\,\hat{b}^\dagger + \hat{d}^\dagger \hat{b}) - iG_+(\hat{d}\,\hat{b} + \hat{d}^\dagger \hat{b}^\dagger), \tag{3.8}$$

$$\hat{\mathcal{H}}_{CR} = -iG_- e^{i2\omega_m t}(\hat{d}\,\hat{b} + \hat{d}^\dagger \hat{b}^\dagger) - iG_+ e^{-2i\omega_m t}(\hat{d}\,\hat{b}^\dagger + \hat{d}^\dagger \hat{b}). \tag{3.9}$$

The enhanced optomechanical couplings are defined via the microwave amplitudes, $G_\pm = g_0 a_\pm$, which lead to optical scattering rates $\gamma_{\text{op}}^\pm = \frac{4G_\pm}{\kappa}$. Given that we typically operate in the sideband-resolved regime, we make the rotating wave approximation and only treat the linear contribution, though we can later incorporate counter-rotating effects if necessary.

With Eq. (3.8) and standard input-output relations, the Heisenberg-Langevin equations in the frequency domain are formatted in matrix notation: $\hat{\boldsymbol{D}}[\omega] = \boldsymbol{\chi}(\omega) \cdot \boldsymbol{L} \cdot \hat{\boldsymbol{D}}_{\mathbf{in}}[\omega]$, with mode operators $\hat{\boldsymbol{D}} = (\hat{d}, \hat{d}^\dagger, \hat{b}, \hat{b}^\dagger)^T$, bath operators $\hat{\boldsymbol{D}}_{\mathbf{in}} = (\hat{d}_{\text{in}}, \hat{d}^\dagger\text{in}, \hat{b}\text{in}, \hat{b}^\dagger\text{in})^T$, and $\boldsymbol{L} = \text{diag}(\sqrt{\kappa}, \sqrt{\kappa}, \sqrt{\gamma_m}, \sqrt{\gamma_m})$. As before, the microwave input field is defined as the weighted

average over the bath contributions from the input (L), output (R), and internal (int) ports, $\hat{d}_{\rm in} = \sum_{\sigma=L,R,{\rm int}} \sqrt{\kappa_\sigma/\kappa}\, \hat{d}_{\sigma,{\rm in}}$.

To reiterate, the inverse scattering matrix for this system is

$$\boldsymbol{\chi}^{-1}(\omega) = \begin{bmatrix} \frac{\kappa}{2} - i\omega & 0 & -iG_- & -iG_+ \\ 0 & \frac{\kappa}{2} - i\omega & iG_+ & iG_- \\ -iG_- & -iG_+ & \frac{\gamma_m}{2} - i(\omega+\delta) & 0 \\ iG_+ & iG_- & 0 & \frac{\gamma_m}{2} - i(\omega-\delta) \end{bmatrix}. \tag{3.10}$$

The relevant scattering parameters are discussed below.

3.2.2 Zero-point bath designations

The bath commutators and correlations for the microwave and mechanical bath operators are given by Eqs. (1.94)-(1.97). In the following analysis, we will instead designate the bath commutation relations with separate variables α and β:

$$[\hat{d}_{\sigma,{\rm in}}(t), \hat{d}^\dagger_{\sigma,{\rm in}}(t')] = \alpha\delta(t-t'), \tag{3.11}$$

$$[\hat{b}_{\rm in}(t), \hat{b}^\dagger_{\rm in}(t')] = \beta\delta(t-t'). \tag{3.12}$$

Here, α represents the quantum fluctuations of the microwave field while β represents those of the mechanics. Similarly, the updated bath correlations read

$$\langle \hat{d}_{\sigma,{\rm in}}(t)\hat{d}^\dagger_{\sigma,{\rm in}}(t')\rangle = (n_c^{th} + \alpha)\delta(t-t'), \tag{3.13}$$

$$\langle \hat{b}_{\rm in}(t)\hat{b}^\dagger_{\rm in}(t')\rangle = (n_m^{th} + \beta)\delta(t-t'). \tag{3.14}$$

Formally, the field operators obey the canonical commutation relations such that $\alpha = \beta = 1$. The purpose of this labeling is not to adjust the commutation relations but rather to provide a straightforward method to track how the microwave and mechanical fluctuations propagate throughout the measurement. The ultimate goal of such a labeling scheme is to

help clarify the origins of the sideband asymmetry: does the observed asymmetry stem from zero-point motion of the mechanics or the shot noise of the microwave field?

3.2.3 Dressed mechanics

As a first consistency check, we can explore how the motional noise power is modified by electro-mechanical coupling with microwave drive tones at near ideal red- and blue-detunings. The Langevin equation for the mechanical operator $\hat{b}$ (defined in the frame rotating at $\omega_m+\delta$) is defined via the scattering parameters

$$\hat{b} = \boldsymbol{\chi}_{31}\sqrt{\kappa}\hat{d}_{\text{in}} + \boldsymbol{\chi}_{32}\sqrt{\kappa}\hat{d}^{\dagger}_{\text{in}} + \boldsymbol{\chi}_{33}\sqrt{\gamma_m}\hat{b}_{\text{in}} + \boldsymbol{\chi}_{34}\sqrt{\gamma_m}\hat{b}^{\dagger}_{\text{in}}, \tag{3.15}$$

where all explicit frequency dependence has been omitted. In this notation, the mechanical susceptibility is given by the scattering factor $\boldsymbol{\chi}_{33}$. We can explicitly calculate the change in the mechanical frequency and damping due to the interaction with the cavity by looking at the corresponding"self energy" (i.e. difference in inverse mechanical susceptibilities evaluated on resonance with and without the cavity, see e.g. [45]). Making the rotating-wave approximation ($\omega \ll \kappa$) and assuming sufficient frequency separation between the sidebands ($\delta \gg \gamma_{\text{tot}}$), the total mechanical damping is

$$\gamma_{\text{tot}} = 2\text{Re}\left[\boldsymbol{\chi}_{33}^{-1}(\omega_m)\right] \tag{3.16}$$

$$= \gamma_m + \gamma_{\text{op}}^{-} - \gamma_{\text{op}}^{+}, \tag{3.17}$$

while the optical spring shift is

$$\delta\omega_m = \text{Im}\left[\boldsymbol{\chi}_{33}^{-1}(\omega_m)\right] \tag{3.18}$$

$$= -\frac{\delta}{\kappa}(\gamma_{\text{op}}^{+} - \gamma_{\text{op}}^{-}). \tag{3.19}$$

Note that in both the damping and frequency shift, the effects of the red- and blue-detuned drives conspire to cancel.

We can now calculate the motional noise spectrum in the lab frame, where we assume the mechanics is in the high-Q limit so that the sidebands are tightly confined at positive and negative frequencies and the bath operators can be assumed to behave Markovian:

$$\begin{aligned}
S_{xx}[\omega] =& \int dt e^{i\omega t}\langle\hat{x}(t)\hat{x}(0)\rangle, \\
=& \quad x_{\mathrm{zp}}^2\left\{|\boldsymbol{\chi}_{31}(\omega)|^2+|\boldsymbol{\chi}_{32}(-\omega)|^2\right\}\kappa(n_c^{th}+1) \\
&+ x_{\mathrm{zp}}^2\left\{|\boldsymbol{\chi}_{32}(\omega)|^2+|\boldsymbol{\chi}_{31}(-\omega)|^2\right\}\kappa n_c^{th} \\
&+ x_{\mathrm{zp}}^2\left\{|\boldsymbol{\chi}_{33}(\omega)|^2+|\boldsymbol{\chi}_{34}(-\omega)|^2\right\}\gamma_m(n_m^{th}+1) \\
&+ x_{\mathrm{zp}}^2\left\{|\boldsymbol{\chi}_{34}(\omega)|^2+|\boldsymbol{\chi}_{33}(-\omega)|^2\right\}\gamma_m n_m^{th}, \\
=& \frac{\gamma_{\mathrm{tot}}}{(\omega-\omega_m)^2+(\frac{\gamma_{\mathrm{tot}}}{2})^2}\,x_{\mathrm{zp}}^2\left(n_m+\tilde{\beta}\right)+\frac{\gamma_{\mathrm{tot}}}{(\omega+\omega_m)^2+(\frac{\gamma_{\mathrm{tot}}}{2})^2}\,x_{\mathrm{zp}}^2 n_m.
\end{aligned}$$

Here the mechanical occupation factor is given by the detailed balance rate equation

$$n_m = \frac{\gamma_m n_m^{th}+\gamma_{\mathrm{op}}^- n_c^{th}+\gamma_{\mathrm{op}}^+(n_c^{th}+\alpha)}{\gamma_{\mathrm{tot}}}, \tag{3.20}$$

while $\tilde{\beta}$ denotes the zero point fluctuations of the dressed mechanical mode with coupling to both the intrinsic mechanical bath and additional optical bath channels,

$$\tilde{\beta} = \frac{\gamma_m\beta+(\gamma_{\mathrm{op}}^- - \gamma_{\mathrm{op}}^+)\alpha}{\gamma_{\mathrm{tot}}} = 1. \tag{3.21}$$

In the limit of sufficiently small cooperativity ($\frac{\gamma_{\mathrm{op}}^{\pm}}{\gamma_m} \ll 1$) or carefully balanced drives ($\gamma_{\mathrm{op}}^+ = \gamma_{\mathrm{op}}^-$), the mechanical fluctuations consist almost entirely of the zero-point fluctuations of the intrinsic bath $\tilde{\beta} \to \beta$. For a large red-detuned drive ($\gamma_{\mathrm{tot}} \gg \gamma_m$), the optical damping dominates over the intrinsic dissipation and the mechanical dynamics is entirely determined by the microwave field fluctuations, $\tilde{\beta} \to \alpha$.

This behavior is notable for two reasons. First, the optical contribution to the mechanical fluctuations ensures that the backaction-imprecision product for position measurement obeys a strict lower bound enforced by quantum mechanics [11]. It would appear from Eq. (3.20)

that a single red-detuned drive with high cooperativity ($\gamma_{\rm tot} \simeq \gamma_{\rm op}^{-}$) pumping a cavity with zero classical noise ($n_c^{th} = 0$) generates no back-action heating of the mechanical mode and the detector noise product would be zero. This argument is incorrect because it ignores the contribution of the quantum fluctuations of the optical field. The pump-dependent asymptotic heating of $\tilde{\beta}$ serves as the measurement back-action and ensures adherence to quantum bounds.

Second, distinguishing between the source of "quantum motion" is a serious issue for measurements that aim to detect mechanical zero-point fluctuations. If such a measurement implies the detection of the intrinsic mechanical bath, then the optically-induced damping must be small. If instead the purpose of such an asymmetry measurement is to measure quantum-induced motion, i.e., the mechanical response to quantum fluctuations of either the intrinsic microwave or mechanical noise, then the source of such fluctuations is not relevant. In this view, there is no limit to the back-action induced damping, which is more aligned with typical measurement schemes to date, i.e., most systems require intense red-detuned pumping to generate sideband cooling near the motional ground state. However, in such a limit the mechanical signal can be treated as a classical transducer of microwave noise and the sideband asymmetry is then traced entirely back to the quantum shot noise of the microwave field, regardless of how the noise is measured. From this viewpoint, such a measurement is closely related to experiments that detect the shot noise of electromagnetic fields via back-action heating of macroscopic mechanical transducers [10, 42].

To date, sideband asymmetry has been measured in mesoscopic mechanical resonators cooled near the ground state via either passive cooling [46] or active sideband-cooling [16, 43, 44, 47], and thus both high and low cooperativity regimes ($\gamma_{\rm tot} \simeq \gamma_m$ vs. $\gamma_{\rm tot} \gg \gamma_m$) have been explored. To simplify notation in what follows, we will ignore the subtlety in defining "quantum motion" in an electromechanical device and associate $\tilde{\beta} \to \beta$ with intrinsic zero-point fluctuations of the mechanics.

As a final note, the symmetrized mechanical noise spectrum scales as expected,

$$\bar{S}_{xx}[\omega] = \frac{1}{2}\int dt e^{i\omega t}\langle\{\hat{x}(t),\hat{x}(0)\}\rangle, \tag{3.22}$$

$$= \frac{x_{\rm zp}^2\gamma_{\rm tot}}{(|\omega|-\omega_m)^2+(\frac{\gamma_{\rm tot}}{2})^2}\left(n_m+\frac{\tilde{\beta}}{2}\right). \tag{3.23}$$

3.2.4 Microwave spectrum

Amplitude of the output field $\hat{V}_{\rm out}(t) = \hat{d}_{R,\rm out}(t) + \hat{d}^\dagger_{R,\rm out}(t)$. The output operator defined via standard input-output relations $\hat{d}_{\sigma,\rm out} = \hat{d}_{\sigma,\rm in} - \sqrt{\kappa_\sigma}\hat{d}$. In terms of the scattering parameters,

$$\hat{d}_{R,\rm out} = \hat{d}_{R,\rm in} - \boldsymbol{\chi}_{11}\sqrt{\kappa_R\kappa}\hat{d}_{\rm in} - \boldsymbol{\chi}_{12}\sqrt{\kappa_R\kappa}\hat{d}^\dagger_{\rm in} - \boldsymbol{\chi}_{13}\sqrt{\kappa_R\gamma_m}\hat{c}_{\rm in} - \boldsymbol{\chi}_{14}\sqrt{\kappa_R\gamma_m}\hat{c}^\dagger_{\rm in}. \tag{3.24}$$

For illustrative purposes, we present the scattering parameters for the microwave field assuming weak coupling ($\kappa \gg \gamma_{\rm tot}$) and large sideband separation ($\delta \gg \gamma_{\rm tot}$):

$$\boldsymbol{\chi}_{11}(\omega) = \frac{2}{\kappa}\left[1+\sum_{\pm}\frac{\pm\gamma_{\rm op}^{\pm}}{\gamma_{\rm tot}-2i(\omega\mp\delta)}\right], \tag{3.25}$$

$$\boldsymbol{\chi}_{12}(\omega) = \frac{2}{\kappa}\sum_{\pm}\frac{\pm\sqrt{\gamma_{\rm op}^{+}\gamma_{\rm op}^{-}}}{\gamma_{\rm tot}-2i(\omega\mp\delta)}, \tag{3.26}$$

$$\boldsymbol{\chi}_{13}(\omega) = \frac{2\sqrt{\gamma_{\rm op}^{-}}}{\gamma_{\rm tot}-2i(\omega+\delta)}, \tag{3.27}$$

$$\boldsymbol{\chi}_{14}(\omega) = \frac{2\sqrt{\gamma_{\rm op}^{+}}}{\gamma_{\rm tot}-2i(\omega-\delta)}. \tag{3.28}$$

Note that $\boldsymbol{\chi}_{11}$ captures the various different ways cavity noise can propagate through the system. As we discuss below, $|\boldsymbol{\chi}_{11}|^2$ will contain non-vanishing mixing terms that can be interpreted either as interference between scattering channels or as correlations between back-action and imprecision measurement noise.

For calibration, we typically measure the complex transmission through the device, given by

$$S_{21}(\omega) = -\sqrt{\kappa_L\kappa_R}\boldsymbol{\chi}_{11}. \tag{3.29}$$

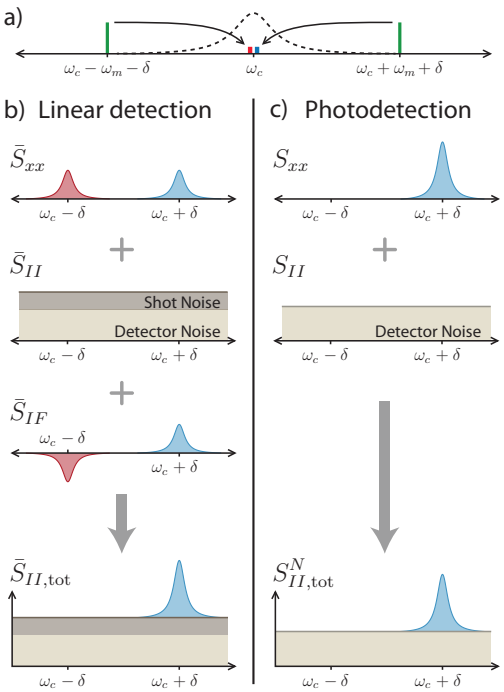

Figure 3.2: Comparison between linear detection and photon counting. **a.** Pump scheme. We consider a single microwave cavity (dotted line) pumped at $\omega_c \pm (\omega_m + \delta)$ (green bars). The up -converted (red bar) and down-converted (blue bar) motional sidebands are placed tightly within the cavity linewidth. For figure clarity, the occupations of the microwave and mechanical modes are assumed to be zero. **b.** Linear detection. The quantum contribution from the symmetrized motional noise $\bar{S}_{xx}$ is present in both sidebands. Microwave shot noise (brown band) and amplifier noise (beige band) combine to form the imprecision noise $\bar{S}_{II}$. This measurement is sensitive to noise correlations between the microwave and mechanical odes ($\bar{S}_{IF}$), which results in asymmetric squashing (red region) and antisquashing (blue region) of the noise floor. **c.** Photodetection. Normal-ordered detection is sensitive to the asymmetric motional noise spectrum S_{xx}. The detector is not sensitive to microwave shot noise, and the noise floor (S_{II}) is from detector nonidealities (beige band), analogous to dark counts for a photodetector. Although the source is different, the sideband imbalance is identical in both photodetection and linear detection.

3.2.5 Symmetric noise detection

Since we implement a linear detection scheme in this experiment, we construct the symmetrized microwave noise spectrum by substituting the above scattering parameters into the expression for symmetric detection, except now the mechanical and microwave zero-point

bath fluctuations are separately specified:

$$\bar{S}_R[\omega] = \int dt e^{i\omega t} \langle \{\hat{V}_{\rm out}(t), \hat{V}_{\rm out}(0)\}\rangle, \tag{3.30}$$

$$= \int dt e^{i\omega t} \langle \hat{d}^\dagger_{R,\rm out}(0)\hat{d}_{R,\rm out}(t) + \hat{d}_{R,\rm out}(t)\hat{d}^\dagger_{R,\rm out}(0)\rangle, \tag{3.31}$$

$$= \quad \kappa_R\kappa \left(|\chi_{11}|^2 + |\chi_{12}|^2\right) \left(n_c^{th} + \alpha/2\right) \tag{3.32}$$

$$+ \kappa_R\gamma_m \left(|\chi_{13}|^2 + |\chi_{14}|^2\right) \left(n_m^{th} + \beta/2\right) \tag{3.33}$$

$$+ \left[1 - \kappa_R \left(\chi_{11} + \chi_{11}^*\right)\right] \left(n_r^{th} + \alpha/2\right), \tag{3.34}$$

$$= \bar{S}_o + \frac{\kappa_R}{\kappa} \sum_{\pm} \frac{\gamma_{\rm tot}\gamma_{\rm op}^{\pm}}{(\omega \mp \delta)^2 + (\gamma_{\rm tot}/2)^2} \left[\left(n_m + \frac{\beta}{2}\right) \pm \left(n_{\rm eff} + \frac{\alpha}{2}\right)\right]. \tag{3.35}$$

The noise floor is

$$\bar{S}_o\left[\omega\right] = \frac{\alpha}{2} + n_r^{th} + \frac{4\kappa_R}{\kappa}(n_c^{th} - n_r^{th}), \tag{3.36}$$

and we have defined $n_{\rm eff} = 2n_c^{th} - n_r^{th}$. The noise floor is shaped by the cavity response due to interference from noise that reflects off the port correlated with noise that is re-radiated from the cavity. The underlying components of this spectrum are outlined in Fig. 3.2(b).

One sees explicitly that the sideband imbalance is proportional to $(2n_{\rm eff} + \alpha)$ and hence is entirely due to fluctuations in the microwave fields driving the cavity. This interpretation is true both when this noise is thermal and when it is purely quantum (i.e., $n_r^{th} = n_l^{th} = 0$). These terms in the spectrum result from the interference between the two ways the incident field noise can reach the output: either by directly being transmitted through the cavity or by first driving the mechanical resonator whose position then modulates the amplitude quadrature of the outgoing microwaves. This interference is the basic mechanism of noise squashing, which in the case of thermal noise was previously observed in a microwave-cavity-based electromechanical system [18]. This mechanism can also be fully described using a general linear measurement formalism [48], where it is attributed to the presence of correlations between the backaction and imprecision noise of the detector [9, 49].

The above calculation also shows that both the thermal and zero-point force noise emanating from the mechanical bath contribute symmetrically and hence play no role in de-

termining the asymmetry of the sidebands. This suggests that the sideband asymmetry observed using linear detection of the scattered field is not directly probing the asymmetric quantum noise spectrum of the mechanical mode.

To simplify the notation in the following, we consider the mechanical noise occupations inferred from the output spectrum about the up- and down-converted sidebands

$$n_m^{\pm} = \frac{1}{\gamma_{\rm op}^{\pm}} \frac{\kappa}{\kappa_R} \int \frac{d\omega}{2\pi} \left(\bar{S}_R[\omega \mp \delta] - \bar{S}_o \right) \tag{3.37}$$

$$= \left(n_m + \frac{\beta}{2} \right) \pm \left(n_{\rm eff} + \frac{\alpha}{2} \right). \tag{3.38}$$

3.2.6 Photon counting

An alternate measurement strategy to amplitude detection is to first filter the output signal to a narrow bandwidth around a frequency ω and then perform direct photodetection. One is thus measuring power directly without first measuring field amplitudes, and in a manner that is only sensitive to the absorption of photons. As a result, such a measurement is described by the normal ordered spectrum

$$\begin{aligned} S_R[\omega] = & \int dt e^{i\omega t} \langle \hat{d}^{\dagger}_{R,\rm out}(0) \hat{d}_{R,\rm out}(t) \rangle \\ = & \quad \kappa_R \kappa |\chi_{11}|^2 \, n_c^{th} \\ & + \kappa_R \kappa |\chi_{12}|^2 \, (n_c^{th} + \alpha) \\ & + \kappa_R \gamma_m |\chi_{13}|^2 \, n_m^{th} \\ & + \kappa_R \gamma_m |\chi_{14}|^2 \, (n_m^{th} + \beta) \\ & + \left[1 - \kappa_R \left(\chi_{11} + \chi_{11}^* \right) \right] n_r^{th}. \end{aligned}$$

Substituting in the above scattering parameters, we find

$$S_R\left[\omega\right] = S_o + \frac{\kappa_R}{\kappa} \sum_{\pm} \frac{\gamma_{\rm tot} \gamma_{\rm op}^{\pm}}{(\omega \mp \delta)^2 + (\gamma_{\rm tot}/2)^2} \left[\left(n_m + \frac{\beta}{2} \right) \pm \left(n_{\rm eff} + \frac{\beta}{2} \right) \right], \tag{3.39}$$

where the symmetrized noise floor is defined in the vicinity about cavity center as $S_o = \bar{S}_o - \frac{\alpha}{2}$.

3.2.7 Spectrum comparison

Comparing the symmetrized microwave noise spectrum with the normal-ordered spectrum, it is clear that the spectra appear identical up to a flat background given by the microwave shot noise,

$$\bar{S}_R[\omega] = S_R[\omega] + \frac{\alpha}{2}. \tag{3.40}$$

This is no coincidence. Both spectra are formally related via the canonical commutation relation of the output microwave field

$$[\hat{d}_{R,\mathrm{out}}(t), \hat{d}^{\dagger}_{R,\mathrm{out}}(t')] = \alpha\delta(t - t'). \tag{3.41}$$

Regardless of the physical details of the detection scheme, if one assumes this commutation relation, then one can legitimately interpret symmetric or normal-ordered detection as measuring the same thing. On a formal level, this substitution requires that the input fluctuations of the microwave and mechanical baths are identical. If $\alpha \neq \beta$, the output commutator would differ from the input commutator,

$$\left[\hat{d}_{R,\mathrm{out}}(\omega), \hat{d}^{\dagger}_{R,\mathrm{out}}(\omega')\right] = \left[\alpha + \sum_{\pm} \frac{\pm\gamma_m\gamma^{\pm}_{\mathrm{op}}}{(\omega \mp \delta)^2 + (\gamma_{\mathrm{tot}}/2)^2}(\beta - \alpha)\right]\delta(\omega + \omega'). \tag{3.42}$$

This commutation relationship is associated with the relationship between detector absorbs and emits energy into the system. There is a fundamental difference between the two detection schemes: linear detection is sensitive to both absorption and emission of photons (and hence does sense the microwave quantum shot noise) whereas photon counting only absorbs energy from the environment (and hence does not sense the shot noise fluctuations of the electromagnetic field). If the purpose of the sideband asymmetry experiment is to directly compare the rates of energy scattering into and out of the mechanical mode, then one can interpret the commutator substitution as also asserting the mechanical commutator.

However, a deeper issue is that it is beyond the scope of input-output theory to tune the mechanical commutator since such a model would violate the canonical commutator for the output microwave field.

In the face of such subtleties, we adhere to the interpretation that most closely approaches the physical techniques used in the measurement: sideband asymmetry with symmetric detection is most naturally attributed to the shot noise of the microwave field. Similarly, sideband asymmetry via photon counting is most naturally attributed to the zero-point fluctuations of the mechanical bath.

As a final note, Eq. (3.42) is asymptotically true for $\gamma_{\rm tot}/\gamma_m \to \infty$ with $\alpha \neq \beta$, which again supports the idea that under large optical damping, the mechanics acts as a classical transducer responding to the microwave fluctuations. In this limit, the asymmetry is attributed to the shot noise of the microwave field regardless of the choice of detection scheme or choice of interpretation.

3.2.8 Cooling tone

So far, we have modeled the motional sidebands transduced via two probe tones while ignoring a third cooling tone. From the format of Eq. (3.35), we can now generalize the system to additional drive tones.

Assuming large frequency separation of the sidebands, the probe tones indirectly interact by modifying the mechanical susceptibility and mechanical occupation factor. Following the same behavior as the red-detuned probe, the additional cooling tone mainly increases the mechanical damping rate and subsequently cools the mechanical occupation factor c.f. Eq. (3.20). To reflect this behavior, the mechanical parameters in Eq. (3.35) are updated to capture the effects of the cooling tone:

$$\gamma_M = \gamma_m + \gamma_{\rm op}^{\rm cool}, \tag{3.43}$$

$$\gamma_M n_M^{\rm th} = (\gamma_m n_m^{th} + \gamma_{\rm op}^{\rm cool} n_c^{th}). \tag{3.44}$$

We consider moderate cooling in the weak-coupling regime and hence ignore deviations that arise from strong coupling or bad cavity corrections.

3.3 Results

Having explored the interpretation subtleties associated with sideband asymmetry, we now turn to presenting the experimental observation of this imbalance in a microwave-cavity based electromechanical system.

Our system is composed of a superconducting microwave resonator, also referred to as "cavity", where the resonance frequency is modulated by the motion of a compliant membrane. This frequency modulation leads to the desired parametric coupling between microwave field and mechanical motion (Fig. 3.3(a)). Measurements of the cavity response below 100 mK yield the resonance frequency $\omega_c = 2\pi \times 5.4$ GHz, total loss rate $\kappa = 2\pi \times 860$ kHz, output coupling rate $\kappa_R = 2\pi \times 450$ kHz, and input coupling rate $\kappa_L = 2\pi \times 150$ kHz. The capacitor top gate is a flexible aluminum membrane (40μm$\times 40\mu$m$\times$150nm) with a fundamental drumhead mode with resonance frequency $\omega_m = 2\pi \times 4.0$ MHz and intrinsic loss rate $\gamma_m = 2\pi \times 10$ Hz at 20mK. Motional displacement of the top gate modulates the microwave resonance frequency with an estimated coupling rate of $g_0 = \frac{\partial \omega_c}{\partial x} x_{\mathrm{zp}} = 2\pi \times 16$ Hz.

In Fig. 3.3(c), we present a schematic of the measurement configuration used in this work. Tunable cavity filters at room temperature reduce the source phase noise to the thermal noise level at 300K; cryogenic attenuators further reduce the noise down to the shot noise level [18]. A pair of microwave switches at the device stage select between the device or a bypass connection for high precision noise floor calibration of the cryogenic amplifier. The output signal passes through two cryo-circulators at $\sim$100mK followed by a cryogenic low-noise amplifier at 4.2K, and finally to a room temperature circuit for analysis. The occupation factor of the microwave resonator, n_c^{th}, which is expected to thermalize below 5×10^{-3} at temperatures below 50mK, can be increased and controlled by the injection of microwave frequency noise from amplified room temperature Johnson noise. From careful measurements

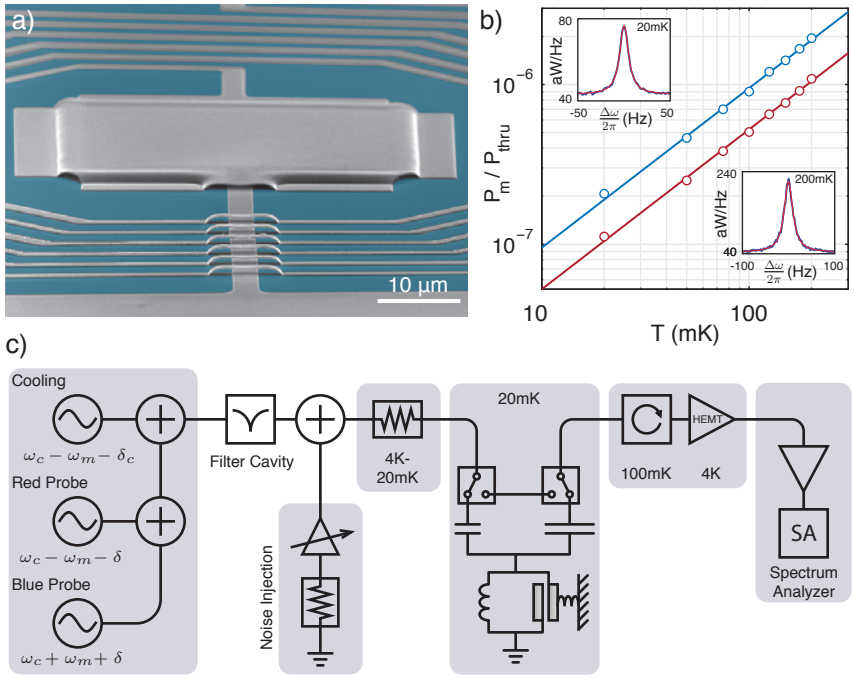

Figure 3.3: Device, calibration, and measurement scheme. **a.** Electron micrograph of the measured device. A suspended aluminum (grey) membrane patterned on silicon (blue) forms the electro-mechanical capacitor. It is connected to the surrounding spiral inductor to form a microwave resonator. Out of view, coupling capacitors on either side of the inductor couple the device to input and output co-planar waveguides. **b.** Motional sideband calibration. The cryostat temperature is regulated while the mechanical mode is weakly probed with microwave tones set at $\omega_c + \omega_m + \delta$ (blue) and at $\omega_c - \omega_m - \delta$ (red) detunings, with $\delta = 2\pi \times 500$ Hz. The observed linear dependence provides the calibration between the normalized sideband power and the mechanical occupation factor. Inset, up-converted motional sideband spectra collected at 20mK (top) and 200mK (bottom), with $\Delta\omega = \omega - (\omega_c - \delta)$. **c.** Schematic of the microwave measurement circuit.

of the noise power emanating from the cavity at zero pumping and comparing this to power spectra with the bypass switched in place, we conclude that there is a small contribution to n_c^{th} due to thermal radiation from the isolated port of the cryogenic circulators, given by the occupation factor $n_r^{th} = 0.34 \pm 0.03$.

When a single microwave tone is applied to the device at ω_p, the parametric coupling converts mechanical oscillations at ω_m to up and down-converted sidebands at $\omega_p \pm \omega_m$. In this experiment, we apply microwave tones at frequencies near $\omega_c \pm \omega_m$ and at powers given by the mean number of photons in the resonator, n_p. The microwave resonance suppresses motional sidebands outside of the linewidth and we consider only the contributions of signals converted to frequencies near ω_c. These are the Lorentzian components of the noise power spectra of Eq. (3.35), which for the remainder of the paper are denoted by "+" and "-", respectively.

Throughout the measurement, we simultaneously apply three microwave tones. We place a cooling tone at $\omega_c - \omega_m - \delta_c$ to control the effective mechanical damping rate, γ_M, and mode occupation, n_m, via back-action cooling [45, 50]. Two additional probe tones, placed at $\omega_c \pm (\omega_m + \delta)$, produce up and down converted sidebands symmetrically detuned from cavity center (Fig. 3.5(a)). The detunings are chosen to ensure no interference between the sidebands ($\delta_c = 2\pi \times 30$ kHz, $\delta = 2\pi \times 5$ kHz) so that we may consider the probe sidebands as independent measurements of the dressed mechanical mode.

3.3.1 Calibrations

To convert the motional sideband powers into equivalent mechanical occupation, we turn off the cooling tone and measure the probe sidebands ($\delta = 2\pi \times 500$ Hz) with low optical damping ($n_p^+ = n_p^- \simeq 5 \times 10^2$) and high mechanical occupation set by the cryostat temperature. Regulating the temperature to calibrated levels between 20 to 200mK, we calculate the integrated noise power under the sideband Lorentzians, $P_m^{\pm}$, normalized by the respective microwave probe power transmitted through the device, $P_{\text{thru}}^{\pm}$. In the limit of high thermal occupation, the normalized power is directly proportional to n_m [51]. As we vary

the cryostat temperature, T, we compare the normalized power to the thermal occupation factor $[\exp(\frac{\hbar\omega_m}{k_B T}) - 1]^{-1}$ (Fig. 3.3(b)). A linear fit yields the conversion factors for the up-converted (n_m^-) and down-converted (n_m^+) sidebands: $n_m^- = (9.9 \pm 0.2) \times 10^8 \cdot P_m^+ / P_{\text{thru}}^+$ and $n_m^+ = (5.4 \pm 0.1) \times 10^8 \cdot P_m^- / P_{\text{thru}}^-$. The factor of c.a. two between calibration factors at the two pump detunings is due to the presence of a parasitic bypass channel in the microwave circuit that allows pump signals to weakly transmit across the input and output ports of the device while completely bypassing the microwave resonator (see Sec. 1.1.3).

3.3.2 Sideband ratio and imbalance

Further detuning the probe tones ($\delta = 2\pi \times 5$ kHz) and turning on the cooling tone ($\delta_c = 2\pi \times 30$ kHz), we explore the sideband ratio, n_m^+/n_m^-, over various mechanical and microwave occupations. To reduce n_m to values approaching 1, we increase the cooling tone power up to $n_p^{\text{cool}} = 4 \times 10^5$. For sideband characterization, the probe tone powers are set to $n_p^- = n_p^+ = 10^5$ and the probe sideband spectra are analyzed using the conversion factors described above. The imbalance between n_m^+ and n_m^- is clearly evident in the noise spectra (Fig.3.5(b)).

As further demonstration of the asymmetry with respect to n_{eff}, we plot n_m^+/n_m^- as a function of n_m^- in Fig. 3.5(c). Each curve corresponds to one setting of injected microwave noise. The data shows excellent agreement to the expected ratio, $n_m^+/n_m^- = 1+(2n_{\text{eff}}+1)/n_m^-$. This relationship highlights the combined effect of quantum and classical noise in Eq. (3.35). By fitting each curve to a two parameter model, $a + b/n_m^-$, we find an average constant offset $a = 0.99 \pm 0.02$ for all curves, accurately matching the model and confirming our calibration techniques. Fitting for b, the data indicates n_{eff} spanning 0.71 to 4.5 with uncertainty all within ± 0.09 quanta.

To quantify the contributions due to quantum fluctuations and classical cavity noise, we fix the cooling tone power at $n_p^{\text{cool}} = 4 \times 10^5$ ($\gamma_M = 2\pi \times 360$ Hz) and measure the imbalance $n_m^+ - n_m^-$ as we sweep n_{eff}. At each level, we measure the average noise power density, η, over a 250 Hz window centered at ω_c and away from any motional sideband. Over this range, η

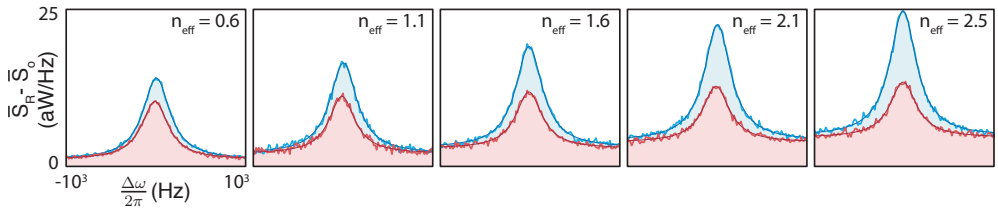

Figure 3.4: Sideband imbalance. Microwave spectrum centered about the up-converted (red) and down-converted (blue) sidebands and with the noise floor of the measurement chain subtracted off. As the classical noise in the cavity is increased from $n_{\text{eff}} = 0.6$ to 2.5, the noise floor increases, the average sideband occupation increases, and the sideband imbalance grows.

contains two contributions: the noise radiating out of the microwave resonator, proportional to n_{eff}, and the detector noise floor, set by the noise temperature of the cryogenic amplifier ($T_N \approx 3.6$K). We directly measure the detector noise floor by switching from the device to an impedance-matched bypass connection and measure the noise power density, η_0, over the same window with matching detected tone powers.

In Fig. 3.5(d), we plot the sideband imbalance against the noise floor increase, $\Delta\eta = \eta - \eta_0$, which is expected to follow: $n_m^+ - n_m^- = 2n_{\text{eff}} + 1 = 4\lambda \cdot \Delta\eta + 1$, where λ is the conversion factor for $\Delta\eta$ in units of cavity quanta, n_c^{th}. The detected noise spectrum at each noise level measured relative to the floor is shown in Fig. 3.4. The data clearly follows a linear trend with a slope of $\lambda = (2.7 \pm 0.1) \times 10^{-1}$ (aW/Hz)$^{-1}$. More importantly, we observe an offset of 1.2 ± 0.2, in excellent agreement with the expected quantum imbalance of "+1" from the quantum fluctuations of the microwave field.

As an additional check, we also consider the sideband average, $(n_m^- + n_m^+)/2$, as a function of $\Delta\eta$. Averaging the up and down-converted Lorentzian components of Eq. (3.35), we see that the resulting occupation, $n_m + \frac{\beta}{2}$, does depend on n_{eff} due to the coupling between the mechanical and microwave modes, $n_m = \frac{\gamma_m}{\gamma_{\text{tot}}} n_m^{th} + \frac{\gamma_{\text{op}}}{\gamma_{\text{tot}}}(2n_c^{th} + \alpha) + \frac{\gamma_{\text{op}}^{\text{cool}}}{\gamma_{\text{tot}}} n_c^{th}$, where γ_{op} ($\gamma_{\text{op}}^{\text{cool}}$) is the optical coupling rate for the individual probe (cooling) tones. Accounting for this so-called back-action heating of the mechanical mode [42, 45], we recover $\lambda = (2.5 \pm 0.2) \times 10^{-1}$ (aW/Hz)$^{-1}$, consistent with the imbalance results above.

Notably, the average sideband occupation does contain contributions from mechanical zero-point fluctuations. Future experiments could infer the mechanical quantum contribution

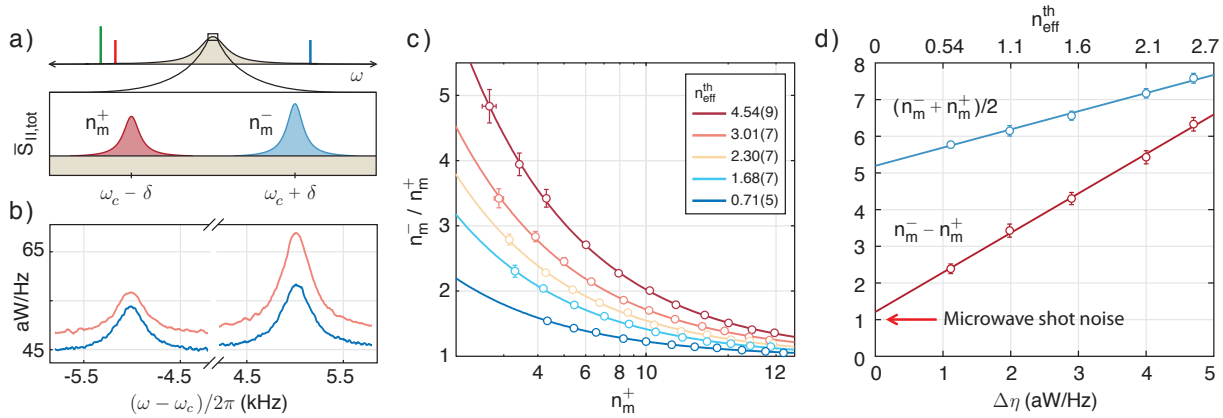

Figure 3.5: Sideband asymmetry. **a.** Pump scheme. Three tones are placed about the microwave resonance. Two probe tones generate up-converted (red) and down-converted (blue) sidebands. An additional tone (purple) cools the mechanical mode. **b.** Sideband spectra. $\bar{S}_R[\omega]$ measured at $n_{\text{eff}} = 0.60$ (blue) and 2.5 (orange) with $n_m = 4.7 \pm 0.1$. **c.** Sideband asymmetry. The ratio n_m^+/n_m^- vs. n_m^- is plotted for increasing noise injection. **d.** Sideband imbalance (blue) and sideband average (purple) vs. the measured noise increase, $\Delta\eta$. Sideband imbalance, $n_m^+ - n_m^-$, and average, $(n_m^+ + n_m^-)/2$, exhibit a linear trend with $\Delta\eta$. The imbalance at $\Delta\eta = 0$ is the quantum imbalance due to the squashing of fluctuations of the microwave field.

of $\frac{\beta}{2}$ with a method to independently calibrate n_m to high accuracy, for example, with a passively cooled high frequency mechanical mode thermalized to a primary low temperature thermometer.

3.3.3 Output port occupation

We estimate the occupation factor of the output port, n_r^{th}, by measuring the microwave noise spectrum absent any microwave pumping. In this setup, we assume that n_c^{th} is solely due to noise radiating into the device from the the isolated port of a cryogenic circulator, so that $n_c^{th} = n_r^{th}\kappa_R/\kappa$. This noise source generates a dip in the broadband noise floor,

$$\bar{S}_R[\omega] = \frac{1}{\lambda}\left[\frac{\kappa^2}{\kappa^2 + 4(\omega - \omega_c)^2}\left(\frac{\kappa_R}{\kappa} - 1\right) n_r^{th} + \left(\frac{\kappa}{4\kappa_R}\right)\left(\alpha_R + 2n_r^{th}\right)\right]. \tag{3.45}$$

Taking $\frac{\kappa_R}{\kappa}$ from independent calibration measurements and λ from the sideband imbalance measurements, we fit the observed Lorentzian to find $n_r^{th} = (3.4 \pm 0.3) \times 10^{-1}$. A typical noise floor spectrum is shown in Fig. 3.6.

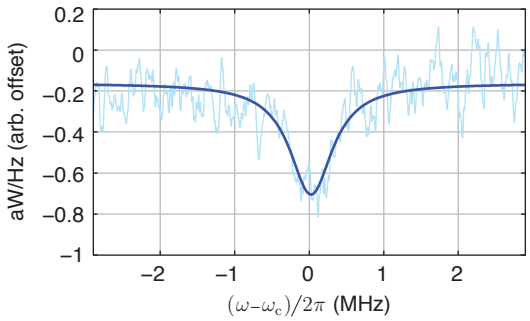

Figure 3.6: n_r^{th} noise spectrum. Example spectrum of microwave noise taken at zero pumping (light blue) with Lorentzian fit (dark blue).

3.3.4 Noise floor calibration

The increase in the device noise floor at cavity resonance is measured relative to the noise floor of an impedance matched through connection with matching amplifier conditions. With the device switched in place, the broadband microwave noise floor is

$$\bar{S}_o[\omega] = \frac{\kappa}{\omega^2 + (\kappa/2)^2}\left(n_c^{th} - n_r^{th}\right) + n_r^{th} + \alpha/2. \tag{3.46}$$

Since this noise floor dip is not present when switching in the impedance-matched through, the observed noise floor increase has a small correction that is proportional to n_{eff} and n_r^{th},

$$\Delta\eta = \frac{1}{2\lambda}\left[n_{\text{eff}} - \left(\frac{2\kappa_R - \kappa}{2\kappa_R}\right) n_r^{th}\right], \tag{3.47}$$

where $n_{\text{eff}} = 2n_c^{th} - n_r^{th}$ as above, and where λ is the conversion factor for $\Delta\eta$ in units of n_c^{th}.

To see how this behavior affects our measurements, we consider the sideband powers in the presence of classical noise n_c^{th}, n_r^{th}. Integrating the noise power under the transduced sidebands of Eq. (3.35), we find that

$$n_m^+ - n_m^- = 4\lambda\Delta\eta + \left(\frac{2\kappa_R - \kappa}{\kappa_R}\right) n_r^{th} + 1, \tag{3.48}$$

and

$$\frac{n_m^+ + n_m^-}{2} = \left(\frac{2\gamma_{\rm op} + \gamma_{\rm op}^{\rm cool}}{\gamma_M}\right)\left[\lambda\Delta\eta + \left(\frac{4\kappa_R - \kappa}{4\kappa_R}\right) n_r^{th}\right] + \frac{\gamma_m}{\gamma_M} n_m^{th} + \frac{\gamma_{\rm op}}{\gamma_M} + \frac{1}{2}, \tag{3.49}$$

where we follow the notation of Eq. (3.43) and have set $\alpha = \beta = 1$, $\gamma_{\rm op}^+ = \gamma_{\rm op}^- = \gamma_{\rm op}$.

The n_r^{th} contribution does not affect the slope of either data set. For sideband imbalance and average measurements, we expect linear dependence on $\Delta\eta$ with slope proportional to λ. The n_r^{th} factor does, however, add fixed offsets to both data sets. For the sideband difference, the contribution is suppressed relative to the quantum offset of "+1". With the experimental parameters $n_r^{th} = 0.34 \pm 0.03$, $\kappa = 2\pi \times (860 \pm 10)$ kHz, and $\kappa_R = 2\pi \times (450 \pm 30)$ kHz, we estimate an offset correction of $\left(\frac{2\kappa_R - \kappa}{\kappa_R}\right) n_r^{th} \approx (3 \pm 4) \times 10^{-2}$, well within the measurement uncertainty for sideband imbalance. This is not the case for the sideband average, where we expect a correction to the offset that is significant when compared to the mechanical quantum contribution of "+1/2".

3.3.5 Conclusion

In summary, we report the quantum imbalance between the up and down-converted motional sideband powers in a cavity electro-mechanical system measured with a symmetric, linear detector. We show that for linear detection of the microwave field, the imbalance arises from the correlations between the mechanical motion and the quantum fluctuations of the microwave detection field. For normal-ordered detection of the microwave field, however, the imbalance arises directly from the quantum fluctuations of the mechanics. By further assuming that the output microwave field satisfies the canonical commutator, which also determines the quantum fluctuations of the mechanical mode, the measurement can be interpreted as performing either symmetric or normal-ordered detection regardless of the type of detector utilized. In both scenarios, the imbalance in motional sidebands is a fundamental quantity originating from the Heisenberg's uncertainty relations and provides a quantum calibrated thermometer for mesoscopic mechanical systems.

Recently, four other groups have measured the motional sideband asymmetry in micron-scale opto- and electro-mechanical systems with both linear [52, 53] and nonlinear [46, 47] detectors, akin to the photon-counting techniques described here. Whatever the interpretation choice of the reader, quantum motion in a macroscopic mechanical resonator has now been demonstrated unambiguously.

Chapter 4

Back-action evasion detection

In the previous section, we explored the behavior for detuned two-tone probing of an electromechanical system. Detuning the sidebands was crucial to simultaneously probe the up- and down-converted motional sidebands without introducing direct correlations between the two drive tones. Though the probes indirectly interact via the dressed the mechanical mode, either by modifying the occupation factor or mechanical susceptibility, there are no back-action imprecision correlations between separate sidebands. What happens when this is no longer the case?

Let us first consider a pair of balanced red- and blue-detuned drive tones ($G_- = G_+ = G$) that are arranged so that the up- and down-converted motional sidebands perfectly overlap (Fig. 4.1). In this configuration, the cavity field becomes

$$\alpha(t) = \sum_{\pm} \alpha_{\pm} e^{-i(\omega_{\pm} t + \phi_{\pm})}, \tag{4.1}$$

$$= \alpha_{\pm} \cos(\omega_m t) e^{-i\omega_c t}, \tag{4.2}$$

with balanced drive amplitudes, $\alpha_{\pm} = \alpha_+ = \alpha_-$. At this point, we ignore the drive phases and set $\phi_{\pm} = 0$ – refer to Sec. 4.1.3 for further discussion of the role of $\phi_{\pm}$.

The cavity field now consists of a fast oscillating carrier tone at ω_c modulated at the mechanical resonance ω_m. Since cavity field drastically boosts the coupling between the cavity and mechanics, the interaction strength will be modulated in time at the mechanical

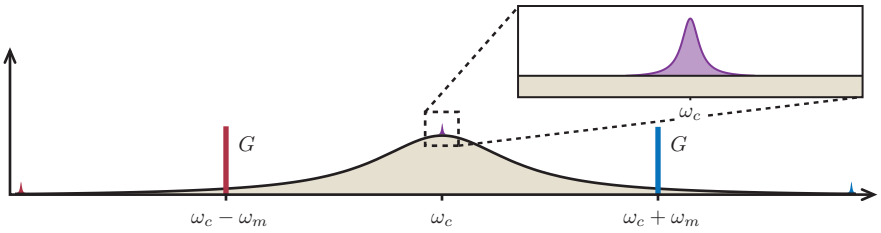

Figure 4.1: BAE pump configuration. In a back-action evading (BAE) scheme, two drive tones are detuned about the microwave cavity (black line) at frequencies $\omega_c \pm \omega_m$ and have balanced amplitudes with associated optomechanical couplings G. The up- and down-converted sidebands are converted into the center of the cavity and are perfectly overlapped (purple area). Backaction forces generated via cavity noise (beige area) mixing exhibit correlations resulting from the red-detuned drive (red bar) and blue-detuned drive (blue bar) mixing with the same region of cavity noise near ω_c. Though suppressed by the cavity DOS, sidebands converted outside the cavity (small red and blue peaks located $\omega_c \pm 2\omega_m$) do not exhibit noise floor correlations and hence will generate quadrature-independent heating.

resonance frequency, and hence the cavity detector will be sensitive only to motion that is in-phase with the modulation signal while out-of-phase motion will average to zero over many mechanical periods. To show that this is indeed the case, we can analyze this drive scheme within the input-output framework.

4.0.1 Interaction Hamiltonian

From these equations, we can now consider the linearized interaction Hamiltonian

$$\hat{\mathcal{H}} = \hbar g_0 [\alpha(t)\hat{d}^\dagger + \alpha(t)^* \hat{d}](\hat{b}e^{-i\omega_m t} + \hat{b}^\dagger e^{i\omega_m t}). \tag{4.3}$$

Substituting in the cavity field $\alpha(t)$, we separate the Hamiltonian into constant DC terms and counter-rotating terms, $\hat{\mathcal{H}} = \hat{\mathcal{H}}_{\text{lin}} + \hat{\mathcal{H}}_{\text{CR}}$,

$$\hat{\mathcal{H}}_{\text{lin}} = G(\hat{d} + \hat{d}^\dagger)(\hat{b} + \hat{b}^\dagger), \tag{4.4}$$

$$\hat{\mathcal{H}}_{\text{CR}} = G(\hat{d} + \hat{d}^\dagger)[(\hat{b} + \hat{b}^\dagger)\cos(2\omega_m t) - i(\hat{b} - \hat{b}^\dagger)\sin(2\omega_m t)]. \tag{4.5}$$

with $G = g_0\alpha_\pm$ and $\hat{d}$ ($\hat{b}$) is the annihilation operator for the microwave (mechanical) mode defined in the interaction picture. Assuming sufficient sideband resolution, the counter-rotating effects are suppressed by the cavity susceptibility and thus $\hat{\mathcal{H}}_{\text{CR}}$ will be initially

ignored in the following analysis.

The operator Langevin equations directly follow from the transformed Hamiltonian as

$$\chi_c^{-1}(\omega)\,\hat{d}[\omega] = -\sqrt{\kappa}\hat{d}_{\rm in}[\omega] - iG_{\pm}(\hat{b}[\omega] + \hat{b}^{\dagger}[\omega]), \tag{4.6}$$

$$\chi_m^{-1}(\omega)\,\hat{b}[\omega] = -\sqrt{\kappa}\hat{b}_{\rm in}[\omega] - iG_{\pm}(\hat{d}[\omega] + \hat{d}^{\dagger}[\omega]). \tag{4.7}$$

In this rotating frame, the susceptibilities $\chi_m^{-1}(\omega) = -i\omega + \frac{\gamma_m}{2}$ and $\chi_c^{-1}(\omega) = -i\omega + \frac{\kappa}{2}$ are Hermitian invariant, i.e., $\chi_m(\omega) = \chi_m^*(-\omega)$ and $\chi_c(\omega) = \chi_c^*(-\omega)$, so that the above equations transform directly into a closed system of equations between the microwave and mechanical field quadratures $\hat{X}_1 = (\hat{b} + \hat{b}^{\dagger})$ and $\hat{U}_1 = (\hat{d} + \hat{d}^{\dagger})$,

$$\chi_c^{-1}(\omega)\,\hat{U}_1[\omega] = -\sqrt{\kappa}\,\hat{U}_{1,\rm in}[\omega], \tag{4.8}$$

$$\chi_m^{-1}(\omega)\,\hat{X}_1[\omega] = -\sqrt{\gamma_m}\,\hat{X}_{1,\rm in}[\omega], \tag{4.9}$$

with bath inputs $\hat{X}_{1,\rm in} = (\hat{b}_{\rm in}+\hat{b}_{\rm in}^{\dagger})$ and $\hat{U}_{1,\rm in} = (\hat{d}_{\rm in}+\hat{d}_{\rm in}^{\dagger})$. It appears that the probe tones have no effect on this specific pair of oscillator quadratures. If we instead consider the orthogonal quadratures $\hat{X}_2 = -i(\hat{b} - \hat{b}^{\dagger})$ and $\hat{U}_1 = -i(\hat{d} - \hat{d}^{\dagger})$ with bath inputs $\hat{X}_{1,\rm in} = (\hat{b}_{\rm in} + \hat{b}_{\rm in}^{\dagger})$ and $\hat{U}_{1,\rm in} = (\hat{d}_{\rm in} + \hat{d}_{\rm in}^{\dagger})$,

$$\chi_c^{-1}(\omega)\,\hat{U}_2[\omega] = -\sqrt{\kappa}\,\hat{U}_{2,\rm in}[\omega] - 2iG_{\pm}\hat{X}_1[\omega], \tag{4.10}$$

$$\chi_m^{-1}(\omega)\,\hat{X}_2[\omega] = -\sqrt{\gamma_m}\,\hat{X}_{2,\rm in}[\omega] - 2iG_{\pm}\hat{U}_1[\omega], \tag{4.11}$$

with bath inputs $\hat{X}_{2,\rm in} = -i(\hat{b}_{\rm in} - \hat{b}_{\rm in}^{\dagger})$ and $\hat{U}_{2,\rm in} = -i(\hat{d}_{\rm in} - \hat{d}_{\rm in}^{\dagger})$.

The correlations between the backaction forces conspire to direct the measurement-induced backaction noise onto a single mechanical quadrature, i.e., the motional heating is driven entirely by fluctuations in $\hat{U}_1$. Similarly, the mechanical-induced heating of the microwave field (i.e., the motional sideband) is transduced entirely into the conjugate microwave quadrature. That is, $\hat{X}_1$ is transduced entirely onto $\hat{U}_2$ while $\hat{X}_2$ is not sensed. Thus, there is no time-dependent feedback mechanism to drive dynamical backaction effects like

damping or amplification.

4.0.2 Quadrature definitions

In the previous section, we briefly introduced the harmonic oscillator quadrature fields as quantum variables that naturally arise from this balanced and overlapped drive scheme. Now, we will now discuss the motivation and significance of the harmonic oscillator quadrature fields.

In general, a one-dimensional oscillator is defined via the dynamics of two conjugate variables and can thus be instantaneously defined classically in a two-dimensional phase space. Motivated by the form of the electromechanical interaction, we shall consider the quadrature amplitudes that are defined in the basis of the cosine (in-phase) and sine (out-of-phase) components of the oscillating signal. Thus, we can explicitly separate the position in to the quadrature components [1],

$$\hat{x} = x_{\mathrm{zp}}(\hat{c} + \hat{c}^\dagger) = \hat{X}_1 \cos(\omega_m t) + \hat{X}_2 \sin(\omega_m t), \tag{4.12}$$

where the mechanical quadrature operators are defined via the ladder operators in the interaction picture ($\hat{c} = \hat{b}e^{-i\omega_m t}$) as

$$\hat{X}_1 = x_{\mathrm{zp}}(\hat{b} + \hat{b}^\dagger), \tag{4.13}$$

$$\hat{X}_2 = -ix_{\mathrm{zp}}(\hat{b} - \hat{b}^\dagger), \tag{4.14}$$

with canonical commutation relations,

$$[\hat{X}_1, \hat{X}_2] = 2ix_{\mathrm{zp}}^2. \tag{4.15}$$

[1] There are two commonly used quadrature definitions: $\hat{X}_1 = x_{\mathrm{zp}}(\hat{d} + \hat{d}^\dagger)$ or $\hat{X}_1 = (\hat{d} + \hat{d}^\dagger)/\sqrt{2}$. Relevant to this discussion, the definitions carry different commutation relations: $[\hat{X}_1, \hat{X}_2] = 2ix_{\mathrm{zp}}^2$ versus $[\hat{X}_1, \hat{X}_2] = i$ and energy prefactors $(\hat{d}^\dagger\hat{d} + \hat{d}\hat{d}^\dagger) = (\hat{X}_1^2 + \hat{X}_2^2)/2x_{\mathrm{zp}}^2$ versus $(\hat{X}_1^2 + \hat{X}_2^2)$. In this work, we use the former definition.

These definitions can be generalized to an arbitrary axes rotation in quadrature space,

$$\hat{X}_\phi = x_{\mathrm{zp}}(e^{i\phi}\hat{b} + e^{-i\phi}\hat{b}^\dagger), \tag{4.16}$$

$$= \hat{X}_1 \cos\phi - \hat{X}_2 \sin\phi. \tag{4.17}$$

For the purpose of the experiment, this phase angle is controlled by the drive tone phases in the lab frame; refer to Sec. 4.1.3 for more information.

In terms of the quadrature definitions, the bare dynamics of the mechanical resonator is prescribed by the system Hamiltonian,

$$\hat{\mathcal{H}}_o = \frac{\hbar\omega_m}{2}(\hat{a}^\dagger\hat{a} + \hat{a}\hat{a}^\dagger), \tag{4.18}$$

$$= \frac{\hbar\omega_m}{4x_{\mathrm{zp}}^2}(\hat{X}_1^2 + \hat{X}_2^2). \tag{4.19}$$

Moving into the Heisenberg picture, the bare quadrature time evolution follows from the quadrature commutator and explicit quadrature time-dependence:

$$\frac{d}{dt}\hat{X}_\phi = \frac{i}{\hbar}[\hat{\mathcal{H}}_o, \hat{X}_\phi] + \frac{\partial}{\partial t}\hat{X}_\phi, \tag{4.20}$$

$$= 0. \tag{4.21}$$

There is no dynamic coupling between the conjugate quadrature variables $\hat{X}_1$ and $\hat{X}_2$ (or any other pair of orthogonal quadratures) and ignoring environmental dissipation, the quadratures are constants of motion. Perturbing one quadrature will not affect the other and hence the quadratures are candidate quantum non-demolition (QND) measurables [54–56].

We have assumed the existence of the microwave field quadratures in the above. Since the microwave cavity is also a harmonic oscillator defined in a two-dimensional phase space for electromagnetic field analogs to position and momentum (i.e., conjugate variables defined between functions of voltage and current), the microwave quadratures are well-defined quantities with near identical operator definitions, commutation relations, and bare dynamical

behavior,

$$\hat{U}_1 = \hat{d} + \hat{d}^\dagger, \tag{4.22}$$

$$\hat{U}_2 = -i(\hat{d} - \hat{d}^\dagger), \tag{4.23}$$

$$[\hat{U}_1, \hat{U}_2] = 2i, \tag{4.24}$$

$$\frac{d}{dt}\hat{U}_\phi|_{\hat{\mathcal{H}}_o} = 0. \tag{4.25}$$

We can reinterpret the interaction Hamiltonian as a linear coupling between the quadratures,

$$\hat{\mathcal{H}}_{\text{lin}} = \hbar G_\pm \hat{X}_1 \hat{U}_1. \tag{4.26}$$

which immediately motivates features of Eqs.(4.8)-(4.11): the mechanical transduction of $\hat{X}_1$ onto $\hat{U}_2$, the optical back-action of $\hat{U}_1$ onto $\hat{X}_2$, and the associated stationary behavior for both $\hat{X}_1$ and $\hat{U}_1$.

The microwave field acts as a $\hat{X}_1$ detector and will induce optical back-action forces on the orthogonal $\hat{X}_2$ that are dynamically uncoupled from the measurement. This is the purpose of setting up balanced, overlapping drive tones – by isolating the back-action forces from the detected parameter, the drive configuration forms a QND measurement of a single mechanical quadrature. In the following, this measurement scheme is referred to as back-action evasion (BAE) detection [35, 57, 58]. This type of measurement is fundamentally different than continuous position measurement where the measurement will increasingly perturb both position and momentum with increasing measurement strength, leading to the so-called standard quantum limit (SQL) for position detection [11]. Over the past decade, position measurements have reached imprecision levels below that at SQL [59,60]. Similarly, the back-action heating driven via quantum fluctuations of the measurement field have been observed in mechanical system via electrons [61] and via photons [10, 62].

4.0.3 Noise spectrum

To support the claims of QND detection, we now calculate the mechanical quadrature spectrum and the output microwave noise spectrum. Starting with the mechanics, the symmetrized quadrature noise spectrum is,

$$\bar{S}_{\hat{X}_\phi}[\omega] = \frac{1}{2}\int dt e^{i\omega t}\langle\{\hat{X}_\phi(t), \hat{X}_\phi(0)\}\rangle \tag{4.27}$$

$$= \frac{1}{2}\int \frac{d\omega'}{2\pi}\langle\{\hat{X}_\phi[\omega'], \hat{X}_\phi[\omega]\}\rangle. \tag{4.28}$$

Substituting in Eqs. (4.8-4.11) along with the quadrature bath correlations

$$\langle\hat{X}_{\phi,\mathrm{in}}[\omega]\hat{X}_{\phi,\mathrm{in}}[\omega']\rangle = x_{\mathrm{zp}}^2(2n_m^{th}+1)\,2\pi\delta(\omega+\omega'), \tag{4.29}$$

$$\langle\hat{U}_{\phi,\mathrm{in}}[\omega]\hat{U}_{\phi,\mathrm{in}}[\omega']\rangle = (2n_c^{th}+1)\,2\pi\delta(\omega+\omega'), \tag{4.30}$$

$$\langle\hat{X}_{\phi,\mathrm{in}}[\omega]\hat{U}_{\phi,\mathrm{in}}[\omega']\rangle = 0, \tag{4.31}$$

yields the quadrature spectrum,

$$\bar{S}_{X_1}[\omega]/x_{\mathrm{zp}}^2 = \frac{\gamma_m}{\omega^2+(\frac{\gamma_m}{2})^2}\left[1+2(n_m^{th}+n_m^{\mathrm{bad}})\right], \tag{4.32}$$

$$\bar{S}_{X_2}[\omega]/x_{\mathrm{zp}}^2 = \frac{\gamma_m}{\omega^2+(\frac{\gamma_m}{2})^2}\left[1+2(n_m^{th}+n_{\mathrm{ba}}+n_m^{\mathrm{bad}})\right]. \tag{4.33}$$

The back-action heating of $\hat{X}_2$ manifests via the occupation factor,

$$n_{\mathrm{ba}} = \frac{2\gamma_{\mathrm{op}}}{\gamma_m}(2n_c^{th}+1), \tag{4.34}$$

where the optical scattering rate is defined as $\gamma_{\mathrm{op}} = 4G^2/\kappa$.

In Eqs.(4.32, 4.33), we have included bad-cavity effects generated by the counter-rotating terms of $\hat{\mathcal{H}}_{CR}$. To first order in drive power, the counter-rotating terms introduce weak back-action forces that are included here in the form of quadrature-insensitive heating given by the occupation factor $n_m^{\mathrm{bad}} = \frac{1}{32}(\frac{\kappa}{\omega_m})^2 n_{\mathrm{ba}}$ [58]. For the parameter regime typically encountered

in our experiments, this heating term is of order unity at the highest measurement strengths and hence plays no significant role for interpreting results.

The output microwave field is connected to the cavity field via standard input-output relation $\hat{d}_{\sigma,\text{out}} = \sqrt{\kappa_\sigma}\hat{d} + \hat{d}_{\sigma,\text{in}}$, and is defined in terms of the field leaving the output port (right) of the device, $\hat{d}_{R,\text{out}}$. Solving for the output spectrum

$$\bar{S}_R[\omega] = \frac{1}{2}\int dt e^{i\omega t}\langle\{\hat{d}_{R,\text{out}}(t), \hat{d}^\dagger_{R,\text{out}}(0)\}\rangle, \tag{4.35}$$

$$= \frac{\kappa_R}{\kappa}\frac{\gamma_{\text{op}}}{x^2_{\text{zp}}}\bar{S}_{\hat{X}_1}[\omega] + \bar{S}_o[\omega]. \tag{4.36}$$

where the noise floor identifies the classical occupation of the microwave baths and the shot noise of the microwave field,

$$\bar{S}_o\left[\omega\right] = \frac{\kappa_R\kappa}{\omega^2 + (\frac{\kappa}{2})^2}\left(n_c^{th} - n_r\right) + n_r + \frac{1}{2}. \tag{4.37}$$

4.0.4 Scattering matrix formalism

As a consistency check, we can rederive the above relations within the scattering framework. With the drive configuration for BAE, the scattering matrix is

$$\boldsymbol{\chi}(\omega) = \begin{bmatrix} -i\omega + \frac{\kappa}{2} & 0 & -iG & -iG \\ 0 & -i\omega + \frac{\kappa}{2} & iG & iG \\ -iG & -iG & -i\omega + \frac{\gamma_m}{2} & 0 \\ iG & iG & 0 & -i\omega + \frac{\gamma_m}{2} \end{bmatrix}^{-1}. \tag{4.38}$$

Solving for the mechanical scattering terms,

$$\begin{aligned} \boldsymbol{\chi}_{31}(\omega) &= \tfrac{4iG}{(\gamma_m - 2i\omega)(\kappa - 2i\omega)}, & \boldsymbol{\chi}_{32}(\omega) &= \tfrac{4iG}{(\gamma_m - 2i\omega)(\kappa - 2i\omega)}. \\ \boldsymbol{\chi}_{33}(\omega) &= \tfrac{2}{\gamma_m - 2i\omega}, & \boldsymbol{\chi}_{34}(\omega) &= 0. \end{aligned} \tag{4.39}$$

The symmetrized quadrature spectra are

$$\bar{S}_{\hat{X}_1}[\omega] = \bar{S}_{xx}[\omega] + \Delta[\omega], \tag{4.40}$$

$$\bar{S}_{\hat{X}_2}[\omega] = \bar{S}_{xx}[\omega] - \Delta[\omega], \tag{4.41}$$

where $\Delta[\omega]$ incorporates the cross terms associated with $\langle \hat{b}[\omega]\hat{b}[\omega']\rangle$ and $\langle \hat{b}^\dagger[\omega]\hat{b}^\dagger[\omega']\rangle$,

$$\Delta[\omega] = 2\,\mathrm{Re}(\boldsymbol{\chi}_{31}[\omega]\boldsymbol{\chi}_{32}[-\omega])\,\kappa(2n_c^{th}+1) \tag{4.42}$$

$$+ 2\,\mathrm{Re}(\boldsymbol{\chi}_{33}[\omega]\boldsymbol{\chi}_{34}[-\omega])\,\gamma_m(2n_m^{th}+1) \tag{4.43}$$

$$= -2\frac{\gamma_{\mathrm{op}}}{\omega^2 + (\frac{\gamma_m}{2})^2}\,\kappa(2n_c^{th}+1). \tag{4.44}$$

Solving for the quadrature spectra yields identical results as Eqs. (4.32), (4.33).

For the microwave spectrum, the relevant scattering terms are

$$\begin{aligned} \boldsymbol{\chi}_{11}(\omega) &= \tfrac{2}{\kappa-2i\omega}, & \boldsymbol{\chi}_{12}(\omega) &= 0, \\ \boldsymbol{\chi}_{13}(\omega) &= \tfrac{4iG}{(\gamma_m-2i\omega)(\kappa-2i\omega)}, & \boldsymbol{\chi}_{14}(\omega) &= \tfrac{4iG}{(\gamma_m-2i\omega)(\kappa-2i\omega)}, \end{aligned} \tag{4.45}$$

which reproduce the output BAE spectrum of Eq. (4.36).

4.1 Back-action and imprecision definitions

4.1.1 BAE configuration

In terms of spectral density, that we directly accesses via FFT analysis of the full measurement chain, S_I, we must include the power gain, $\mathcal{G}^2[\omega]$, and uncorrelated noise floor, $\bar{S}_{\mathrm{add}}[\omega]$, of the amplifier chain,

$$S_I[\omega] = \mathcal{G}^2\left(\bar{S}_R[\omega] + \bar{S}_{\mathrm{add}}[\omega]\right). \tag{4.46}$$

The final expression references the measured spectrum in terms of the components of

the mechanical quadrature spectrum. By splitting up the spectrum into three main components, it is now easy to identify the contributions from the intrinsic thermal motion, n_m^{th}, measurement back-action, n_{ba}, and detector imprecision, n_{imp}.

Regarding the amplifier noise floor, we initially assume the amplifier gain and noise floor are sufficiently flat about the cavity resonance frequency over a bandwidth on the order of κ, $\mathcal{G}^2[\omega] \rightarrow \mathcal{G}^2$ and $\bar{S}_{\mathrm{add}}[\omega] = \hbar\omega_c n_{\mathrm{add}}[\omega]$.

Per the typical definition of measurement imprecision [6, 11], n_{imp} is defined as the measurement-induced mechanical occupation evaluated at mechanical resonance. Here, however, the measurement system is a single quadrature detector opposed to a position detector and hence we only consider the imprecision noise for the sensed parameter $\hat{X}_1$:

$$S_I[0] = \gamma_{\mathrm{op}}^{\pm} \frac{\kappa_R}{\kappa} \frac{8}{\gamma_m} \left[\left(n_m^{th} + \frac{1}{2} \right) + n_{\mathrm{imp}} \right], \tag{4.47}$$

where,

$$n_{\mathrm{imp}} = \frac{\kappa}{\kappa_R} \frac{\gamma_m}{8\gamma_{\mathrm{op}}^{\pm}} \left(\bar{S}_o[0] + \bar{S}_{\mathrm{add}}[0] \right). \tag{4.48}$$

For ideal BAE, there is no back-action heating of $\hat{X}_1$ and the single quadrature detector noise product is zero. This does not break the quantum bounds on detector noise products since the BAE measurement manifests through back-action imprecision correlations.

In practice, there is drive power dependent heating of the mechanics induced either through resistive ohmic heating or other mechanical nonlinearities [42,63]. To conservatively model any drive-dependent heating, we define the amount of motional backaction heating as the net increase in mechanical occupation induced from the measurement drive tones regardless of the microscopic origin. As such, the measured backaction, n_{ba} , is calculated in this work as the net increase between the dressed mechanics in the presence of BAE driving and the bare mechanics, which here refers to the system without the BAE tones (but still including the cooling tones).

For a quantum limited phase-insensitive amplifier, $\bar{S}_{\mathrm{add}} = \frac{1}{2}$ and the minimum imprecision level for a zero-temperature cavity is equal to one quanta. Referenced to the mechanical

spectrum, however, the imprecision can be made arbitrarily small by increasing the drive powers ($\gamma_{\rm op}$). Though this would seem to ensure that sufficiently high powers can, in principle, be applied to suppress imprecision below the $x_{\rm zp}$ level, there are various cavity and mechanical nonlinearities that pose limits to the applied power. Historically, such a measurement has proven difficult due to the effect of relatively small optomechanical couplings in combination with mechanical Kerr nonlinearities that have combined in the past to limit the imprecision above zero-point level [15, 17, 19].

4.1.2 DTT configuration

We have now shown that ideal BAE detection generates back-action forces on the mechanics that are entirely routed to the un-detected mechanical quadrature $\hat{X}_2$. To confirm that this is indeed the case, we can directly observe the back-action heating generated by the BAE tones in numerous different ways. As a first step, we compare the BAE detection scheme to a $\langle \hat{x}^2 \rangle$ measurement with identical drive strengths. We designate this position measurement scheme as a "detuned two-tone" (DTT) identical to the pump configuration summarized for sideband asymmetry measurements in Fig. 3.1.

Detuned two-tone pump configuration consists of two balanced drive tones ($\gamma_{\rm op}^{+} = \gamma_{\rm op}^{-}$) placed symmetrically about the cavity at frequencies $\omega_c \pm (\omega_m + \delta)$. Compared to the total mechanical linewidth, the transduced sidebands are sufficiently separated in frequency space ($\delta \gg \gamma_m$) to prohibit direct drive interference.

Using the analysis developed for sideband asymmetry measurements of the previous section, we now further restrict the drive configuration to balanced red and blue drives, such that $G_{-} = G_{+} = G$ and by extension $\gamma_{\rm op}^{+} = \gamma_{\rm op}^{-} = \gamma_{\rm op} = \frac{4G^2}{\kappa}$. The DTT output microwave spectrum exhibits electromechanical noise contributions from the intrinsic mechanical motion, the measurement imprecision, and back-action imprecision correlations in the form of noise squashing and anti-squashing.

We can reinterpret the detuned two tone (DTT) configuration as a measurement of position ($\propto \langle \hat{x}^2 \rangle$) by averaging the up and down-converted sidebands in Eq. (3.35) to remove

the effects of cavity noise correlations in the form of squashing and anti-squashing,

$$\frac{1}{2}\sum_{\pm}\bar{S}_R[\omega\pm\delta]=\bar{S}_o[\omega]+\frac{\kappa_R}{\kappa}\frac{\gamma_m\gamma_{\rm op}^{\pm}}{\omega^2+(\frac{\gamma_m}{2})^2}\,(n_m+1/2), \tag{4.49}$$

where we have assumed the noise floor $\bar{S}_o$ is flat over the designated frequency range. The mechanical occupation now exhibits optically induced quadrature-independent back-action heating, $n_m=n_m^{th}+\frac{\gamma_{\rm op}^{\pm}}{\gamma_m}(2n_c^{th}+1)$.

Following the imprecision formalism from above, the detected output noise spectrum is

$$S_I^{\rm DTT}[\omega]=\mathcal{G}^2\left(\frac{1}{2}\sum_{\pm}\bar{S}_R[\omega\pm\delta]+\bar{S}_{\rm add}[\omega]\right),$$

with DTT back-action factor as

$$n_{\rm ba}^{\rm DTT}=\frac{\gamma_{\rm op}^{\pm}}{\gamma_m}(2n_c^{th}+1), \tag{4.50}$$

$$=n_{\rm ba}^{\rm BAE}/2, \tag{4.51}$$

and imprecision factor,

$$n_{\rm imp}^{\rm DTT}=\frac{\kappa}{\kappa_R}\frac{\gamma_m}{4\gamma_{\rm op}^{\pm}}\left(\bar{S}_o[0]+\bar{S}_{\rm add}[0]\right) \tag{4.52}$$

$$=2n_{\rm imp}^{\rm BAE}. \tag{4.53}$$

Note that the back-action and imprecision noise in DTT differs from the BAE configuration by a factor of two. The scaling between BAE and DTT back-action heating factors implies that the total back-action heating for position is equal in both BAE and DTT pump configurations. The different scaling arises because the heating is spread equally between the quadratures in DTT configuration but is entirely concentrated to a single quadrature in BAE configuration. The imprecision also differs by a factor of two due to the distribution of the sidebands in frequency space. Spacing out the sidebands effectively adds twice the amount of imprecision noise compared to the overlapped sidebands in BAE configuration.

4.1.3 Microwave drive phase dependence

So far, we have completely ignored the phases of the microwave drive tones. Now we can explicitly include the phase information and explore how it may affect the BAE measurement. Modeling the cavity field generated via two balanced drives ($\alpha_- = \alpha_+$) symmetrically detuned from ω_c by $\pm\omega_m$,

$$\alpha(t) = \sum_{\pm} \alpha_{\pm} \cos(\omega_{\pm} t + \phi_{\pm}), \tag{4.54}$$

$$= \alpha_{\pm} \left[e^{-i(\omega_m t + \Delta)} + e^{i(\omega_m t + \Delta)} \right] e^{-i(\omega_c t + \bar{\phi})} + \text{c.c.}, \tag{4.55}$$

where the above frequencies and phases are defined via the drive parameters,

$$\begin{aligned} \tfrac{1}{2}(\omega_+ + \omega_-) &= \omega_c, \qquad & \tfrac{1}{2}(\omega_+ - \omega_-) &= \omega_m, \\ \tfrac{1}{2}(\phi_+ + \phi_-) &= \bar{\phi}, \qquad & \tfrac{1}{2}(\phi_+ - \phi_-) &= \Delta. \end{aligned} \tag{4.56}$$

In terms of the incident microwave power and phases that are available for experimental control,

$$\alpha_{\pm} = \sqrt{\frac{\kappa_L}{\omega_m^2 + (\kappa/2)^2} P_{\text{in}}^{\pm}}, \tag{4.57}$$

$$\bar{\phi} = \bar{\phi}_{\text{in}}, \tag{4.58}$$

$$\Delta = \arctan\left(\frac{\kappa}{2\omega_m}\right) + \Delta_{\text{in}}. \tag{4.59}$$

Plugging this drive field into the Langevin equations for the mechanical and microwave fields in a rotating, displaced frame ($\hat{a} \to [\alpha(t) + \hat{d}]e^{-i\omega_c t}$ and $\hat{c} \to \hat{b}e^{-i\omega_m t}$) with enhanced optomechanical couplings $G_{\pm} = g_0 \alpha_{\pm}$ and rotating wave approximation, the field quadratures follow

$$\chi_m^{-1}(\omega)\, \hat{X}_{\phi}[\omega] = -\sqrt{\gamma_m}\, \hat{X}_{\phi,\text{in}}[\omega] - iG_{\pm} \hat{U}_{\phi}[\omega] \left(e^{-i(\phi - \Delta)} - e^{-i(\phi - \Delta)} \right) x_{\text{zp}},$$
$$\chi_c^{-1}(\omega)\, \hat{U}_{\phi}[\omega] = -\sqrt{\kappa}\, \hat{U}_{\phi,\text{in}}[\omega] - iG_{\pm} \hat{X}_{\Delta}[\omega] \left(e^{-i(\phi - \bar{\phi})} - e^{-i(\phi - \bar{\phi})} \right) / x_{\text{zp}}.$$

As one would expect for power detection, the output spectrum derived with drive phase information has no absolute phase dependence,

$$\bar{S}_R[\omega] = \bar{S}_o + \frac{\kappa_R}{\kappa}\frac{\gamma_{\rm op}^{\pm}}{x_{\rm zp}^2} S_{\hat{X}_\Delta}[\omega].$$

The phase difference Δ determines the mechanical quadrature axes in the lab frame. The absolute phase $\bar{\phi}$ determines the lab frame axis of the microwave quadrature that carries the mechanical quadrature signal. Our measurement techniques are unable to differentiate between the microwave quadratures (this could be addressed with an IQ-mixer for quadrature detection) so we only concern ourselves with the relative phase Δ.

4.2 BAE results

Having analyzed the BAE measurement within an input-output framework and confirmed its QND behavior, we will now discuss our experimental results in an electromechanical device. For this experiment, we implement BAE with the same device and measurement circuit utilized in sideband asymmetry measurements. To reiterate, we study a lumped-element microwave LC resonator (denoted in this work as "cavity") in the high-Q regime with resonance frequency $\omega_c = 2\pi \times 5.4$ GHz and total linewidth $\kappa = 2\pi \times 860$ kHz. From independent tests at 300mK, the output port scattering rate is $\kappa_R = 2\pi \times 450$ kHz. The capacitor top gate that supports out-of-plane acoustic modes, of which we study the fundamental mode with resonance $\omega_m = 2\pi \times 4.0$ MHz and intrinsic dissipation $\gamma_m = 2\pi \times 10$ Hz at 20mK. Motion of the top gate modulates the capacitance and shifts ω_c by $2\pi \times 16$ Hz ($= g_0$) per $x_{\rm zp}$, where $x_{\rm zp} \simeq 1.8$ fm.

4.2.1 Calibrations

To calibrate the measurement circuit, we perform linewidth-broadening and thermo-mechanical noise calibrations for a single red-detuned drive. A microwave pump is placed at $\omega_c - \omega_m$ and and the complex cavity transmission is measured via sweeping heterodyne detection. As the

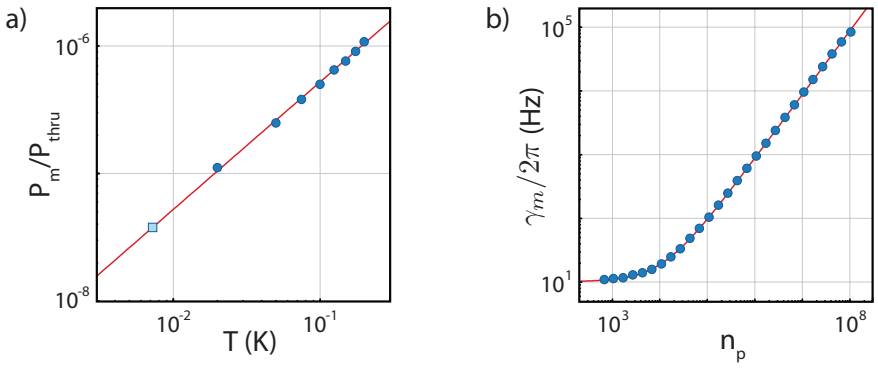

Figure 4.2: System calibrations. **a.** Calibration of the up-converted motional sideband against calibrated thermal motion (blue circles). At the base temperature of the fridge (and outside the range of resistance thermometry) the mechanics thermalizes to an extracted temperature of 7.2 ± 0.2mK (light blue square) consistent with the expected base temperature of the cryostat. **b.** Backaction damping and pump photon calibration. As the system is pumped with elevated drive power, the total linewidth of the up-converted sideband (blue circles) is monitored via scanning homodyne detection. Fit to back-action damping theory (red line) result in a calibration for pump photons n_p versus detected output power.

pump power is increased, we monitor the detected output pump power, P_-, as well as the back-action damping $\gamma_{\rm op}$ from linewidth broadening of the transduced mechanical sideband. Next, we decrease the pump power to a sufficiently low level ($\gamma_{\rm op} \simeq \gamma_m/100$) and then plot the integrated noise power in the up-converted sideband, P_m, as we sweep the calibrated temperature of the cryostat between 20mK to 200mK. The two measurements are cast in linear form and yield the calibration factors a_- and b_-,

$$\gamma_{\rm op} = \frac{4G^2}{\kappa} = a_- \left(\frac{4}{\kappa}\right) P_-, \tag{4.60}$$

$$\frac{P_m}{P_-} = \frac{1}{b_-}\frac{k_B T}{\hbar\omega_m}, \tag{4.61}$$

where κ is observed to be constant over the relevant pump configurations so that power-dependent linewidth shifts are ignored. Converting the calibration factors to readily accessible formats for measurement, we find

$$\frac{n_p}{P_-} = \left(\frac{a_-}{g_0^2}\right) = (2.25 \pm 0.7) \times 10^{11}\,\mathrm{W}^{-1}, \tag{4.62}$$

$$\frac{n_m}{(P_m/P_-)} = b_- = (9.92 \pm 0.16) \times 10^8. \tag{4.63}$$

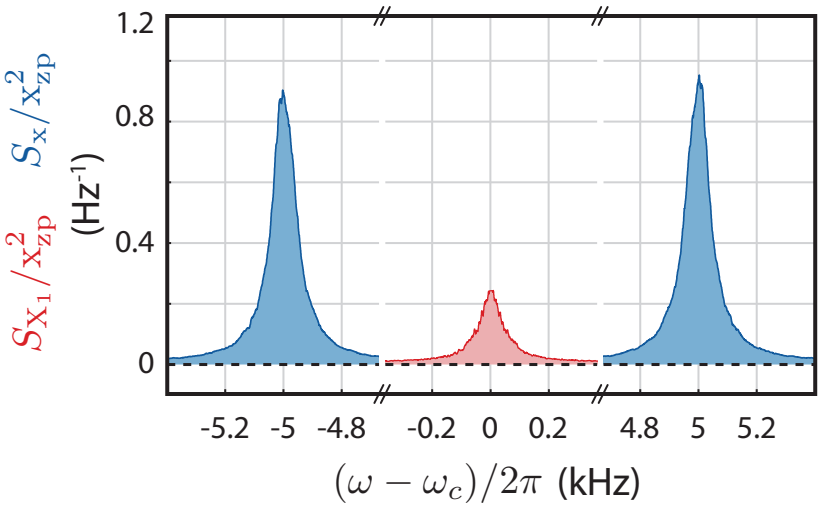

Figure 4.3: BAE and DTT noise spectrum. Measured noise spectrum converted to units of motional zero-point fluctuations. The BAE spectrum (red area) clearly shows reduced noise area compared to the sidebands generated in DTT pumping (blue area).

Though BAE and DTT experiments incorporate both red and blue-detuned drives, accurately balancing the drive powers provide full system analysis entirely via the red-detuned drive calibrations. Refer to Fig. 4.2 for calibration measurement results.

4.2.2 Measurement

For the actual experiment, a third cooling tone is added to suppress mechanical frequency jitter on the scale of the intrinsic linewidth. To do this, we apply a cooling tone at $n_p^{\text{cool}} \sim 10^5$ detuned from cavity center by δ_c (refer to Fig. 4.5). Sufficiently large detuning ($\delta_c \gg \gamma_{\text{tot}}$) ensures that the cooling tone dresses the mechanics – it broadens the mechanical damping and cools the mechanical occupation from the intrinsic bath the lower occupation – without otherwise affecting behavior of the BAE detection scheme.

For the measurement, we aim to perform three tasks: measure the intrinsic mechanical motion dressed via the cooling tone, balance and measure DTT noise spectrum, and measure the BAE spectrum. We accomplish this with the following protocol:

1. First, measure the cavity transmission with all tones set to estimated powers and frequencies. Fit the transmission spectrum to extract system frequencies and detunings.

Reconfigure the pumps to ensure $\omega_{\rm cool} = \omega_c - (\omega_m + \delta_c)$ with $\delta_c = 2\pi \times 35$ kHz and $\omega_\pm = \omega_c \pm (\omega_m + \delta)$ with $\delta = 2\pi \times 5$ kHz.

2. Turn off BAE tones, check cooling tone fedthru power and take cooling spectra. Extract γ_m and $n_m^{\rm cool}$. Treat these as the initial, unperturbed system parameters γ_m^o and n_m^o,

$$n_{\rm cool} = b_- \left(\frac{A_{\rm cool}}{P_{\rm cool}} \right), \tag{4.64}$$

$$= n_m^o. \tag{4.65}$$

3. Turn on DTT tones, take noise spectrum, and balance to γ_m. Power balancing is achieved by matching the linewidth of the dressed mechanical system to the intrinsic linewidth γ_m. We assume the intrinsic linewidth does not appreciably change with applied BAE tone which is consistent with mechanical occupation extracted from BAE measurement at lower powers.

4. Measure DTT noise spectra. Fit each sideband to a Lorentzian lineshape then calculate the average integrated sideband power as $A_{\rm DTT} = \frac{1}{2}(A_{\rm red} + A_{\rm blue})$. We then convert the sideband powers to equivalent occupation,

$$n_{\rm DTT} = b_- \left(\frac{A_{\rm DTT}}{P_-} \right), \tag{4.66}$$

$$= n_m^o + n_{\rm ba}^{\rm DTT} + \frac{1}{2}. \tag{4.67}$$

   A typical DTT noise spectrum is presented in Fig. 4.3.

5. Measure the BAE noise spectra. Reconfigure the pumps to overlap the mechanical sidebands. Measure the fed through power of each drive, then measure the BAE spectrum. Refer to Fig. 4.3 for a typical BAE spectrum. In comparison to the DTT spectrum, it is clear that the back-action is significantly reduced in BAE configuration. Extract the integrated area under the BAE Lorentzian, $A^{\rm BAE}$. With calibration factors,

convert the integrated power to equivalent quanta,

$$n_{\mathrm{BAE}} = b_- \left(\frac{A_{\mathrm{BAE}}}{2P_-} \right), \tag{4.68}$$

$$= n_m^o + n_{\mathrm{ba}}^{\mathrm{BAE}} + \frac{1}{2}. \tag{4.69}$$

Note that the conversion factor between integrated sideband power and mechanical occupation differs between BAE and DTT configurations by a factor of two. Furthermore, the backaction definition also differs by two between BAE and DTT. To properly account for both these effects, we define the number of pump photons in BAE as twice the number of pump photons in DTT.

6. Extract the back-action and imprecision components of the BAE and DTT occupation factors. Associate any mechanical heating deviation from step (1) as measurement backaction $n_{\mathrm{ba}}^{\mathrm{BAE}}$. For the two pump configurations (σ = BAE, DTT), the backaction can be directly isolated in the above calculations, whereas the imprecision can defined in terms of the detected noise floor, sideband peak height, and equivalent sideband occupation:

$$n_{\mathrm{ba}}^{\sigma} = n_\sigma - n_m^o, \tag{4.70}$$

$$n_{\mathrm{imp}}^{\sigma} = \left(n_\sigma + \frac{1}{2} \right) \left(\frac{\mathrm{background}}{\mathrm{peak}} \right). \tag{4.71}$$

For probe powers spanning $n_p = 10^4 - 10^7$, the detected $n_{\mathrm{ba}}^{\mathrm{BAE}}$, $n_{\mathrm{ba}}^{\mathrm{DTT}}$ for are plotted in Fig. 4.4.

At the highest powers reached in the experiment, we demonstrate BAE detection that avoids total backaction heating by approximately 10dB. More importantly, we observe quadrature heating that is 8.5 ± 0.4 dB below the noise associated with quantum limited back-action heating from the microwave shot noise. Simultaneously, the quadrature imprecision is below the zero-point level, corresponding to $\langle \hat{X}_1^2 \rangle_{\mathrm{imp}} = 0.6 x_{\mathrm{zp}}^2$. Reframing these quantities in terms of the detector spectral densities associated with backaction ($S_{\hat{X}_1,\mathrm{imp}}$) and imprecision

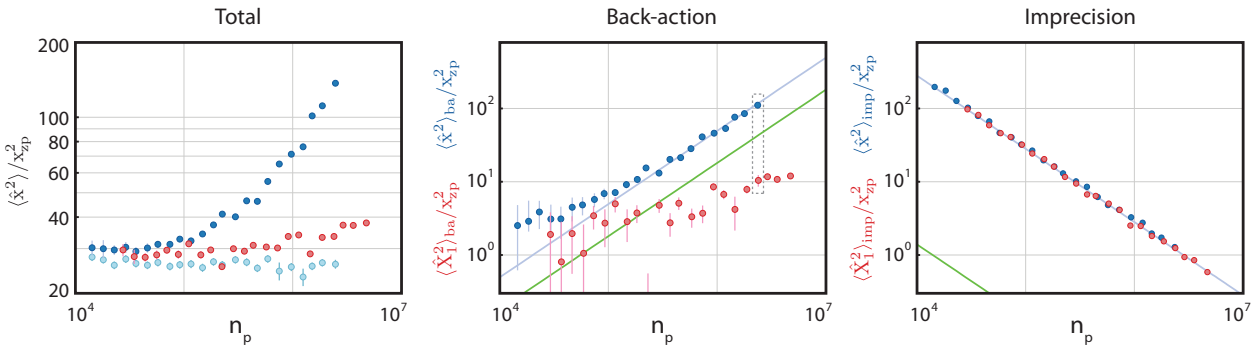

Figure 4.4: BAE and DTT occupations. **a.** Integrated sideband power for DTT (dark blue), BAE (red), and no-pump (light blue) configurations. There is a clear reduction in the total observed noise power between DTT and BAE configurations. In no-pump, the BAE tones are turned off and the cooling tone sideband is monitored to check system drift. **b.** Back-action noise for DTT (blue) and BAE (red) pumping defined as the increase in motional noise relative to the undriven mechanical occupation, i.e., the occupation extracted from no-pump measurements. Even with zero classical noise, the BAE quadrature detection reaches below the level of quantum-limited backaction for position detection (green line). Example spectra at the highest powers (dotted grey box) are featured in Fig. 4.3. **c.** Imprecision noise as a function of pump power. At the highest powers, the BAE imprecision reaches 0.6 x_{zp}^2. A quantum limited amplifier would drastically reduce this level (green line).

($S_{F,ba}$), we reach a detector noise product of $\sqrt{S_{\hat{X}_1,\mathrm{imp}} S_{F,ba}} \simeq 2.5\hbar$ [42] that is lower than other comparable micro- and nano-mechanical devices [11].

4.3 Double BAE

So far, we have used the DTT position measurement as a way to highlight the QND nature of the BAE measurement. Comparing the two measurements, the effective sideband area in BAE is highly suppressed, consistent with backaction avoidance. However, this measurement does not entirely verify or validate that the BAE measurement is acting as intended. To exclude any loopholes, such as miscalibrated pump power or electromechanical couplings (which would effect both BAE and DTT measurements and therefore are not realistic issues) or a mechanical parametric effect, we now consider directly measuring the backaction of one set of BAE tones (denoted below as "pump") with an additional, weaker BAE set ("probe"). Refer to Fig. 4.5 for a schematic of the full pump configuration. In the following, we will first confirm that double BAE works as we suspect and will then present results of the direct measurement of BAE measurement backaction.

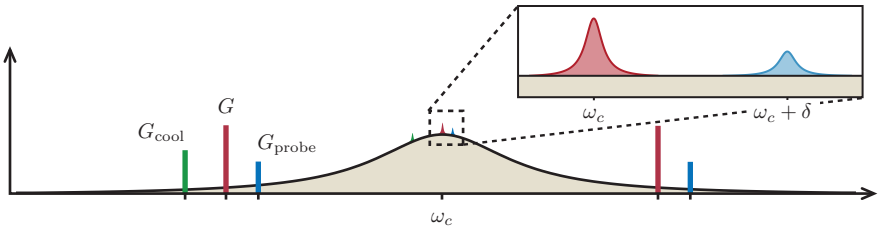

Figure 4.5: Double BAE pump configuration. Five drive tones are placed about the cavity (black line). A pair of BAE pump tones (red bars), each inducing the enhanced optomechanical strength G, are placed at $\omega_c \pm \omega_m$. A weaker set of probe BAE tones (blue bars) are placed at $\omega_c + \delta \pm \omega_m$ with coupling strength G_{probe}. A fifth cooling tone (green bar) with coupling strength G_{cool} is detuned outside of the BAE tones and serves to optically damp the mechanics. Inset: the BAE pump (red area) and probe (blue area) sidebands are sufficiently detuned to avoid overlap. During measurement, both sets of sidebands are monitored as we vary the relative phases between the probe drives. Additionally, we regulate the cavity noise occupation (beige) which resembles a flat noise floor over the relevant measurement bandwidths.

4.3.1 Double BAE

Assuming the pump and probe BAE are sufficiently isolated from each other, each set of BAE tones are sensitive only to the quadrature phase set by their respective drive phases: the pump signal at $\omega \simeq 0$ senses $\phi = 0$, the probe signal at $\omega \simeq \delta$ measures $\phi = \theta$,

$$\chi_c^{-1}(\omega)\hat{d}[\omega] = -\sqrt{\kappa}\hat{d}_{in}[\omega] - iG\hat{X}_1[\omega]/x_{\text{zp}} - iG_{\text{probe}}\hat{X}_\theta[\omega - \delta]/x_{\text{zp}}. \tag{4.72}$$

We immediately find that the microwave field will carry information about the desired quadratures in spectrally-distinct regions of frequency space.

For $\delta \gg \gamma_{\text{tot}}$, the mechanics now incorporates two distinct phase-dependent heating tones with measurement axes rotated by ϕ_2.

$$\begin{aligned}\chi_m^{-1}(\omega)\hat{X}_\phi[\omega] = &-\sqrt{\gamma_m}\hat{X}_{\phi,\text{in}}[\omega] \\ &- ix_{\text{zp}}G\left(e^{i\phi} - e^{-i\phi}\right)\left(\hat{d}_{\text{in}}[\omega] + \hat{d}_{\text{in}}^\dagger[\omega]\right) \\ &- ix_{\text{zp}}G_{\text{probe}}\left(e^{i(\phi-\theta)} - e^{-i(\phi-\theta)}\right)\left(\hat{d}_{\text{in}}[\omega+\delta] + \hat{d}_{\text{in}}^\dagger[\omega-\delta]\right),\end{aligned}$$

where we have ignored cross-terms that scale as $(\frac{\gamma_m}{\kappa}\frac{\delta}{\kappa}n_{\text{ba}})$. Unlike the case of single BAE drive, the mechanical quadratures now exhibit cross-correlations, i.e., $S_{\hat{X}_1\hat{X}_2} \neq 0$. However, we only concern ourselves with the quadrature spectrum for the experimentally accessible

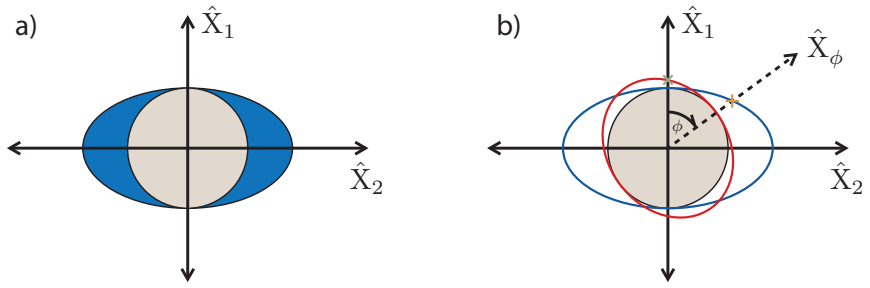

Figure 4.6: Mechanical noise ellipse. **a.** For a single BAE drive, the mechanical noise ellipse (blue) resembles a thermal squeezed state whereby all the back-action noise is added to the undetected quadrature $\hat{X}_2$ of the thermal noise ellipse (beige). With single BAE alone, we only access the $\hat{X}_1$ quadrature fluctuations and there is no direct way to assess the full noise ellipse. **b.** Double BAE noise ellipse. Considered as separate measurements, the pump BAE elongates the mechanical noise ellipse along the $\hat{X}_2$ quadrature axes. Set to measure $\hat{X}_\phi$, the probe BAE acts in kind and funnels noise into its associated conjugate quadrature $\hat{X}_{\phi+\pi/2}$. Operating simultaneously, each BAE set is sensitive to the back-action of the other (green and orange crosses).

phases $\phi = \theta, 0$:

$$S_{\hat{X}_\theta}[\omega] = \frac{1}{\omega^2 + (\frac{\gamma_m}{2})^2}\left[\gamma_m(2n_m^{th}+1) + 4\gamma_{\rm op}(2n_c^{th}+1)\sin^2\theta\right] \tag{4.73}$$

$$= \bar{S}^o_{\hat{X}_1}[\omega]\cos^2\theta + \bar{S}^o_{\hat{X}_2}[\omega]\sin^2\theta. \tag{4.74}$$

where the spectra $\bar{S}^o_{\hat{X}_1,\hat{X}_2}$ denote the quadrature spectra derived in Eqs. (4.32)-(4.33) for single BAE drive. Additionally, the pump BAE signal will be perturbed by the probe tones in a symmetric fashion,

$$S_{\hat{X}_1}[\omega] = \frac{1}{\omega^2 + (\frac{\gamma_m}{2})^2}\left[\gamma_m(2n_m^{th}+1) + 4\gamma_{\rm op}^{\rm probe}(2n_c^{th}+1)\sin^2\theta\right]. \tag{4.75}$$

Though the full system Hamiltonian can no longer be considered QND, the sets of pump and probe BAE drive act as independent QND measurements of their respective quadrature axes; each respective signal is only sensitive to the back-action heating of the other (Fig. 4.6). By sweeping the phase θ of the probe BAE, we perform a QND measurement of the rotated quadrature $\hat{X}_\theta$ and directly measure the back-action forces of the pump BAE measurement in-situ.

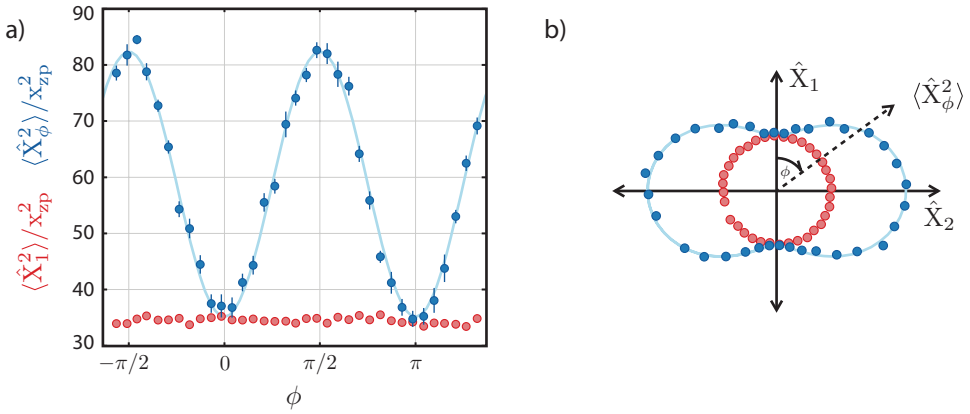

Figure 4.7: Quadrature variance over the full noise ellipse. **a.** The probe BAE senses the noise ellipse generated by the pump BAE tones. The quadrature ellipse follows the expected trend whereby all the measurement back-action is added to only a single quadrature. The pump BAE senses the back-action of the probe BAE which here are too weak to be detected above measurement noise. **b.** Quadrature noise variance in polar axes. Since we directly measure the noise variances, the noise ellipse resembles a peanut instead of an oval.

4.3.2 BAE phase locking

According to Eq. (4.74), introducing a second pair of probe BAE tones measures the mechanical noise ellipse dressed by the pump BAE drive. However, implementing this routine in our experiment requires one new technique that has not yet been discussed: phase control of the drive tones. In the following, we will discuss technical details for phase locking between the pair of BAE drive tones.

For simplicity, we align our lab frame clock such that the phase difference between the pair of pump BAE drives is zero. In this frame, the probe BAE measurement quadratures are rotated by $\theta = (\phi_+ - \phi_-)/2$, where ϕ_+ and ϕ_- are given by the incident phases of the probe drive tones. Due to the phase reduction by a factor of two, the incident drive phases must be controlled within $[0, 4\pi]$ to achieve quadrature detection over a full 2π rotation.

We can imagine performing this with open loop control by manually setting the relative phase of the microwave signal generators with internal or external phase control. Open loop control is accurate up to the quality of sources' phase drift. For phase stability, all signal generators are locked via a 10 MHz rubidium standard. However, in practice, we observe rms phase drifts on the scale of one degree per 10 minutes. We were unable to reduce the

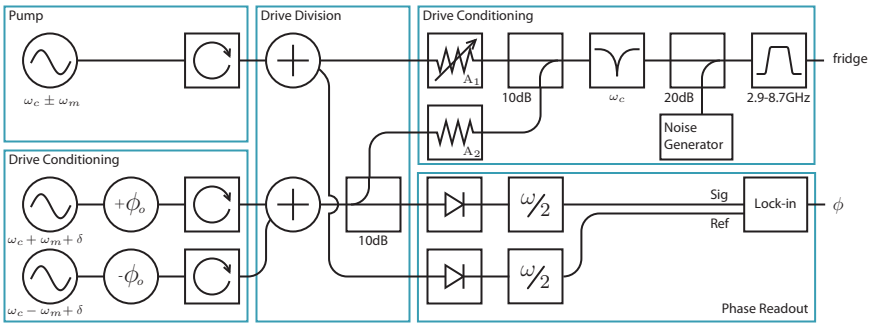

Figure 4.8: Phase locking circuit.

phase drifts beyond this nominal level despite optimizing the BNC timing circuit to increase mechanical stability, minimize delays between different sources and reduce pickup noise.

To remedy this phase drift issue, we implement closed loop control with manual feedback. Though we did implement an active feedback circuit for real-time phase control, we found that the manual phase control was more robust and more than adequate to deal with the timescale of our phase drifts. The feedback circuit is designed around phase readout for the pump BAE detection quadrature θ.

We will now discuss how we generate an error signal that is proportional to this phase. First, we peel off a small amount of power from a set BAE tones and feed it into a power diode (square law detector) followed by a RF low-pass filter with 11MHz cut-off frequency. This combination generates a low-frequency (LF) signal at the modulation frequency. Focusing on the component oscillating at twice the mechanical frequency,

$$\mathrm{LF}(t) = \left(\alpha(t)\right)^2\Big|_{2\omega_m} \tag{4.76}$$

$$= \alpha_{\pm}\cos(2\omega_m t + 2\theta), \tag{4.77}$$

Note that this error signal doubles both the frequency and phase of the modulation signal which causes complications for the detection. Suppose we generate the LF modulation signals from both pump and probe BAE signals and then read out the phase difference with a lock-in amplifier. The lock-in is sensitive to a single branch of phase spanning 2π and so, since mixing down to produce the LF signal doubles the phase shift, the lock-in can only supply

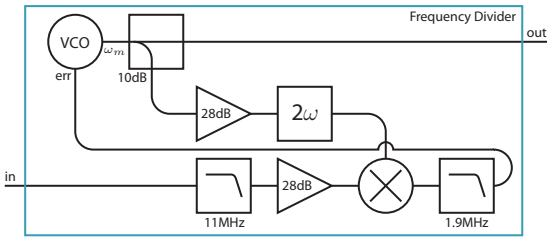

Figure 4.9: Frequency halving circuit.

half of the full sweep, $\theta \in [0, \pi]$.

To get closed loop control over the entire 2π range, we use an additional RF signal generator and create two signals on separate channels, oscillating at the mechanical frequency. Each channel is further divided in two, feeding into a frequency doubling circuit and a lock-in amplifier. The frequency-doubled signal from both channels are fed into separate PLL circuits that phase lock each channel to the pump and probe BAE LF signals, respectively. Refer to Fig. 4.8 and 4.9 for a schematic of the circuit. The phase difference between the un-doubled signals is monitored via a lock-in amplifier, which now supplies a one-to-one correspondence between error signal and relative BAE phase. We now have close-loop control over the entire quadrature noise ellipse.

4.3.3 Double BAE results

Using these phase-locking techniques, we are now able to directly measure mechanical back-action forces generated by a single BAE drive at $n_p = 1.1 \times 10^6$. We place a second set of probe BAE tones, 20dB weaker and detuned than the pump and detuned by $2\pi \times 30$ kHz. As we rotate the probe phase, it is clear that the back-action onto the mechanics is highly quadrature-dependent and follows closely along with Eq. 4.74 (Fig. 4.10(a)). Similarly, we see no apparent change in the $\hat{X}_1$ quadrature variance as measured by the pump tones which is consistent with the reduced back-action generated from the much weaker probe tones.

Fitting the probe noise ellipse to this model, we can now directly extract out the back-action onto the $\hat{X}_2$ quadrature. As we inject more and more classical noise into the cavity (following the same noise injection and noise floor calibration techniques of Sec. 3.3.2), we

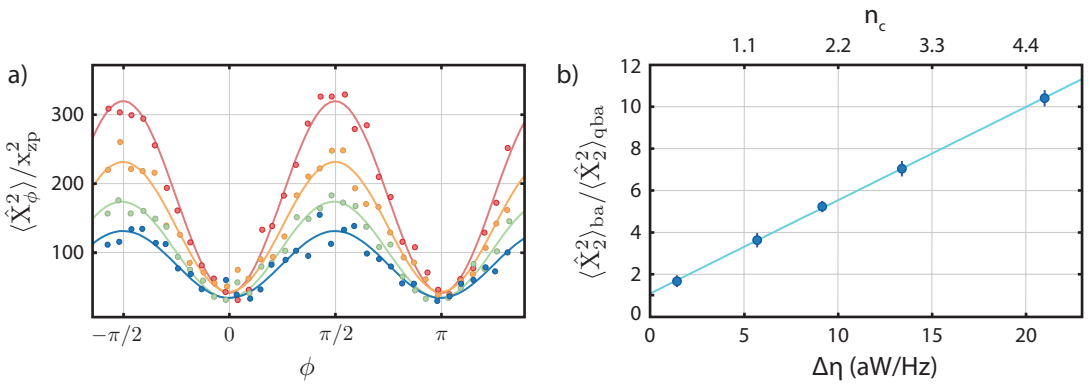

Figure 4.10: Backaction heating versus cavity noise. **a.** The mechanical quadrature variances are measured for increasing levels of cavity occupation. At elevated noise levels, the back-action heating of $\hat{X}_2$ increases while that of $\hat{X}_1$ stays fixed. **b.** As the cavity occupation increases, the noise floor shift $\Delta\eta$, representing the peak height of the cavity noise Lorentzian, is plotted against the $\hat{X}_2$ quadrature heating. Extracting to zero classical noise reveals the contribution of the quantum backaction induced by the quantum fluctuations of the microwave field.

repeat this measurement at each setting and extract out the back-action heating onto the $\hat{X}_2$ quadrature ($\langle \hat{X}_2^2 \rangle_{ba}$) as a function of the noise floor increase (Fig. 4.10(a)). According to Eq. (4.34), the measurement back-action is proportional to both classical and quantum noise, $\langle \hat{X}_2^2 \rangle_{ba} = (2\gamma_{\rm op}/\gamma_m)(2n_c^{th} + 1)$, such that the intercept at $n_c^{th} = 0$ reveals the back-action heating entirely due to the quantum fluctuations of the microwave field. Fitting our data (Fig. 4.10(b)) reveals an intercept of 1.1 ± 0.1, in excellent agreement with the expected quantum contribution of "+1". This is the first time that the quantum fluctuations of the microwave field [64, 65] is demonstrated via mechanical detection. Notably, this point corresponds to real mechanical motion that is driven by a completely empty cavity.

Chapter 5

Mechanical squeezing

5.1 Introduction

We now focus on generating a quantum squeezed mechanical state where the variance of a single motional quadrature is suppressed below the zero-point level [66], similar to squeezed states that have been produced in various other systems [67–73], . Given that ideal BAE detects the $\hat{X}_1$ quadrature while avoiding backaction heating, it would seem that BAE itself could generate a squeezed mechanical state. However, this is not the case. Due to the QND nature of this kind of measurement, the $\hat{X}_1$ quadrature is completely unaffected from measurement. For a single realization of the measurement on the timescale governed by the total mechanical dissipation, the mechanics is indeed squeezed. After repeated continuous measurement, however, the state is averaged out over the thermal distribution of the mechanics and we instead measure a conditional squeezed state. In this fashion, we observe no reduction in the quadrature noise from the initial thermal level as expected for a QND measurement.

There are numerous other proposals to generate mechanical squeezing via continuous measurement plus feedback, such as BAE quadrature detection with feedback [56, 58, 74, 75], position measurement with detuned parametric drive [76]. Implementing BAE with feedback is technically challenging as it requires an active feedback circuit for signal processing and sufficiently small measurement imprecision noise. Alternatively, we could implement a simpler parametric squeezing scheme [77], though single quadrature cooling is limited to 3 dB

before the mechanics reaches a parametric instablility [78] and hence quantum squeezing via parametric modulation is beyond our current capabilities. However, there are many other theoretical proposals to surpass this 3 dB limit [79–82].

Instead, we consider a dissipative bath engineering scheme that can produce arbitrarily large steady-state mechanical squeezing [83]. By simply increasing the strength of the red-detuned drive in the two-tone BAE drive configuration (Fig. 5.2), we no longer perform a QND measurement on $\hat{X}_1$. Instead, the backaction fores are correlated with the mechanical motion in such a way that, instead of quadrature-insensitive cooling, the electromechanical interaction forms a coherent feedback circuit that generates both steady-state mechanical squeezing and net cooling of both quadratures from their initial thermal levels. This scheme can be interpreted as a manifestation of reservoir engineering [84] realized in other bosonic systems [85–88].

Recently, we performed such a measurement and observed quantum squeezing [63]. Since then, two other groups have reported similar results in the microwave domain [89, 90]. In this chapter, we will briefly discuss the electromechanical squeezing interaction as it directly pertains to our system, followed by discussion of measurement and analysis techniques. The bulk of this chapter will address the issue of error analysis in such a routine: how can we systematically address correlated error between calibration uncertainty and fit uncertainty for error propagation to the quadrature occupations? Though there are multiple ways to tackle this problem, we will explore a Bayesian analysis routine that provides a relatively direct way to resolve this issue.

5.2 Squeezing and detection

We will first outline the squeezing interaction and, making a series of approximations, show that arbitrarily large steady-state mechanical squeezing is achievable with two-tone driving of an electromechanical system such as ours. However, as many of these approximations turn out to be violated due to nonidealities like power-dependent cavity [17] and mechanical heating [63], we will later relax these assumptions and show that mechanical squeezing is

still within reach.

5.2.1 Generating steady-state mechanical squeezing

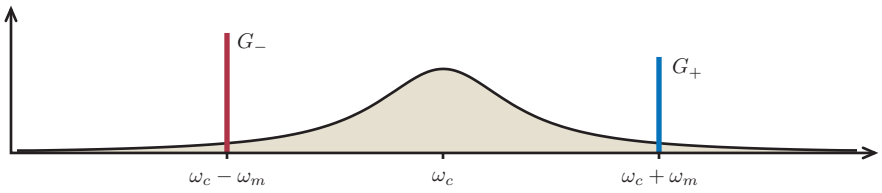

Figure 5.1: Mechanical squeezing pump configuration. A red- and blue-detuned pump (red and blue bars) are placed at ideal detunings $\omega_c \pm \omega_m$ about the cavity Lorentzian (beige). The pumps are power imbalanced such that there is excess red power, $G_- > G_+$.

As a first step, we model the interaction in the good cavity limit ($\frac{\omega_m}{\kappa} \gg 1$) with perfectly aligned and overlapped sidebands ($\delta, \Delta = 0$) for a cavity mode deep in the ground state ($n_c^{th} = 0$). Moving to the interaction picture rotating at ω_c, ω_m and displaced by a large coherent field $|\bar{a}_\pm| \gg 1$, the Hamiltonian simplifies to

$$\hat{\mathcal{H}}_{\text{int}} = -\hbar \hat{d}^\dagger (G_+ \hat{b}^\dagger + G_- \hat{b}) + H.c.\,, \tag{5.1}$$

$$= -\hbar G (\hat{d}^\dagger \hat{\beta} + \hat{d}\, \hat{\beta}^\dagger). \tag{5.2}$$

with enhanced optomechanical couplings $G_\pm = g_0 \bar{a}_\pm$. In the second line, we have expressed the electromechanical interaction in terms of a mechanical Bolgoliubov mode, $\hat{\beta}$, where

$$\hat{\beta} = \hat{b} \cosh r + \hat{b}^\dagger \sinh r, \tag{5.3}$$

with squeezing factor

$$\tanh r = \frac{G_+}{G_-}, \tag{5.4}$$

and effective coupling strength

$$G = \sqrt{G_-^2 - G_+^2}. \tag{5.5}$$

Analogous to sideband cooling ($G_+ = 0$) where the mechanical mode is cooled via cou-

pling to a cavity mode that is near the ground state, two tone drive ($G_- > G_+ > 0$) instead couples a mechanical Bolgoliubov mode to the cavity mode. For the imbalanced and overlapped two-tone drive configuration of Fig. 5.1, the mechanical Bolgoliubov mode, $\hat{\beta}$, represents the annihilation operator of a squeezed mechanical state. That is, $\hat{\beta}\hat{S}(r)\left|0\right\rangle = 0$ where $\hat{S}(r) = \exp[r(\hat{b}\,\hat{b} + \hat{b}^\dagger\hat{b}^\dagger)/2]$ is the squeeze operator. From the form of this interaction, cooling via cavity dissipation is capable of generating steady-state mechanical squeezing. In Sec. 5.3 we relax some of the above assumptions but show, via an input-output framework that we can indeed generate mechanical squeezing for experimentally accessible regimes.

5.2.2 Bolgoliubov mode detection

Following the assumptions outlined above – perfectly overlapped and centered drive tones, a cavity deep in the ground state ($n_c^{th} = 0$) and highly suppressed bad-cavity effects – we can analyze and detect mechanical squeezing by following the measurement protocol outlined in [83]. Here, the expressions for the quadrature occupation and squeeze factor simplify to compact equations in terms of the red drive cooperativity, $\mathcal{C} = 4G_-^2/(\kappa\gamma_m)$, and the mechanical bath occupation, n_m^{th}. The squeeze factor r follows

$$e^{-2r} \approx \frac{1}{2}\sqrt{\frac{1+2n_m^{th}}{\mathcal{C}}}, \tag{5.6}$$

while the squeezed quadrature occupation is

$$2\langle \hat{X}_1^2 \rangle \approx \frac{\gamma_m}{\kappa}(1+2n_m^{th}) + \sqrt{\frac{1+2n_m^{th}}{\mathcal{C}}}. \tag{5.7}$$

In terms of experimental measurables, the squeezing can be estimated directly from the output microwave noise spectrum, $S_R[\omega] = \int dt e^{i\omega t}\langle \hat{d}^\dagger_{R,\mathrm{out}}(0)\hat{d}_{R,\mathrm{out}}(t)\rangle$. Specifically, the integrated noise power is proportional to the Bolgoliubov mode occupation,

$$\int \frac{d\omega}{2\pi} S_R[\omega] \simeq \frac{4\kappa G^2}{4G^2 + \kappa(\kappa+\gamma_m)}\langle \hat{\beta}^\dagger\hat{\beta}\rangle. \tag{5.8}$$

For the limit of high cooperativity such that $n_m^{th}/\mathcal{C} \ll 1$, this relationship is sufficient for quadrature detection. In terms of $\hat{\beta}$ and $\hat{\beta}^\dagger$, the quadrature occupation is

$$\langle \hat{X}_1^2 \rangle = \frac{e^{-2r}}{2}\left(\langle \hat{\beta}^\dagger \hat{\beta}\rangle + \langle \hat{\beta}\hat{\beta}^\dagger\rangle + \langle \hat{\beta}^\dagger \hat{\beta}^\dagger\rangle + \langle \hat{\beta}\hat{\beta}\rangle\right). \tag{5.9}$$

Asserting the Cauchy-Schwarz inequality, the squeezing occupation obeys a rigorous upper bound

$$\langle \hat{X}_1^2 \rangle \leq e^{-2r}[1 + 2\langle \hat{\beta}^\dagger \hat{\beta}\rangle]. \tag{5.10}$$

This bound approaches an equality up to corrections on the order of $1/\sqrt{\mathcal{C}}$.

The above Eqs. (5.8)-(5.10) show that the integrated noise output noise spectrum serves as a proxy for mechanical squeeze detection. In practice, however, we implement a different measurement routine for the following reasons. First, we must relax various assumptions in the above analysis that are not applicable to our measurement system. Most importantly, we must account for classical cavity noise ($n_c^{th} > 0$) that is pump power dependent and internally generated within the microwave cavity. The cavity occupation changes the dependence of Eqs. (5.6)-(5.7) on both optimal cooperativity and optimal pump ratios. Furthermore, the sideband resolution of our device ($\frac{\omega_m}{\kappa} \approx 8$) introduces corrections to the microwave spectrum lineshape and quadrature occupations that, though small, are necessary for accurate squeeze estimation. Finally, we will show below that, due to pump-dependent cavity and mechanical heating, our optimal squeezing generates moderate levels of quantum squeezing. At these levels of squeezing, the rigorous upper bound of Eq. (5.10) overestimates the quadrature occupations above the zero-point level.

For these reasons, we take a different approach: we will calculate the quadrature occupations via the scattering matrix techniques outlined in Sec. 1.4. Instead of integrating over the output spectrum, we instead fit the detected noise spectrum to the output spectrum model, extract out the system parameters, then calculate the squeezed and amplified quadrature occupations as functions on the system parameters. In the following sections, we first discuss these techniques for perfectly overlapped and centered pumps. Later, we will

relax these assumptions and include all deleterious effects driven by the electromechanical interaction: imperfect pump tuning, bad cavity effects from finite sideband resolution, and sources of calibration error.

5.3 Squeezing models

We will first analyze the squeezing interaction assuming perfectly aligned drive tones and infinite sideband resolution. Under these assumptions, it is possible to generate relatively simple analytic models for the microwave spectrum and the quadrature occupations. We will later relax both of these assumptions and instead develop numerical spectrum models that will be used for spectrum fitting and quadrature extraction routines.

5.3.1 Ideal pumping with RWA

In this section, we calculate the quadrature occupations assuming ideal pump configuration and making the rotating wave approximation, and show that the two-tone drive does generate steady-state mechanical squeezing. To start, we derive all relevant spectrum and occupations from the scattering framework introduced in Sec. 1.4 and setting $\delta, \Delta = 0$. The complex transmission is given by Eq. (1.104) and follows

$$S_{21}[\omega] = \frac{-\sqrt{\kappa_R \kappa_L}(\gamma_m - 2i\omega)}{4G^2 + (\kappa - 2i\omega)(\gamma_m - 2i\omega)}. \tag{5.11}$$

For a given pump configuration with $G_\pm$ independently calibrated from measuring the drive powers at the detector, the driven response ensures that the transduced sidebands are overlapped and centered in the cavity. We also extract κ in-situ (with identical pump configuration) by fitting the measured spectrum to the model.

The output noise spectrum is given as

$$S_R[\omega] = \frac{1}{2}\int dt e^{i\omega t}\langle\{\hat{X}_i(0), \hat{X}_i(t)\}\rangle, \tag{5.12}$$

$$= 4\kappa_R \frac{(4\omega^2+\gamma_m^2)\kappa n_c^{th} + 4G_-^2\gamma_m n_m^{th} + 4G_+^2\gamma_m(n_m^{th}+1)}{|4G^2+(\kappa+2i\omega)(\gamma_m+2i\omega)|^2}. \tag{5.13}$$

With all the S_{21} parameters specified, the only fit parameters in the noise model is the cavity bath occupation n_c^{th} and the mechanical bath flux $\gamma_m n_m^{th}$. We keep the mechanical bath contribution specified as a flux opposed to separating into rate γ_m and occupation n_m^{th} since the flux is the most relevant parameter and we have no sensitivity to γ_m at these measurement powers, i.e., $\gamma_m \ll \gamma_{\rm tot}, \kappa$.

The mechanical quadrature spectrum is

$$\bar{S}_{\hat{X}_i}[\omega] = 4x_{\rm zp}^2 \frac{4(G_- \mp G_+)^2\kappa(n_c^{th}+\frac{1}{2}) + (\kappa^2+4\omega^2)\gamma_m(n_m^{th}+\frac{1}{2})}{|4G^2+(\kappa+2i\omega)(\gamma_m+2i\omega)|^2}, \tag{5.14}$$

with associated quadrature occupations

$$\langle\hat{X}_i^2\rangle = \int_{-\infty}^{\infty}\frac{d\omega}{2\pi}\bar{S}_{\hat{X}_i}[\omega] \tag{5.15}$$

$$= x_{\rm zp}^2 \frac{4(G_- \mp G_+)^2\kappa(2n_c^{th}+1) + [4G^2+\kappa(\kappa+\gamma_m)]\gamma_m(2n_m^{th}+1)}{(\kappa+\gamma_m)(4G^2+\kappa\gamma_m)}, \tag{5.16}$$

where the quadrature designation $i = 1, 2$ is associated with $\pm$, respectively, leading to suppression or enhancement of measurement backaction forces proportional to n_c^{th}. As predicted, the electromechanical interaction does produce steady-state mechanical squeezing via reservoir engineering.

5.3.2 General spectrum model

The above model is sensitive not only to the bath occupations n_c^{th} and $\dot{n}_m^{th} \equiv \gamma_m n_m^{th}$, but also the coupling rates $G_\pm$, linewidths κ and γ_m, and detunings δ, Δ. Though we do our best to calibrate these parameters, we must extract all such parameters from signals that come from

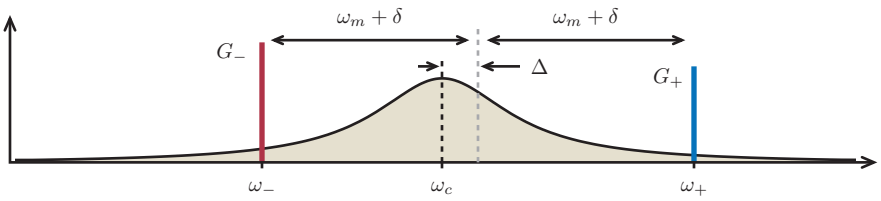

Figure 5.2: General pump configuration. Here, we include deviations from the ideal squeezing pump configuration in the form of detunings $\Delta = (\omega_+ + \omega_-)/2 - \omega_c$ associated with how well the drives are centered around the cavity and $\delta = (\omega_+ - \omega_-)/2 - \omega_m$ associated with how well the motional sidebands are overlapped.

microwave transmission and power detection spectra and hence we must always deal with numerous sources of measurement and calibration error that can propagate throughout such measurements. This outlines a general issue with how we make this measurement, there are eleven total system parameters that can effect the electromechanical squeezing interaction and we must consider how these parameters influence our results.

For accurate estimation and error analysis, we want a spectrum model that incorporates all system parameters that affect quadrature estimation, captures relevant system corrections like bad cavity or Kerr effects, and is defined entirely in terms of directly accessible measurement parameters. Fortuitously, the full scattering framework handles these issues in a compact fashion. We can define the scattering matrix elements as functions on calibration parameters and can iteratively expand the matrix to sufficiently large sideband order to include bad cavity effects or include Kerr cross-terms directly in the scattering matrix.

With arbitrary pump detunings and first-order bad cavity corrections, the analytic forms of Eqs. (5.13)-(5.16) become unwieldy and unfit for model fitting. After much effort to develop analytic models, it turns out to be sufficiently fast and much simpler to calculate the output spectrum via numerical inversion of the scattering matrix at each specified frequency.

5.4 Measurement

5.4.1 Calibration measurements

We begin by performing two measurements that calibrate the pump powers detected at the output of our measurement chain, $P_\pm = gain \times \hbar\omega_\pm \times \kappa_R \Delta_\pm n_p^\pm$, in terms of enhanced

optomechanical coupling rates, $G_\pm$, as well as the effective intracavity photon levels, $\Delta_\pm n_p^\pm$. Here, $\Delta_\pm$ is a correction factor that modifies the cavity transmission off resonance [16] and has no significance in the following analysis.

With scanning homodyne detection (i.e., via a driven response), we first measure the mechanical linewidth, $\gamma_{\rm tot} = \gamma_m + \gamma_{\rm op}$, as we increase the power, P_-, of a single pump red-detuned from the cavity center by ω_m. Here, $\gamma_{\rm op} = 4G_-^2/\kappa$ is the optically-induced mechanical damping. For $\gamma_{\rm tot} \ll \kappa$, the mechanical response is a simple Lorentzian dip and we fit $\gamma_{\rm op}$ vs. $P_\pm$ to obtain a calibration for G_-^2. As $\gamma_{\rm op}$ becomes comparable to κ, we fit the transmission data to a strong coupling model with $G_+ = 0$ and $\delta = 0$.

Next, we place two balanced pumps, detuned from cavity center by $\pm(\omega_m + 2\pi \times 500\,{\rm Hz})$ and with powers $P_\pm$, at sufficiently low powers so as not to add any damping or amplification of the thermal noise, and we measure the integrated mechanical noise power of up- and down-converted motional sidebands, $P_m^\pm$, over a range of cryostat temperatures T. Due to weak temperature and power dependence of κ [17], we monitor the cavity linewidth at each measurement power or temperature. The results of these calibrations are cast in a linear form and fit with ordinary least squares to extract the calibration factors a, b_- and b_+,

$$\left(\frac{\kappa}{\bar{\kappa}}\right)\gamma_{\rm opt} = \frac{4G_-^2}{\bar{\kappa}} = a\left(\frac{4}{\bar{\kappa}}\right)P_-, \tag{5.17}$$

$$\left(\frac{\kappa}{\bar{\kappa}}\right)^2\frac{P_m}{P_\pm} = b_\pm\left(\frac{2}{\bar{\kappa}}\right)^2\frac{k_B T}{\hbar\omega_m}, \tag{5.18}$$

where $\bar{\kappa}$ is the cavity linewidth averaged over the respective parameter range. We find

$$\begin{aligned} a &= (3.25 \pm 0.09) \times 10^{16}\,{\rm rad^2\,s^{-2}\,W^{-1}}, \\ b_- &= (3.82 \pm 0.14) \times 10^{4}\,{\rm rad^2\,s^{-2}}, \\ b_+ &= (6.84 \pm 0.22) \times 10^{4}\,{\rm rad^2\,s^{-2}}. \end{aligned}$$

We now are able to formulate the pump-dependent model parameters in terms of $P_{\pm}$,

$$G_{-}^{2} = a \times P_{-}, \tag{5.19}$$

$$G_{+}^{2} = a \left(\frac{b_{-}}{b_{+}} \right) \times P_{+}, \tag{5.20}$$

$$\Delta_{-} n_{p}^{-} = \left(\frac{a}{b_{-}} \right) \times P_{-}. \tag{5.21}$$

Eq. (5.20) follows from the balancing condition $\left(\frac{P_{-}}{P_{+}}\right)_{\text{balanced}} = \left(\frac{b_{-}}{b_{+}}\right)$.

Next, we introduce a second, blue-detuned drive and directly measure the pump powers $P_{\pm}$ which we use to extract the enhanced optomechanical coupling rates $G_{\pm}$ via Eqs. (5.19-5.21). Using an RWA model akin to Eq. (5.11), we fit the transmission spectrum via nonlinear least squares estimation and extract the frequency of the microwave resonator ω_c, the cavity linewidth κ, the frequency of the mechanical oscillator ω_m, and the pump detunings Δ, δ. The two pump tones are iteratively aligned to overlap the mechanical sidebands at the center of the cavity to ensure that δ is close to zero.

At this point, we now have a set of calibration parameters acquired in three methods: either directly measured ($P_{\pm}$), estimated from fits to transmission data (ω_c, ω_m, κ, Δ, δ), or extracted from independent calibration measurements (a, $b_{\pm}$). Each parameter represents an underlying probability distribution that captures the precision of each respective calibration. To simplify the following analysis, we assume the fit parameters are independent and normally distributed such that each parameter is associated with an underlying probability density function modeled as a Gaussian distribution with mean and variance given by the statistical estimators generated via measurement and fitting.

5.4.2 Noise spectrum measurement

Keeping the same two-tone pump configuration from the transmission calibration, we measure the microwave noise spectrum via linear detection. Calibrating out the gain of the

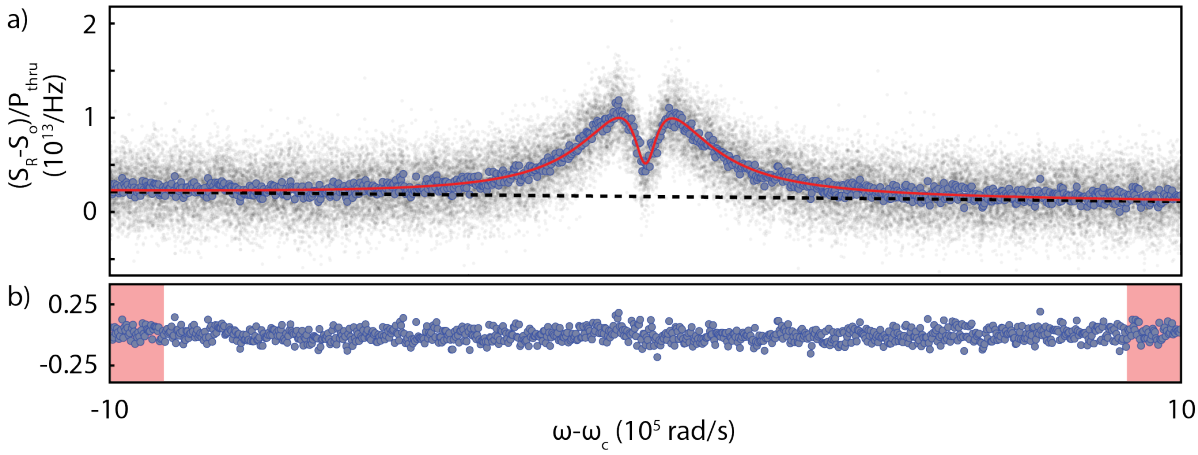

Figure 5.3: Squeezing noise spectrum. **a.** Raw noise spectrum (grey dots) and binned noise data (blue dots) fit to the squeezing spectrum model (red line). We include a linear noise floor offset (black dotted line) which we subtract off in later analysis. **b.** We calculate the data residuals (blue dots) by subtracting off the fit. We estimate the measurement noise from the sample variance of the residuals over a range far outside the cavity linewidth (red region).

output amplifier chain, the measured spectrum is given by

$$\bar{S}_{\text{out}}(\omega) = S_0(\omega) + S_R(\omega), \tag{5.22}$$

where $S_R(\omega)$ is the noise spectrum of the electro-mechanical system and $S_0(\omega)$ is the noise floor of the system. The noise floor is dominated by the noise figure of the cryogenic HEMT amplifier in addition to smaller power-dependent offsets due to phase noise from the entire amplifier chain. We spend an equal time interleaving measurements of the pumped and unpumped noise spectra over the same bandwidth. We subtract off the unpumped floor, then account for power-dependent amplifier effects by removing a linear floor offset that we fit over a span roughly seven times greater than the cavity linewidth. The linear offset matches independent measurements of the phase noise from our room temperature amplifier with matching pump configuration.

5.5 Bayesian parameter estimation and error analysis

Essential to any claim of sub-zero-point squeezing is the error bar for the reported quadrature occupation. Here, we consider a systematic approach to incorporate the uncertainty from all the sources of our measurement, including systematic calibration error, measurement noise, and the uncertainty from fitting the model to a measured noise spectrum. This problem has been addressed by Bayesian analysis techniques that explicitly incorporate all known sources of error. In the following, we largely follow the analysis outlined in Ch. 3 of [91]. Our purpose for using this analysis is to address the issue of estimating error bars from nonlinear fitting with a fit model that also has uncertainty.

In what follows, we develop statistical estimators for the quadrature occupations, $\langle X_{1,2}^2 \rangle$, from two sets of measurements: the detected noise spectrum and the system calibrations. Here, system calibration refers to the combination of initial calibrations (a, b_-, b_+), driven response data (κ, Δ, δ) and power detection (P_-, P_+). We refer to such parameters as $\beta = \{a, b_-, b_+, \kappa, \Delta, \delta, P_-, P_+\}$. The only remaining unknowns are the bath contributions, here denoted as $\alpha = \{n_c, \dot{n}_m^{th}\}$.

To systematically incorporate the uncertainty from our calibrations and spectrum measurements, we consider the Bayesian posterior distribution

$$p\left(\alpha, \beta | D, I\right) = \frac{1}{Z} p\left(D | \alpha, \beta, I\right) p\left(\alpha, \beta\right), \tag{5.23}$$

where D is the observed noise data, I is the set of all assumptions required for this analysis, $Z = p\left(D\right)$ is a normalization constant that is not necessary for sampling of the posterior, $p\left(D | \alpha, \beta, I\right)$ is the likelihood function, and $p\left(\alpha, \beta\right)$ is the prior distribution for α, β.

The prior distribution captures how well we have confined our calibrations in parameter space. Assuming all system parameters are independent, the prior simplifies to a product of single-parameter normal distributions, i.e., $p\left(\beta\right)$ is a product of Gaussian distributions with mean and variance set by the statistical estimators ($\bar{\alpha}_i$ and σ_{α_i}, respectively) for each system

calibration.

$$P(\alpha) = \prod_i \frac{1}{\sigma_{\alpha_i}\sqrt{2\pi}} \exp\left[-\frac{(\alpha - \bar{\alpha}_i)^2}{\sigma_{\alpha_i}^2}\right]. \tag{5.24}$$

For the unknowns, $p(\alpha)$ is the product of uninformed Jeffreys priors [91]; these priors are uniform in log space to be scale-invariant and are set here to span a decade above and below initial estimates for n_c, $\dot{n}_m^{th}$ specified by minimum bound $\beta_{i,\min}$ and maximum bound $\beta_{i,\max}$:

$$P(\beta) = \begin{cases} \prod_i \frac{1}{\log(\beta_{i,\max}/\beta_{i,\min})}\frac{1}{\beta_i}, & \text{for } \beta_i \in [\beta_{i,\min}, \beta_{i,\max}], \\ 0, & \text{otherwise.} \end{cases} \tag{5.25}$$

Since we operate in the high cooperativity regime and have no sensitivity to the intrinsic mechanical linewidth, we assume that the calibration parameter γ_m also follows an usninformed Jeffrey's prior.

The likelihood captures how well the data matches the noise spectrum model with specified α, β. We calculate residuals of the detected noise data $\{N_i\}$ by subtracting off the noise spectrum model $\{S_i\}$ calculated at frequencies matching the data. Next, we assume the measurement noise at each measured frequency is independent and Gaussian with identical variance. The measurement noise σ is directly sampled from noise data over a 150 kHz window detuned outside cavity center by $\pm 3\kappa$ (see Fig. 5.3). Hence, the likelihood is the product of residual probabilities derived from $N(0, \sigma)$,

$$P(D; \alpha, \beta, I) = \prod_i \frac{1}{\sigma\sqrt{2\pi}} \exp\left[-\frac{(N_i - S_i)^2}{2\sigma^2}\right]. \tag{5.26}$$

All together, we construct the posterior distribution as

$$P(\alpha, \beta; D, I) \propto p(D; \alpha, \beta, I) P(\alpha) P(\beta). \tag{5.27}$$

Since the posterior distribution is difficult to calculate analytically, we instead model the posterior via an affine-invariant Markov chain Monte Carlo (MCMC) ensemble sampler [92]. We implement this calculation with *emcee*, an open-source Python package developed in the

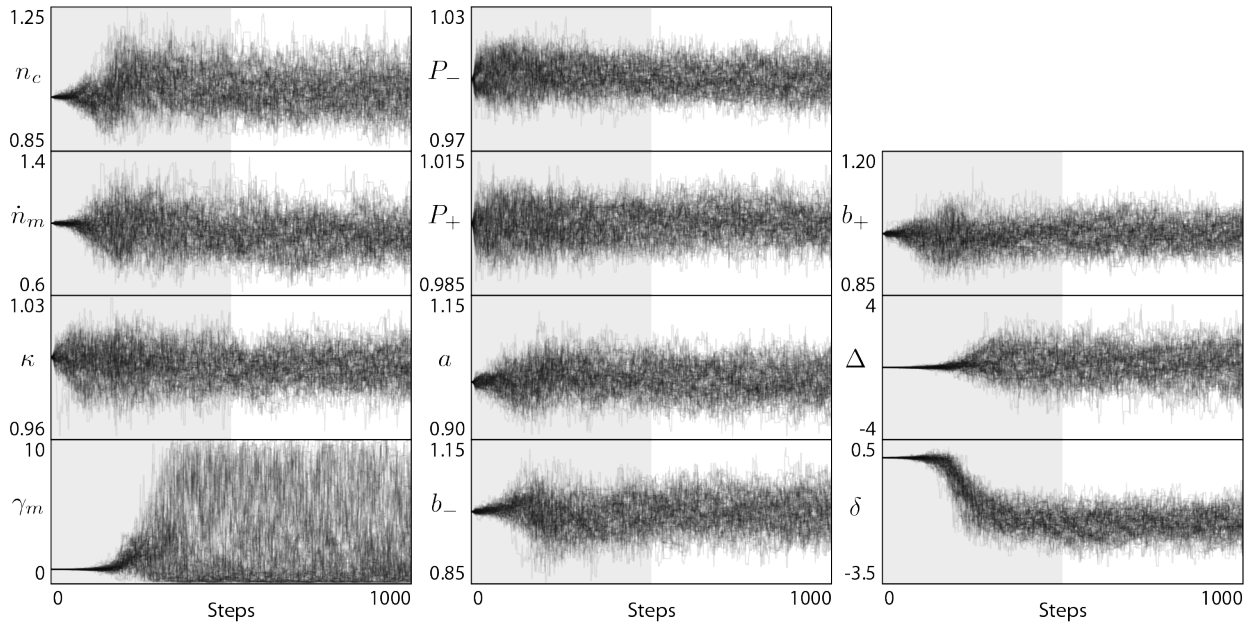

Figure 5.4: Markov chains generated via *emcee*. One hundred parallel walkers traverse the multi-dimensional parameters space over a period of one thousand steps. In steady-state, the walkers generate pseudo-random chains that accurately sample the Bayesian posterior distribution. As evidenced by the transient relaxation for many chains, the first five hundred steps (grey region) is discarded to ensure proper burn-in and parameter estimation is evaluated over the remaining samples.

astronomy community with over three hundred citations since 2012 [93]. With *emcee*, we generate a sufficiently large number of of pseudo-random parameter chains $(\alpha, \beta)_i$ sampled from the posterior distribution. For the calculation, we initialize a hundred walkers and run for a minimum of a thousand steps. We discard the first half to ensure that the resulting distributions are steady state (allowing initial transients to relax) but maintain a large enough sample size to render the Monte Carlo uncertainty negligible. These chains are displayed in Fig. 5.4 for the pump ratio $n_p^+/n_p^- = 0.4$.

In Fig. 5.5, we display the single parameter and pairwise histograms evaluated over the collection of MCMC chains. The single parameter histograms represent the marginalized distributions for each system parameter. Intriguingly, the pairwise distributions clearly display any correlations between system parameters.

Finally, we calculate expectation values and 1-σ intervals for n_c, $\dot{n}_m^{th}$ and $\langle X_{1,2}^2 \rangle$. For n_c and $\dot{n}_m^{th}$, we construct the marginalized distributions from their respective Markov chains and then tabulate the statistical estimators for mean and variance. For the mechanical

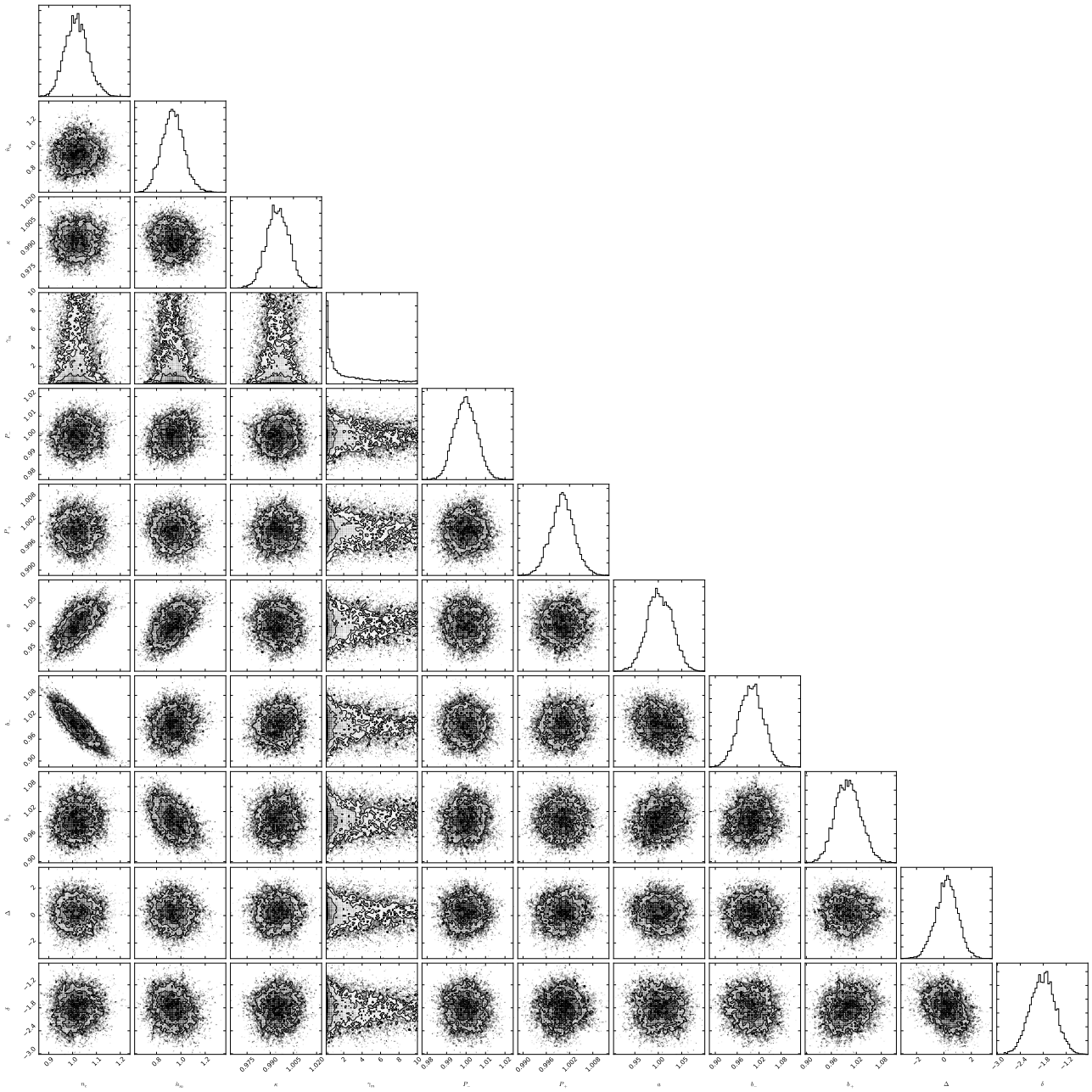

Figure 5.5: Triangle plot of single and pairwise parameter distributions. The posterior distribution is projected into pairwise distributions and single parameter histograms. MCMC sampling techniques provide direct access to visualize all correlations between system parameters. All parameters are normalized by their respective estimates acquired from calibration measurements or maximum likelihood estimation. Again, the first five hundred steps are discarded to ensure MCMC burn-in.

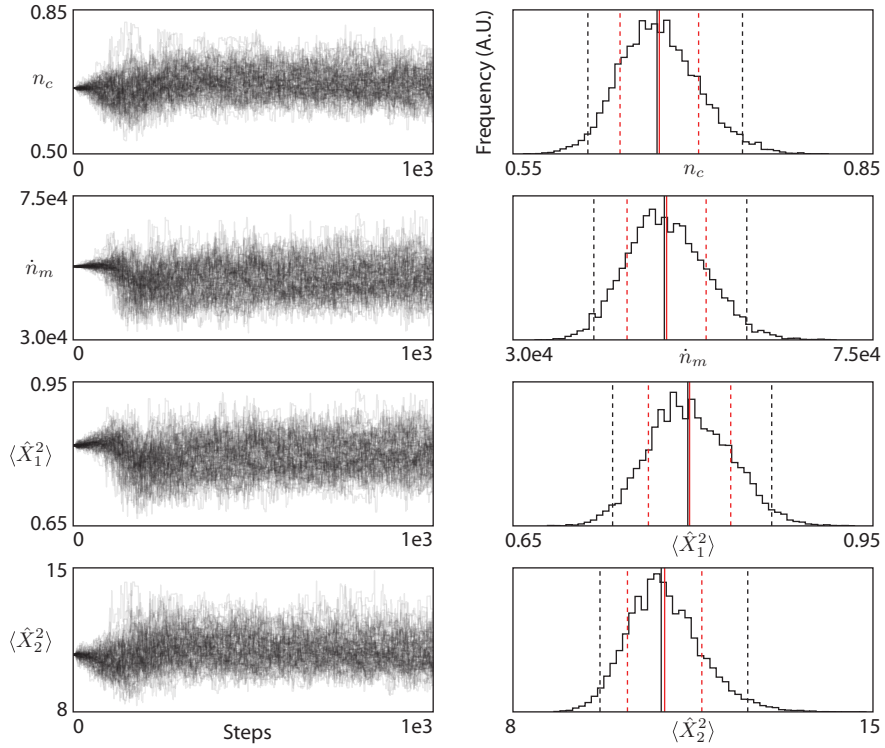

Figure 5.6: Parameter estimation. The MCMC chains corresponding to the individual fit parameters n_c^{th} and $\dot{n}_m^{th}$ sample the marginalized fit parameter distributions. The quadrature occupations are extracted via function evaluation over the entire set of MCMC chains for all system parameters. From these chains, we evaluate the mean (solid red line), 1-σ interval (dotted red lines) defined via the sample variance, as well as the median (solid black lines) and 95% quantiles (dotted black lines).

quadratures, we calculate expectation values for functions of system parameters, $f(\alpha, \beta)$, with function evaluation over the entire MCMC ensemble,

$$\langle f \rangle = \int f(\alpha, \beta)\, p(\alpha, \beta | D, I)\, d\alpha d\beta, \tag{5.28}$$

$$\simeq \frac{1}{N} \sum_{i=1}^{N} f(\alpha, \beta)_i. \tag{5.29}$$

The mean and standard deviation for $\langle X_{1,2}^2 \rangle$ are generated via Eq. (5.29) with $f(\alpha, \beta)$ set to the mechanical quadrature functions discussed in Sec. 5.3.2. Examples of the quadrature chains with associated histograms and parameter estimators is presented in Fig. 5.6.

5.5.1 Comparison to Monte Carlo calibration simulation

As a consistency check, we also perform a more typical data analysis routine that is based on nonlinear least square fitting. Instead of incorporating the calibration uncertainty in the form of Bayesian priors, we will instead use Monte Carlo techniques to simulate a large set of random calibration parameters α sampled from the multivariate normal distribution described in Eq. (5.24). For each random set of calibration factors, we generate a new noise spectrum model and then use maximum likelihood estimation to extract the mean and variance of the fit parameters β. We repeat this process over the entire population of the simulated calibration sets and, via function evaluation over the entire sample population of α and β, calculate the mean and variance of that quadrature occupations. At this point, the quadrature variance is entirely due to the calibration uncertainty. It is not clear how to incorporate the fit uncertainty since we have no way of tracking correlations between the calibration uncertainty in α (incorporated here via Monte Carlo simulation) and fit uncertainty in β (estimated from least squares parameter estimation). Instead, we assume here that the fit error, σ_{β_i}, independently propagates into the quadrature occupations via standard linear error propagation,

$$\sigma^2_{\hat{X}_1} = \sigma^2_{\hat{X}_1}\Big|_{\text{cal}} + \sum_i \left(\frac{\partial\langle\hat{X}_1^2\rangle}{\partial\beta_i}\right)^2 \sigma^2_{\beta_i}. \tag{5.30}$$

At optimal squeezing, this Monte Carlo analysis estimates the quadrature occupation as $\langle\hat{X}_1^2\rangle/x^2_{\text{zp}} = 0.80 \pm 0.04$, consistent with the Bayesian analysis results. The strength of the Bayesian analysis is that it does not rely on assumptions about correlations between calibration and fit uncertainty.

5.6 Results

We now present mechanical squeezing results over the full range of pump power ratios used in the experiment. At each configuration, we adjust the ratio between red- and blue-drive

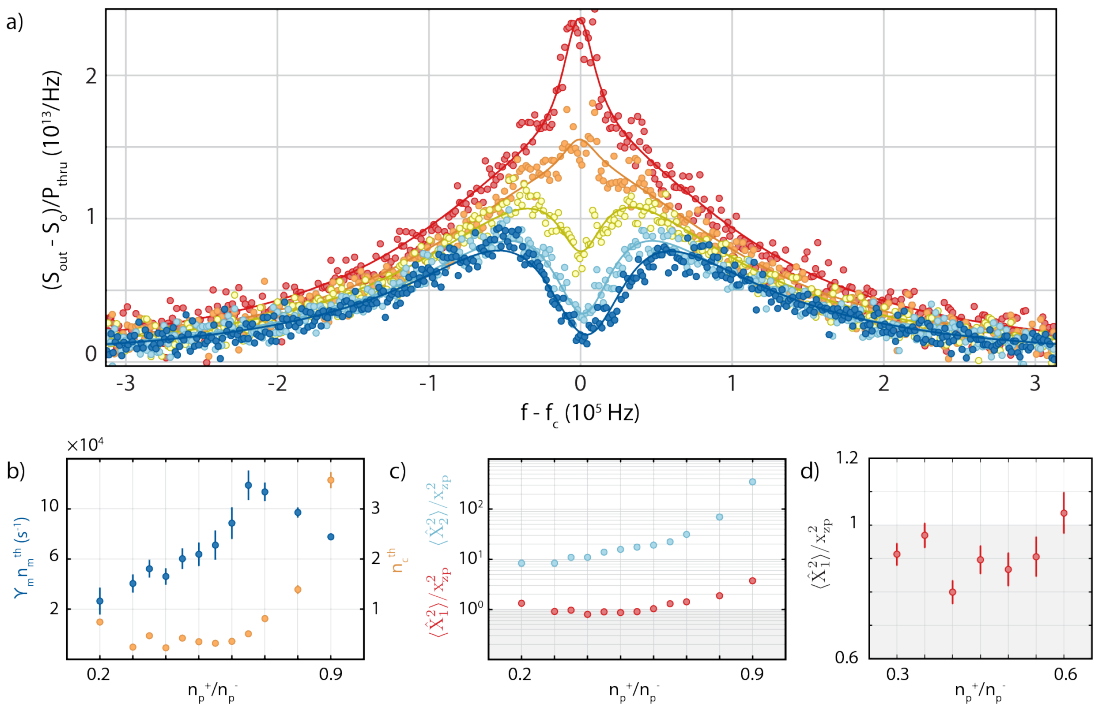

Figure 5.7: Squeezing results. **a.** Example noise spectrum and fits for pump ratios $n_p^+/n_p^- = 0.3$, 0.4, 0.5, 0.6 and 0.65 (ordered from blue to red). **b.** Bath occupation factors n_c^{th} (yellow) and $\dot{n}_m^{th}$ (blue). We observe ratio dependent heating in both the cavity and mechanical bath contributions. **c.** Quadrature estimation for $\langle \hat{X}_1^2 \rangle$ (red) and $\langle \hat{X}_2^2 \rangle$ (blue). **d.** We observe quantum squeezing $\langle \hat{X}_1^2 \rangle < x_{zp}^2$ at pump ratios between 0.3 to 0.55. At the lowest point, we cool a single quadrature of the mechanics to 0.80 ± 0.03 times the zero-point level.

powers while keeping the total pump power fixed at $n_p^- + n_p^+ = 1.76 \times 10^7$ and repeat the calibration and measurement routines. Typical noise spectra for a selection of power ratios is presented in Fig. 5.7(a). We then extract the bath occupations $\{n_c^{th}, \dot{n}_m^{th}\}$ and quadrature occupations $\langle \hat{X}_{1,2}^2 \rangle$ as shown in Fig. 5.7(b)-(d). Though we observe ratio-dependent heating for both the mechanical and cavity baths, we achieve mechanical squeezing with quadrature occupation below the zero-point level for a range of pump configurations.

In Fig. 5.7(c) and (d), we observe optimal squeezing at an intermediate power ratio consistent with the trends of [83]. We can understand this behavior as follows. As the pump ratio approaches zero, the pump configuration corresponds to sideband cooling [45] such that the quadrature occupation is asymptotically limited to the zero-point level. At the other end, as the pump ratio approaches unity, the pump configuration becomes BAE detection

which again ensures single quadrature occupation at or above the zero-point level.

The trend of the quadrature occupation of Fig. 5.7(c) – the gradual decrease in occupation as the pump ratio increases from zero followed by an abrupt increase for ratios approaching unity – is similar in appearance to the trend of Eqs. 5.16 derived with zero bath heating. The main affects of the microwave and mechanical bath heating is to reduce the squeezing efficiency, modify the optimal cooperativity, and skew the squeezing extrema to lower ratios. All of these effects will crucially depend on how the bath heating scales with the drive powers. Keeping the total power fixed, we observe increased bath heating as the red and blue powers ratio tends to unity (see Fig. 5.7(b)). The source of this heating is not entirely clear however we believe it is consistent with a nonlinear dielectric composed of two-level fluctuators [17, 25, 94, 95].

In addition to the issue of bath heating, both the mechanics and cavity also exhibit Kerr nonlinearities [15, 17] leading to noise squeezing and quadrature-dependent amplification at sufficiently large drive powers. These effects introduce off-axis correlations between the mechanical (microwave) quadratures that can potentially alter our spectral analysis. In our current measurements, we rule out the influence of the Kerr effects in in the following manner. For the mechanics, we directly observe any quadrature-dependent linewidth narrowing and broadening, a feature that is directly related to parametric squeezing [77], by performing single quadrature BAE detection over the full quadrature phase space. At the drive powers used in our work, we observe no significant mechanical linewidth modulation. For the cavity, we extract the Kerr factor by directly measuring the four-wave mixing at the relevant pump powers. We find that the effect is not relevant in our parameter regime.

5.7 Conclusion

In conclusion, we have generated a non-classical state of a macroscopic mechanical resonator [63] and have extracted a single quadrature variance as small as 0.80 times the zero-point level. Most significantly, our squeezing is limited due to power-dependent heating of the mechanical and microwave baths. If this heating behavior is indeed associated with

a nonlinear dielectric, then we can imagine a few device modifications that could potentially mitigate these effects. Increasing the bare optomechanical coupling would allow us to reach sufficiently large cooperativity at lower drive powers. Alternatively, we could work to suppress the influence of the intrinsic bath by increasing the external coupling to the microwave cavity and thereby dilute the contribution of the internal loss, though it is difficult to understand this behavior without a full microscopic model for TLS-induced bath heating. Another possibility would be to increase the sideband resolution of our device. Larger pump detunings could sample a higher frequency range of the 1/f phase noise envelope of the TLS dielectric noise [96], assuming our mechanical frequency is well below the white noise cut-off frequency of the dielectric noise spectrum.

In terms of continued work in this area, the next logical step is to verify mechanical squeezing via quadrature-sensitive mechanical detection, i.e., QND quadrature detection via BAE. We have already implemented this in our current device by introducing two additional BAE tones sufficiently detuned from the squeezing pumps [63]. However, we again are limited by bath heating issues that, with the introduction of BAE tones, degrade the amount of motional squeezing to above the quantum level. By shifting the BAE tones off of cavity center on the order of the cavity linewidth, we necessarily filter out our mechanical signals which significantly reduce the signal to noise ratio of the mechanical signals. Even at the lowest available BAE pump powers, we observe elevated cavity and mechanical bath heating that limits the squeezed mechanical quadrature occupation to 1.09 times the zero-point level.

There are numerous ways to overcome this issue of limited BAE sensitivity. One such technique, implemented elsewhere [90], is to engineer additional cavity modes that are all coupled to the mechanics via the standard optomechanical interaction. With additional cavity modes, the squeezing and BAE drive tones can address separate cavity modes and thereby eliminate any direct correlations between the drives. One can now place all mechanical signals tightly in the center of their respective cavity lineshapes and resolved weak BAE detection becomes feasible. Alternatively, one could also engineer an improved device to reach the quantum squeezing regime at lower cooperativities. By squeezing in the weak coupling regime, one can fit all necessary signals tightly within the cavity linewidth. Assum-

ing the BAE drive powers can be decreased to the extent that bath heating is insignificant, it is now possible to reach mechanical squeezing and BAE detection at the quantum level. This last topic is the focus of current work.

Bibliography

[1] D. M. Pozar, *Microwave Engineering, 4th Edition*, Wiley, 2011.

[2] J. B. Hertzberg, *Back-action evading measurements of nanomechanical motion approaching quantum limits*, Ph.D. thesis, University of Maryland, College Park, 2009.

[3] S. Weis, R. Rivière, S. Deléglise, E. Gavartin, O. Arcizet, A. Schliesser, and T. J. Kippenberg, "Optomechanically induced transparency," *Science*, vol. 330, no. 6010, pp. 1520–1523, 2010.

[4] J. D. Teufel, D. Li, M. S. Allman, K. Cicak, A. J. Sirois, J. D. Whittaker, and R. W. Simmonds, "Circuit cavity electromechanics in the strong-coupling regime," *Nature*, vol. 471, no. 7337, pp. 204–208, 2011.

[5] A. H. Safavi-Naeini, T. P. M. Alegre, J. Chan, M. Eichenfield, M. Winger, Q. Lin, J. T. Hill, D. E. Chang, and O. Painter, "Electromagnetically induced transparency and slow light with optomechanics," *Nature*, vol. 472, no. 7341, pp. 69–73, 2011.

[6] J. D. Teufel, T. Donner, D. Li, J. W. Harlow, M. S. Allman, K. Cicak, A. J. Sirois, J. D. Whittaker, K. W. Lehnert, and R. W. Simmonds, "Sideband cooling of micromechanical motion to the quantum ground state," *Nature*, vol. 475, pp. 359–363, 2011.

[7] J. Chan, T. P. M. Alegre, A. H. Safavi-Naeini, J. T. Hill, A. Krause, S. Gröblacher, M. Aspelmeyer, and O. Painter, "Laser cooling of a nanomechanical oscillator into its quantum ground state," *Nature*, vol. 478, no. 7367, pp. 89–92, 2011.

[8] F Massel, TT Heikkilä, J-M Pirkkalainen, SU Cho, H Saloniemi, PJ Hakonen, and MA Sillanpää, "Microwave amplification with nanomechanical resonators," *Nature*, vol. 480, no. 7377, pp. 351–354, 2011.

[9] A. H. Safavi-Naeini, S. Gröblacher, J. T. Hill, J. Chan, M. Aspelmeyer, and O. Painter, "Squeezed light from a silicon micromechanical resonator," *Nature*, vol. 500, no. 7461, pp. 185–189, 2013.

[10] T. P. Purdy, P-L Yu, R. W. Peterson, N. S. Kampel, and C. A. Regal, "Strong optomechanical squeezing of light," *Physical Review X*, vol. 3, no. 3, pp. 031012, 2013.

[11] A. A. Clerk, M. H. Devoret, S. M. Girvin, F. Marquardt, and R. J. Schoelkopf, "Introduction to quantum noise, measurement, and amplification," *Rev. Mod. Phys.*, vol. 82, pp. 1155–1208, Apr 2010.

[12] C. W. Gardiner and M. J. Collett, "Input and output in damped quantum systems: Quantum stochastic differential equations and the master equation," *Phys. Rev. A*, vol. 31, pp. 3761–3774, Jun 1985.

[13] L. Mandel and E. Wolf, *Optical coherence and quantum optics*, Cambridge university press, 1995.

[14] R. J. Glauber, *Quantum theory of optical coherence: selected papers and lectures*, John Wiley & Sons, 2007.

[15] J. Suh, M. D. Shaw, H. G. LeDuc, A. J. Weinstein, and K. C. Schwab, "Thermally induced parametric instability in a back-action evading measurement of a micromechanical quadrature near the zero-point level," *Nano Letters*, vol. 12, no. 12, pp. 6260–6265, 2012.

[16] A. J. Weinstein, C. U. Lei, E. E. Wollman, J. Suh, A. Metelmann, A. A. Clerk, and K. C. Schwab, "Observation and interpretation of motional sideband asymmetry in a quantum electromechanical device," *Physical Review X*, vol. 4, no. 4, pp. 041003, 2014.

[17] J. Suh, A. J. Weinstein, and K. C. Schwab, "Optomechanical effects of two-level systems in a back-action evading measurement of micro-mechanical motion," *Applied Physics Letters*, vol. 103, no. 5, pp. 052604, 2013.

[18] T. Rocheleau, T. Ndukum, C. Macklin, J. B. Hertzberg, A. A. Clerk, and K. C. Schwab, "Preparation and detection of a mechanical resonator near the ground state of motion," *Nature*, vol. 463, no. 7277, pp. 72–75, 2010.

[19] J. B. Hertzberg, T. Rocheleau, T. Ndukum, M. Savva, A. A. Clerk, and K. C. Schwab, "Back-action-evading measurements of nanomechanical motion," *Nature Physics*, vol. 6, no. 3, pp. 213–217, 2010.

[20] K. Cicak, D. Li, J. A. Strong, M. S. Allman, F. Altomare, A. J. Sirois, J. D. Whittaker, J. D. Teufel, and R. W. Simmonds, "Low-loss superconducting resonant circuits using vacuum-gap-based microwave components," *Applied Physics Letters*, vol. 96, no. 9, pp. 093502, 2010.

[21] J. Krupka, J. Breeze, A. Centeno, N. Alford, T. Claussen, and L. Jensen, "Measurements of permittivity, dielectric loss tangent, and resistivity of float-zone silicon at microwave frequencies," *Microwave Theory and Techniques, IEEE Transactions on*, vol. 54, no. 11, pp. 3995–4001, 2006.

[22] S. S. Mohan, M. del Mar Hershenson, S. P. Boyd, and T. H. Lee, "Simple accurate expressions for planar spiral inductances," *Solid-State Circuits, IEEE Journal of*, vol. 34, no. 10, pp. 1419–1424, 1999.

[23] I. Wilson-Rae, R. A. Barton, S. S. Verbridge, D. R. Southworth, B. Ilic, H. G. Craighead, and J. M. Parpia, "High-q nanomechanics via destructive interference of elastic waves," *Physical review letters*, vol. 106, no. 4, pp. 047205, 2011.

[24] R. Barends, N. Vercruyssen, A. Endo, P. J. de Visser, T. Zijlstra, T. M. Klapwijk, P. Diener, S. J. C. Yates, and J. J. A. Baselmans, "Minimal resonator loss for circuit quantum electrodynamics," *Applied Physics Letters*, vol. 97, no. 2, 2010.

[25] Jiansong Gao, *The physics of superconducting microwave resonators*, Ph.D. thesis, California Institute of Technology, 2008.

[26] G. D. Cole, E. Behymer, L. L. Goddard, and T. C. Bond, "Fabrication of suspended dielectric mirror structures via xenon difluoride etching of an amorphous germanium sacrificial layer," *Journal of Vacuum Science & Technology B*, vol. 26, no. 2, pp. 593–597, 2008.

[27] D. S. Gardner and P. A. Flinn, "Mechanical stress as a function of temperature in aluminum films," *Electron Devices, IEEE Transactions on*, vol. 35, no. 12, pp. 2160–2169, 1988.

[28] C. J. Santoro, "Thermal cycling and surface reconstruction in aluminum thin films," *Journal of the Electrochemical Society*, vol. 116, no. 3, pp. 361–364, 1969.

[29] F. M. dHeurle, "Aluminum films deposited by rf sputtering," *Metallurgical and Materials Transactions B*, vol. 1, no. 3, pp. 725–732, 1970.

[30] N. Fujitsuka, K. Hamaguchi, H. Funabashi, E. Kawasaki, and T. Fukada, "Silicon anisotropic etching without attacking aluminum with si and oxidizing agent dissolved in tmah solution," *Sensors and Actuators A: Physical*, vol. 114, no. 2, pp. 510–515, 2004.

[31] Richard Alexander Norte, *Nanofabrication for On-Chip Optical Levitation, Atom-Trapping, and Superconducting Quantum Circuits*, Ph.D. thesis, 2015.

[32] R. C. Bialczak, R. McDermott, M. Ansmann, M. Hofheinz, N. Katz, E. Lucero, M. Neeley, A. D. OConnell, H. Wang, A. N. Cleland, et al., "1/f flux noise in josephson phase qubits," *Physical review letters*, vol. 99, no. 18, pp. 187006, 2007.

[33] R. Barends, J. Wenner, M. Lenander, Y. Chen, R. C. Bialczak, J. Kelly, E. Lucero, P. OMalley, M. Mariantoni, D. Sank, et al., "Minimizing quasiparticle generation from stray infrared light in superconducting quantum circuits," *Applied Physics Letters*, vol. 99, no. 11, pp. 113507, 2011.

[34] Daniel Slichter, *Quantum jumps and measurement backaction in a superconducting qubit*, Ph.D. thesis, University of California, Berkeley, 2011.

[35] V. B. Braginsky and F. Y. Khalili, *Quantum Measurement*, Cambridge University Press, 1992.

[36] D. H. Santamore, A. C. Doherty, and M. C. Cross, "Quantum nondemolition measurement of fock states of mesoscopic mechanical oscillators," *Phys. Rev. B*, vol. 70, no. 14, pp. 144301, 2004.

[37] A. A. Clerk, F. Marquardt, and J. G. E. Harris, "Quantum measurement of phonon shot noise," *Phys. Rev. Lett.*, vol. 104, no. 21, pp. 213603, 2010.

[38] A. Muthukrishnan, M. O. Scully, and M. S. Zubairy, *The nature of light: what is a photon?*, CRC Press, 2008.

[39] F. Diedrich, J. C. Bergquist, W. M. Itano, and D. J. Wineland, "Laser cooling to the zero-point energy of motion," *Phys. Rev. Lett.*, vol. 62, pp. 403, 1989.

[40] P. S. Jessen, C. Gerz, P. D. Lett, W. D. Phillips, S. L. Rolston, R. J. C. Spreeuw, and C. I. Westbrook, "Observation of quantized motion of rb atoms in an optical field," *Physical review letters*, vol. 69, no. 1, pp. 49, 1992.

[41] C. Monroe, D. M. Meekhof, B. E. King, S. R. Jefferts, W. M. Itano, D. J. Wineland, and P. Gould, "Resolved-sideband raman cooling of a bound atom to the 3d zero-point energy," *Physical Review Letters*, vol. 75, no. 22, pp. 4011, 1995.

[42] J. Suh, A. J. Weinstein, C. U. Lei, E. E. Wollman, S. K. Steinke, P. Meystre, A. A. Clerk, and K. C. Schwab, "Mechanically detecting and avoiding the quantum fluctuations of a microwave field," *Science*, vol. 344, no. 6189, pp. 1262–1265, 2014.

[43] A. H. Safavi-Naeini, J. Chan, J. T. Hill, T. P. M. Alegre, A. Krause, and O. Painter, "Observation of quantum motion of a nanomechanical resonator," *Phys. Rev. Lett.*, vol. 108, pp. 033602, Jan 2012.

[44] N. Brahms, T. Botter, S. Schreppler, D. W. C. Brooks, and D. M. Stamper-Kurn, "Optical detection of the quantization of collective atomic motion," *Physical Review Letters*, vol. 108, no. 13, pp. 133601, 2012.

[45] F. Marquardt, J. P. Chen, A. A. Clerk, and S. M. Girvin, "Quantum theory of cavity-assisted sideband cooling of mechanical motion," *Phys. Rev. Lett.*, vol. 99, pp. 093902, 2007.

[46] S. M. Meenehan, J. D. Cohen, G. S. MacCabe, F. Marsili, M. D. Shaw, and O. Painter, "Pulsed excitation dynamics of an optomechanical crystal resonator near its quantum ground-state of motion," *arXiv preprint arXiv:1503.05135*, 2015.

[47] F. Lecocq, J. D. Teufel, J. Aumentado, and R. W. Simmonds, "Resolving the vacuum fluctuations of an optomechanical system using an artificial atom," *Nature Physics*, 2015.

[48] A. A. Clerk, "Quantum-limited position detection and amplification: A linear response perspective," *Phys. Rev. B*, vol. 70, pp. 245306, Dec 2004.

[49] F. Y. Khalili, H. Miao, H. Yang, A. H. Safavi-Naeini, O. Painter, and Y. Chen, "Quantum back-action in measurements of zero-point mechanical oscillations," *Phys. Rev. A*, vol. 86, pp. 033840, Sep 2012.

[50] I. Wilson-Rae, N. Nooshi, W. Zwerger, and T. J Kippenberg, "Theory of ground state cooling of a mechanical oscillator using dynamical backaction," *Physical Review Letters*, vol. 99, no. 9, pp. 093901, 2007.

[51] J. B. Hertzberg, T. Rocheleau, T. Ndukum, M. Savva, A. A. Clerk, and K. C. Schwab, "Backaction evading measurements of nanomechanical motion," *Nature Physics*, vol. 463, pp. 72–75, 2009.

[52] T. P. Purdy, P.-L. Yu, N. S. Kampel, R. W. Peterson, K. Cicak, R. W. Simmonds, and C. A. Regal, "Optomechanical raman-ratio thermometry," *Phys. Rev. A*, vol. 92, pp. 031802, Sep 2015.

[53] D. Lee, M. Underwood, D. Mason, A. B. Shkarin, K. Borkje, S. M. Girvin, and J. G. E. Harris, "Observation of quantum motion in a nanogram-scale object," *arXiv preprint arXiv:1406.7254*, 2014.

[54] Braginskiĭ, "Quantum-mechanical limitations in macroscopic experiments and modern experimental technique," .

[55] K. S. Thorne, R. W. P. Drever, C. M. Caves, M. Zimmermann, and V. D. Sandberg, "Quantum nondemolition measurements of harmonic oscillators," *Physical Review Letters*, vol. 40, no. 11, pp. 667, 1978.

[56] V. B. Braginsky, Y. I. Vorontsov, and K. S. Thorne, "Quantum nondemolition measurements," *Science*, vol. 209, no. 4456, pp. 547–557, 1980.

[57] Mark F Bocko and Roberto Onofrio, "On the measurement of a weak classical force coupled to a harmonic oscillator: experimental progress," *Reviews of Modern Physics*, vol. 68, no. 3, pp. 755, 1996.

[58] A. A. Clerk, F. Marquardt, and K. Jacobs, "Back-action evasion and squeezing of a mechanical resonator using a cavity detector," *New Journal of Physics*, vol. 10, no. 9, pp. 095010, 2008.

[59] J. D. Teufel, T. Donner, M. A. Castellanos-Beltran, J. W. Harlow, and K. W. Lehnert, "Nanomechanical motion measured with an imprecision below that at the standard quantum limit," *Nature nanotechnology*, vol. 4, no. 12, pp. 820–823, 2009.

[60] G. Anetsberger, E. Gavartin, O. Arcizet, Q. P. Unterreithmeier, E. M. Weig, M. L. Gorodetsky, J. P. Kotthaus, and T. J. Kippenberg, "Measuring nanomechanical motion with an imprecision below the standard quantum limit," *Physical Review A*, vol. 82, no. 6, pp. 061804, 2010.

[61] A. Naik, O. Buu, M. D. LaHaye, A. D. Armour, A. A. Clerk, M. P. Blencowe, and K. C. Schwab, "Cooling a nanomechanical resonator with quantum back-action," *Nature*, vol. 443, no. 7108, pp. 193–196, 2006.

[62] K. W. Murch, K. L. Moore, S. Gupta, and D. M. Stamper-Kurn, "Observation of quantum-measurement backaction with an ultracold atomic gas," *Nature Physics*, vol. 4, no. 7, pp. 561–564, 2008.

[63] E. E. Wollman, C. U. Lei, A. J. Weinstein, J. Suh, A. Kronwald, F. Marquardt, A. A. Clerk, and K. C. Schwab, "Quantum squeezing of motion in a mechanical resonator," *Science*, vol. 349, no. 6251, pp. 952–955, 2015.

[64] R. H. Koch, D. J. Van Harlingen, and J. Clarke, "Measurements of quantum noise in resistively shunted josephson junctions," *Physical Review B*, vol. 26, no. 1, pp. 74, 1982.

[65] A. Fragner, M. Göppl, J. M. Fink, M. Baur, R. Bianchetti, P. J. Leek, A. Blais, and A. Wallraff, "Resolving vacuum fluctuations in an electrical circuit by measuring the lamb shift," *Science*, vol. 322, no. 5906, pp. 1357–1360, 2008.

[66] C. C. Gerry and P. L. Knight, *Introductory quantum optics*, Cambridge university press, 2005.

[67] R. E. Slusher, L. W. Hollberg, B. Yurke, J. C. Mertz, and J. F. Valley, "Observation of squeezed states generated by four-wave mixing in an optical cavity," *Physical Review Letters*, vol. 55, no. 22, pp. 2409, 1985.

[68] B. Yurke, P. G. Kaminsky, R. E. Miller, E. A. Whittaker, A. D. Smith, A. H. Silver, and R. W. Simon, "Observation of 4.2-k equilibrium-noise squeezing via a josephson-parametric amplifier," *Physical review letters*, vol. 60, no. 9, pp. 764, 1988.

[69] D. M. Meekhof, C. Monroe, B. E. King, W. M. Itano, and D. J. Wineland, "Generation of nonclassical motional states of a trapped atom," *Physical Review Letters*, vol. 76, no. 11, pp. 1796, 1996.

[70] J. Hald, J. L. Sørensen, C. Schori, and E. S. Polzik, "Spin squeezed atoms: a macroscopic entangled ensemble created by light," *Physical review letters*, vol. 83, no. 7, pp. 1319, 1999.

[71] T. J. Dunn, J. N. Sweetser, I. A. Walmsley, and C. Radzewicz, "Experimental determination of the dynamics of a molecular nuclear wave packet via the spectra of spontaneous emission," *Physical review letters*, vol. 70, no. 22, pp. 3388, 1993.

[72] G. A. Garrett, A. G. Rojo, A. K. Sood, J. F. Whitaker, and R. Merlin, "Vacuum squeezing of solids: Macroscopic quantum states driven by light pulses," *Science*, vol. 275, no. 5306, pp. 1638–1640, 1997.

[73] D. Kienzler, H.-Y. Lo, B. Keitch, L. de Clercq, F. Leupold, F. Lindenfelser, M. Marinelli, V. Negnevitsky, and J. P. Home, "Quantum harmonic oscillator state synthesis by reservoir engineering," *Science*, vol. 347, no. 6217, pp. 53–56, 2015.

[74] C. M. Caves, K. S. Thorne, R. W. P. Drever, V. D. Sandberg, and M. Zimmermann, "On the measurement of a weak classical force coupled to a quantum-mechanical oscillator. i. issues of principle," *Rev. Mod. Phys.*, vol. 52, pp. 341–392, Apr 1980.

[75] R. Ruskov, K. Schwab, and A. N. Korotkov, "Squeezing of a nanomechanical resonator by quantum nondemolition measurement and feedback," *Physical Review B*, vol. 71, no. 23, pp. 235407, 2005.

[76] A. Szorkovszky, A. C. Doherty, G. I. Harris, and W. P. Bowen, "Mechanical squeezing via parametric amplification and weak measurement," *Physical review letters*, vol. 107, no. 21, pp. 213603, 2011.

[77] D Rugar and P Grütter, "Mechanical parametric amplification and thermomechanical noise squeezing," *Physical Review Letters*, vol. 67, no. 6, pp. 699, 1991.

[78] G Milburn and DF Walls, "Production of squeezed states in a degenerate parametric amplifier," *Optics Communications*, vol. 39, no. 6, pp. 401–404, 1981.

[79] K. Jähne, C. Genes, K. Hammerer, M. Wallquist, E. S. Polzik, and P. Zoller, "Cavity-assisted squeezing of a mechanical oscillator," *Physical Review A*, vol. 79, no. 6, pp. 063819, 2009.

[80] M. R. Vanner, I. Pikovski, G. D. Cole, M. S. Kim, Č. Brukner, K. Hammerer, G. J. Milburn, and M. Aspelmeyer, "Pulsed quantum optomechanics," *Proceedings of the National Academy of Sciences*, vol. 108, no. 39, pp. 16182–16187, 2011.

[81] A. Szorkovszky, G. A. Brawley, A. C. Doherty, and W. P. Bowen, "Strong thermomechanical squeezing via weak measurement," *Physical review letters*, vol. 110, no. 18, pp. 184301, 2013.

[82] A. Vinante and P. Falferi, "Feedback-enhanced parametric squeezing of mechanical motion," *Physical review letters*, vol. 111, no. 20, pp. 207203, 2013.

[83] A. Kronwald, F. Marquardt, and A. A. Clerk, "Arbitrarily large steady-state bosonic squeezing via dissipation," *Physical Review A*, vol. 88, no. 6, pp. 063833, 2013.

[84] J. F. Poyatos, J. I. Cirac, and P. Zoller, "Quantum reservoir engineering with laser cooled trapped ions," *Physical review letters*, vol. 77, no. 23, pp. 4728, 1996.

[85] J. I. Cirac, A. S. Parkins, R. Blatt, and P. Zoller, ""dark" squeezed states of the motion of a trapped ion," *Physical review letters*, vol. 70, no. 5, pp. 556, 1993.

[86] P. Rabl, A. Shnirman, and P. Zoller, "Generation of squeezed states of nanomechanical resonators by reservoir engineering," *Phys. Rev. B*, vol. 70, pp. 205304, Nov 2004.

[87] A. S. Parkins, E. Solano, and J. I. Cirac, "Unconditional two-mode squeezing of separated atomic ensembles," *Phys. Rev. Lett.*, vol. 96, pp. 053602, Feb 2006.

[88] E. G. Dalla Torre, J. Otterbach, E. Demler, V. Vuletic, and M. D. Lukin, "Dissipative preparation of spin squeezed atomic ensembles in a steady state," *Phys. Rev. Lett.*, vol. 110, pp. 120402, Mar 2013.

[89] J. M. Pirkkalainen, E. Damskägg, M. Brandt, F. Massel, and M. A. Sillanpää, "Squeezing of quantum noise of motion in a micromechanical resonator," *ArXiv e-prints*, 2015.

[90] F. Lecocq, J. B. Clark, R. W. Simmonds, J. Aumentado, and J. D. Teufel, "Quantum nondemolition measurement of a nonclassical state of a massive object," *ArXiv e-prints*, 2015.

[91] Phil Gregory, *Bayesian Logical Data Analysis for the Physical Sciences: A Comparative Approach with Mathematica® Support*, Cambridge University Press, 2005.

[92] J. Goodman and J. Weare, "Ensemble samplers with affine invariance," *Communications in Applied Mathematics and Computational Science*, vol. 5, no. 1, pp. 65–80, 2010.

[93] D. Foreman-Mackey, D. W. Hogg, D. Lang, and J. Goodman, "emcee: The mcmc hammer," *Publications of the Astronomical Society of the Pacific*, vol. 125, no. 925, pp. 306–312, 2013.

[94] WA Phillips, "Two-level states in glasses," *Reports on Progress in Physics*, vol. 50, no. 12, pp. 1657, 1987.

[95] Girish S Agarwal, Yifu Zhu, Daniel J Gauthier, and Thomas W Mossberg, "Spectrum of radiation from two-level atoms under intense bichromatic excitation," *JOSA B*, vol. 8, no. 5, pp. 1163–1167, 1991.

[96] Magdalena Constantin, C Yu Clare, and John M Martinis, "Saturation of two-level systems and charge noise in josephson junction qubits," *Physical Review B*, vol. 79, no. 9, pp. 094520, 2009.